Springer Theses
Recognizing Outstanding Ph.D. Research

Jie Cheng

Research on Chemical Mechanical Polishing Mechanism of Novel Diffusion Barrier Ru for Cu Interconnect

Springer

Springer Theses

Recognizing Outstanding Ph.D. Research

Aims and Scope

The series "Springer Theses" brings together a selection of the very best Ph.D. theses from around the world and across the physical sciences. Nominated and endorsed by two recognized specialists, each published volume has been selected for its scientific excellence and the high impact of its contents for the pertinent field of research. For greater accessibility to non-specialists, the published versions include an extended introduction, as well as a foreword by the student's supervisor explaining the special relevance of the work for the field. As a whole, the series will provide a valuable resource both for newcomers to the research fields described, and for other scientists seeking detailed background information on special questions. Finally, it provides an accredited documentation of the valuable contributions made by today's younger generation of scientists.

Theses are accepted into the series by invited nomination only and must fulfill all of the following criteria

- They must be written in good English.
- The topic should fall within the confines of Chemistry, Physics, Earth Sciences, Engineering and related interdisciplinary fields such as Materials, Nanoscience, Chemical Engineering, Complex Systems and Biophysics.
- The work reported in the thesis must represent a significant scientific advance.
- If the thesis includes previously published material, permission to reproduce this must be gained from the respective copyright holder.
- They must have been examined and passed during the 12 months prior to nomination.
- Each thesis should include a foreword by the supervisor outlining the significance of its content.
- The theses should have a clearly defined structure including an introduction accessible to scientists not expert in that particular field.

More information about this series at http://www.springer.com/series/8790

Jie Cheng

Research on Chemical Mechanical Polishing Mechanism of Novel Diffusion Barrier Ru for Cu Interconnect

Doctoral Thesis accepted by
Tsinghua University, Beijing, China

Springer

Author
Dr. Jie Cheng
State Key Laboratory of Tribology
Tsinghua University
Beijing
China

Supervisor
Prof. Xinchun Lu
State Key Laboratory of Tribology
Tsinghua University
Beijing
China

ISSN 2190-5053 ISSN 2190-5061 (electronic)
Springer Theses
ISBN 978-981-10-6164-6 ISBN 978-981-10-6165-3 (eBook)
DOI 10.1007/978-981-10-6165-3

Library of Congress Control Number: 2017952025

Printed on acid-free paper

This Springer imprint is published by Springer Nature
The registered company is Springer Nature Singapore Pte Ltd.
The registered company address is: 152 Beach Road, #21-01/04 Gateway East, Singapore 189721, Singapore

To my parents for their love,
concern and support
Zhijian Cheng (Dad)
Yongfeng Deng (Mom)

谨以此文献给我的父母,
感谢他们对我的关心、支持和爱。
程志坚 (爸爸)
邓永凤 (妈妈)

Supervisor's Foreword

Chemical mechanical polishing (CMP) has been recognized as the enabling technology to achieve global planarization, which is essential in the manufacturing of integrated circuit. The criteria to evaluate the polishing effects are explicit and intuitive, but efforts to achieve a good polishing result ask for the comprehensive understanding of the underlying mechanism during CMP. Interdisciplinary knowledge regarding the materialogy, tribology, corrosion and surface science is involved, making CMP an intricate process. Therefore, the fundamental investigations about the polishing mechanism are difficult and still incomplete. Also, the emerging technologies and materials during the fabrication of integrated circuit continuously bring challenges for CMP. As a result, imperious demands for the fundamental investigations of CMP have been proposed in recent years.

This thesis focuses on the fundamental research on CMP when ruthenium is used as novel diffusion barrier layer material. The findings in the thesis are of great value to in-depth understand the polishing mechanism of ruthenium and copper, and to enlighten about solutions for the unsolved problems during the barrier layer polishing process. The research work presented in the thesis is independently accomplished by Dr. Jie Cheng, who is rigorous and creative during the scientific research. Hopefully, this doctoral thesis could be inspiring to the relevant researchers and a cornerstone to the great advance of CMP technology.

Beijing, China
May 2017

Prof. Xinchun Lu

Preface

The doctoral thesis focuses on the fundamental studies of chemical mechanical polishing (CMP) of ruthenium (Ru), and the research findings displayed in the thesis were mainly carried out in the State Key Lab of Tribology (SKLT), Tsinghua University. In SKLT, there were good research foundations for CMP, both in the equipment development and the fundamental research of manufacturing process. Apart from this, the outstanding achievements on tribology theories in the laboratory, which reveal the principles of friction, lubrication and wear, provided new perspectives for the in-depth understanding of CMP process. The choice of the investigation target, the preparation of the samples and some experimental work were done in close collaboration with other partners.

As the technology node of integrated circuit develops to sub-14 nm, the application of novel barrier layer is in urgent need in order to support the fabrication of copper (Cu) interconnects. It has been proved that the most promising candidates for the diffusion barrier are metals such as molybdenum (Mo), cobalt (Co) and ruthenium (Ru). The polishing of Mo and Co is easier, but there still exist issues related to the CMP of Ru because of its high chemical-inertness and hardness. The biggest problem lies in the low polishing rate when traditional H_2O_2 is used as oxidant in the polishing slurry. Therefore, a completely new polishing system should be established when Ru is selected as the barrier layer material, in order to achieve a considerable polishing rate of Ru compared with that of Cu. In the thesis, KIO_4 has been chosen as the substitute of H_2O_2 in polishing slurry, and the material removal mechanism of Ru and Cu during the barrier layer polishing stage has been investigated.

Once Ru is chosen as the replacement of existing barrier layer, extensive investigation to control the corrosion process during CMP is quite essential. One big headache is the galvanic corrosion of Cu at Cu/Ru interface due to the large gap in the galvanic series between them, which might generate interfacial defects after polishing. Another issue is the poor surface quality of Cu when polished in KIO_4-based slurries. Therefore, ways to control the corrosion of Cu have been sought for in the thesis.

In the thesis, systematic investigations of Ru CMP have been presented. The tribocorrosion properties and the material removal mechanism of Cu and Ru in KIO_4-based slurry were firstly investigated based on the chemical mechanical synergistic mechanism. Considering the galvanic corrosion issue, the galvanic corrosion at Cu/Ru interface was then studied from a microperspective and in-situ perspective, and on the basis, ways to mitigate corrosion using different corrosion inhibitors were subsequently proposed. The investigation of microgalvanic corrosion for Cu/Ru coupling was under the collaboration with the Division of Surface and Corrosion Science, KTH Royal Institute of Technology, Sweden.

The doctoral thesis includes 8 chapters, 23 tables and 107 figures. Only the selected results from fundamental studies are shown in the thesis. More investigations are still on the way. Practical CMP results using test-patterned wafers will be reported in the subsequent publications.

Beijing, China Dr. Jie Cheng

Acknowledgements

I take this opportunity to convey sincere gratitude to my advisor, Prof. Xinchun Lu, for his continuous inputs and invaluable guidance over the course of my graduate study. I would not have made it through these years without his support. The skills I have learned in his group will continue to be a great asset for me in the future.

I want to acknowledge Prof. Jinshan Pan (at KTH Royal Institute of Technology), Dr. Tongqing Wang and Prof. Yongyong He for sharing the research experiences and ideas to help me solve scientific questions. Apart from this, they devoted time in reviewing my papers and assisting me throughout my research.

It's a pleasure to express regards to the professors and working staffs in the State Key Lab of Tribology (SKTL) of Tsinghua University for the unselfish help. My labmates, Hegeng Mei, Jing Li, Zhimin Chai, Liang Jiang, Jing Peng, Wenbin Zhou, Hongkai Li and Jie Wang, gave their support and assistance during my research. It has been a pleasure to work with all of them.

I am grateful for the support and funding provided for this research by the Science Fund for Creative Research Groups (51321092), the National Natural Science Foundation of China (51335005, 91323302) and the National Basic Research Program of China (2015CB057203).

Last but not least, I would like to thank my parents for the encouragement and unconditional love.

Contents

Abbreviations

AA	Ascorbic Acid
AES	Auger Electron Spectroscopy
AFM	Atomic Force Microscopy
AFP	Abrasive-free Polishing
ALD	Atomic Layer Deposition
BEOL	Back End of Line
BTA	Benzotriazole
CAN	Ceric Ammonium Nitrate
CE	Chemical Etching
CIE	Corrosion Inhibition Efficiency
CMP	Chemical Mechanical Polishing
COF	Coefficient of Friction
CRM	Confocal Raman Microspectroscopy
CVD	Chemical Vapour Deposition
DHA	Dehydroascorbate
DI	De-Ionized
ECD	Electrochemical Deposition
ECMP	Electrochemical Mechanical Polishing
ECP	Electrochemical Polishing
EIS	Electrochemical Impedance Spectroscopy
FEOL	Front End of Line
FIB	Focused Ion Beam
IC	Integrated Circuit
ITRS	International Technology Roadmap for Semiconductors
KFM	Kelvin Probe Force Microscopy
MOL	Middle of Line
MRR	Material Removal Rate
OCP	Open Circuit Potential
PECVD	Plasma Enhanced Chemical Vapour Deposition
PVD	Physical Vapour Deposition

Ra	Surface Average Roughness
SEM	Scanning Electron Microscopy
SER	Static Etch Rate
SHE	Standard Hydrogen Electrode
STI	Shallow Trench Isolation
TEM	Transmission Electron Microscope
XPS	X-ray Photoelectron Spectroscopy

Chapter 1
Introduction

1.1 Development of Ultra-Large Scale Integrated Circuit

1.1.1 Sub-14 Nm Technology Node

The decreasing feature size is the main driving force to improve the operation speed, to lower the power consumption, and to improve the package density throughout the development of integrated circuit (IC) industry. In 1965, Gordon Moore predicted that the number of transistors of IC will increase exponentially, and will double per 1.5–2 years. The so-called Moore's law, which is the empirical law of the IC industry, still functions well in the prediction of the number of transistors. The continuous development of semiconductor chips largely depends on the application of new materials, the advances of manufacturing process, and the shrinking feature size. The shrinking feature size is at the expense of increased complexity of multilevel interconnects. This phenomenon is applicable to Intel processors, as is shown in Fig. 1.1 (Ingerly et al. 2012; Fischer et al. 2015). The 14 nm chip has 13 layered structure, while that for 22 nm chip is only 9. When the feature size shrinks to 14 nm and below, key problems, such as the interconnect delay (RC delay), the cross-talk noise, the width-dependent surface scattering effects, and the power consumption, have become hindrance to the development of ultra-large scale integrated circuit.

RC delay presents a measure of the time delay for signal propagation. For the local interconnects, RC delay remains almost unchanged as the feature size decreases. However, the length of global interconnects often increases for each new technology generation, and therefore the RC delay of global interconnects has a large impact on device performance (Kumar 2008). Table 1.1 shows part of the important data from International Technology Roadmap for Semiconductors 2013 (ITRS 2013) (Wilson 2013). It could be seen that the RC delay is becoming increasingly serious, from 2105 ps at 14 nm technology node to 4005 ps at 10 nm

J. Cheng, *Research on Chemical Mechanical Polishing Mechanism of Novel Diffusion Barrier Ru for Cu Interconnect*, Springer Theses,
DOI 10.1007/978-981-10-6165-3_1

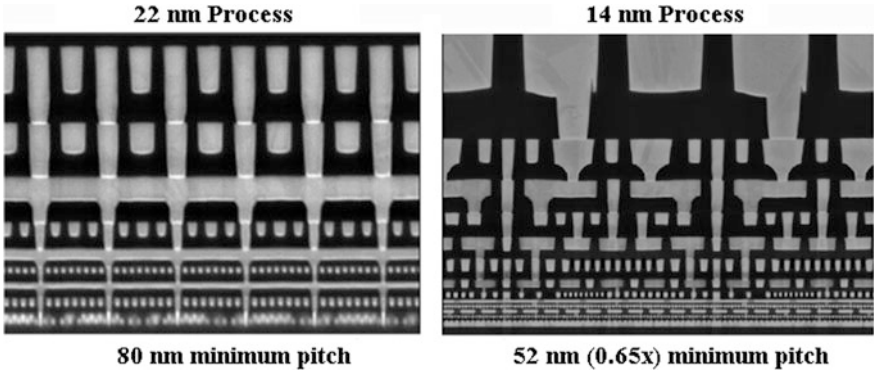

Fig. 1.1 Scanning electron microscopy (SEM) images of the Intel 22 and 14 nm chips

Table 1.1 MPU interconnect technology requirements (data from ITRS 2013)

Year of production	2013	2015	2017	2019	2021	2023	2025
MPU physical gate length (nm)	20.17	16.80	14.00	11.67	9.72	8.10	6.80
DRAM 1/2 pitch (nm)	31.82	25.26	20.05	15.91	12.63	12.02	7.09
Metal 1 wiring pitch (nm)	54	42	34	27	21	17	13
Metal 1 A/R (for Cu)	1.9	1.9	2.0	2.0	2.1	2.1	2.2
Barrier/cladding thickness for Cu (for Cu Metal 1 wiring) (nm)	2.4	1.9	1.5	1.2	1.0	0.8	0.6
Intermediate wiring pitch (nm)	54	42	34	27	21	17	13
Intermediate wiring dual damascene A/R (Cu wire)	1.9	1.9	2.0	2.0	2.1	2.1	2.2
Min. global wiring pitch range (nm)	81	63	51	40	32	25	20
Global wiring dual damascene A/R (Cu wire)	2.34	2.34	2.34	2.34	2.34	2.34	2.40
Interconnect RC delay (ps) for 1 mm Cu min pitch global wire	2105	4005	6660	12,155	21,542	35,357	63,818

technology node. Therefore, it is necessary to search for solutions to reduce the RC delay at the physical design, interconnects, and material levels.

1.1.2 The Application of New Materials for Interconnects

In this section, the solutions at material level are mainly introduced. Equation 1.1 shows the RC delay in a multilevel interconnect structure (Kumar 2008). K and χ represent the dielectric constant and oxide thickness, respectively. ε is the permittivity of free space and ρ is the interconnect resistivity. L, W and H are the

interconnect length, width and height, respectively. L_s is the distance between two adjacent lines. It is obvious that a smaller K and ρ could reduce the RC delay on the condition that the interconnect structure and the physical design remain unchanged.

$$RC \propto K\varepsilon\rho\frac{L^2}{WH}\left(\frac{W}{\chi}+\frac{H}{L_s}\right) \tag{1.1}$$

As aforementioned, one effective way to reduce the RC delay is to lower the dielectric constant K. The substitute for traditional SiO_2 dielectric ($K \sim 4.0$) is low-K dielectric materials. The low-K dielectric materials could be divided into three kinds: air gap, low-K organic polymer and porous carbon doped material (Gottfried et al. 2006). Presently the most commonly used is the porous carbon doped low-K material made by plasma enhanced chemical vapor deposition (PECVD-SiOCH), the K value of which is 2.5–3.2 (Wong et al. 2004). However, the application of low-K dielectric material is extremely difficult, as is shown in Fig. 1.2. It was proposed in 2007 that the K value will decrease to 2.1–2.5 in 2015, while the application will be postponed after 2021 according to ITRS 2011. The promising application of low-K dielectric material requires not only the low K value, but also high thermal stability, gap filling ability, adhesion property, and compatibility with chemical mechanical polishing (CMP) process (Iwai 2009; Wang et al. 2001). The high requirements account for the delay of the low-K material application.

To be specific, the etching, CMP, and physical vapor deposition (PVD) process could also significantly affect the properties of low-K material. For instance, when the K value is below 2.0, the mechanical strength of low-K material is only 1/30 of SiO_2. During the following CMP process, surface damage and interfacial delamination could happen, and therefore it is difficult to obtain a defectless wafer surface (Fig. 1.3) after polishing (Iacopi et al. 2004; Mosig et al. 2002). Apart from this, the plasma etching process might change the surface properties of low-K material, thus

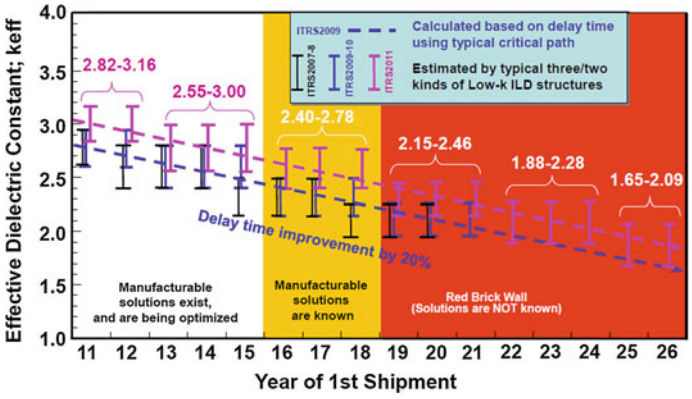

Fig. 1.2 The technology roadmap for low-K dielectric material

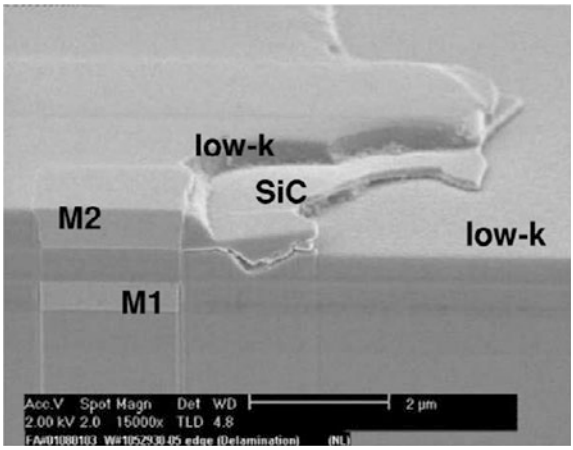

Fig. 1.3 Delamination occurring during dual damascene CMP

resulting in an increase of the *K* value (Wang et al. 2005). Also, the dielectric properties could be affected when metal ions diffuse into low-*K* materials using PVD as the preparation method (Posseme et al. 2008). Normally, a thin capping layer is deposited onto the low-*K* dielectric material surface to avoid direct contact during CMP. The plasma pretreatment of the ultralow-*K* material surface could be applied to further improve its compatibility (Behera et al. 2011). By this method, the intrinsic properties remain unchanged, and the surface pores are sealed. In this way, the low-*K* dielectric material is protected from the damages of other manufacturing processes.

Another way to decrease the RC delay is to lower the resistance of interconnects. Nowadays, Cu has taken place of Al as the interconnect material. The resistivity of Cu is 1.7 μΩ cm, while that for Al is 2.8 μΩ cm. Therefore, the application of Cu has significantly reduced the RC delay. Another reason for the application of Cu lies in its strong anti-electromigration ability. Electromigration could cause voids in metal interconnects and vias, thus generating circuit failure and other reliability issues. The upper limit of current density for Cu and Al is 5×10^6 A/cm^2 and 2×10^5 A/cm^2 respectively when electromigration occurs. As a consequence, the lifetime of Cu is 110 times of Al under extreme conditions (high current density and high temperature). When Cu is used as the interconnect material, ca. 30% energy could be saved, the number of interconnect layers could be reduced, and thus the manufacturing process is simplified (Baklanov et al. 2007).

However when the critical dimension continuously shrinks, the aspect (A/R) ratio is increasingly larger. The Cu made by traditional electrochemical deposition (ECD) method is facing great challenges. It is difficult to deposit Cu in such a shallow trench and the Cu made by ECD often has large grains like bamboo, which is the hotbed for electromigration. To further improve the anti-electromigration property of Cu, Cu alloys, such as CuAl and CuTi, are proposed as potential solutions (Tada et al. 2006; Cao et al. 2014). For example, the anti-electromigration ability is improved 50 times when CuAl alloy and optimized Cu/capping structure

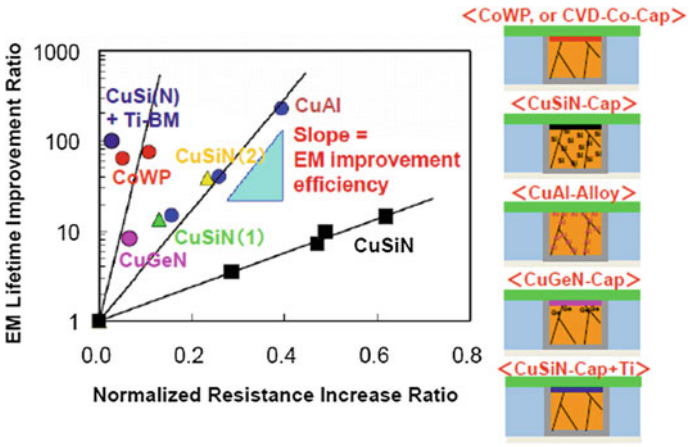

Fig. 1.4 Anti-electromigration properties of different Cu alloys

are used, as is shown in Fig. 1.4. The only disadvantage is that the resistivity of the wiring could more or less increase.

1.2 Ru as Novel Diffusion Barrier

1.2.1 Novel Barrier Materials

Traditional Ta/TaN barrier cannot meet the strict demands from the fast development of interconnect technology due to its high resistivity (13 μΩ cm). To further lower the interconnect resistivity, new barrier layer materials should be used. Dual damascene technique is applied to the back end of line (BEOL) process, and the detailed procedures are shown in Fig. 1.5. It should be noted that the high A/R ratio (∼2.4) and narrow trenches of sub-14 nm technology node have proposed great challenges for the manufacturing process of Cu interconnects, especially for the thin film preparation and the filling of trenches:

- It is difficult to deposit uniform Cu seed layer by PVD method (Roule et al. 2007);
- Voids and overhangs could happen during Cu deposition in narrow trenches (Venkataraman 2012);
- Barrier with lower resistivity is needed;
- Methods to prepare ultra-thin barrier layer are in urgent need.

Presently seedless ECD Cu is the hot area of research, as is shown in Fig. 1.6 (Josell et al. 2003, 2006). Suitable barrier layer material should support the direct

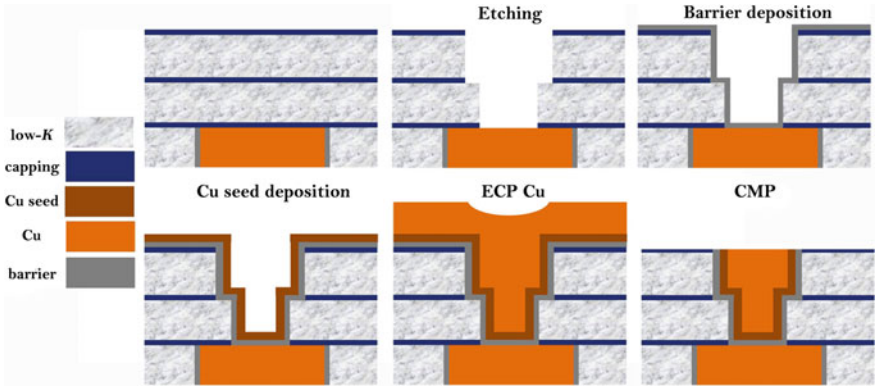

Fig. 1.5 Dual damascene process

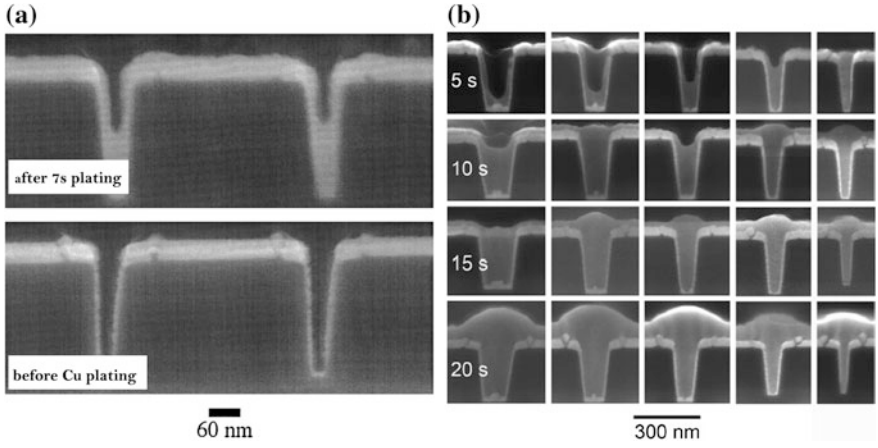

Fig. 1.6 Seedless Cu plating in trenches: **a** Ru/Ta as barrier layer; **b** Os as barrier layer

plating of Cu, without predepositing a Cu seed layer (normally ≥ 10 nm). In this way, the poor coverage of step will be improved (Urzo et al. 2012; Chen et al. 2009).

To achieve the seedless direct Cu plating on barrier, traditional Ta/TaN barrier is inadequate and should be replaced by novel barrier layer. The potential barrier layer materials should have low electrical resistance and immiscibility with Cu, good adhesion property to the substrate, and easy preparation method (Goldberg and Kuo 2003). Nowadays the mostly investigated novel barrier materials are the transition metals, together with their carbide, nitride, alloy and oxide (Alén et al. 2006).

The first group is the transition metals. Metals such as ruthenium (Ru), cobalt (Co), molybdenum (Mo) and zirconium (Zr) are investigated recently (Arunagiri

Table 1.2 Properties of Co, Mo and Ru as barrier layer materials

Transition metals	Ru	Co	Mo
Thickness (nm)	5	30	60
Breakdown T (°C)	300	500	500
Lasting time (min)	10	60	60

et al. 2005a, b; Li et al. 2005; He and Feng 2004; Chen et al. 2004). Table 1.2 shows the properties of some transition metals as barrier layer materials (Ono et al. 1994; Kohn et al. 2001; Arunagiri et al. 2005a, b). However, nucleation of metals will occur at comparatively low temperatures, which will provide paths for the diffusion of Cu (Chan et al. 2004). Consequently, their diffusion property should be further improved.

The second group is the compounds of transition metals. The application of those compounds will largely reduce the thickness of barrier layer and improve the reliability of interconnects (He et al. 2012; Wojcik et al. 2011). By doping to the transition metals, the thermal stability and amorphous compactness are improved, which will contribute to the diffusion barrier properties. A 5 nm Ru–C film can retard the diffusion of Cu after a prolonged (30 min) annealing up to 700 °C, while the Ru film is effective up to only 400 °C, as is shown in Fig. 1.7 (Chen et al. 2009). Similarly, a sputtered 50 nm Mo-N film could also improve the annealing temperature from 500 to 600 °C (Chuang et al. 1999).

The third group is the self-formed barrier. Cu-X (X stands for metals) alloys are used as the interconnect metals, which are directly deposited onto the dielectric material. After heat-treating process, the X metal will precipitate out to the alloy/dielectric interface and react with the oxygen, forming a super-thin diffusion barrier. At present, CuMn and CuAl alloys could form the most effective self-formed barrier (Usui et al. 2006). However, disadvantages such as poor adhesion to the substrate and low compatibility with CMP will limit its application (Kohama et al. 2010).

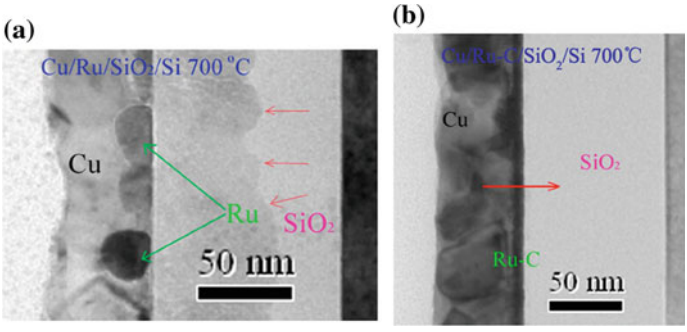

Fig. 1.7 Annealing at 700 °C for 30 min: **a** with Ru as barrier layer; **b** with Ru-C as barrier layer

1.2.2 Properties of Ru

As aforementioned, the key to select the barrier layer material is the ability to support seedless direct plating of Cu. Figure 1.8 shows the Eh-pH diagram (Pourbaix diagram) of Cu. During the electroplating of Cu, Cu^{2+} in electrolyte is reduced to Cu. The plating potential should not be too low to avoid hydrogen brittleness. Therefore, the Cu electroplating could proceed within a wide range of potential and pH values, as is indicated in the red circle in Fig. 1.8.

Cu should have good nucleation and adhesion properties on barrier layer materials to achieve the "direct-on-barrier" process (Kim et al. 2005). Such kind of barrier layers should meet the following requirements: surface oxide could be removed/dissolved within the Cu electroplating potential; the barrier material will not react with Cu. Table 1.3 summarizes the properties of some transition metals (Gibson and Sudworth 1973; Bard et al. 1985). It is obvious that platinum group metals such as Pd, Pt and Ru could be reduced to metallic state at all pH values. However, Pd and Pt have low melting point and polycrystalline structure, which will deteriorate the diffusion properties at high temperature (Massalski et al. 1990; Zhu et al. 2006). Apart from this, it is not easy to get the precursors for the atomic

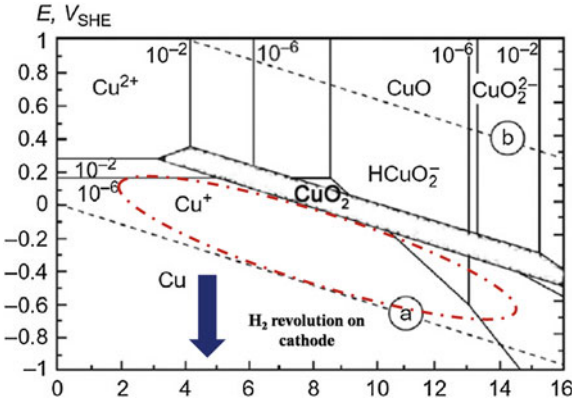

Fig. 1.8 Eh-pH diagram of Cu-H_2O system

Table 1.3 Basic properties of some barrier layer materials

Transition metal	Ru	Co	Mo	Ta	Ti	Pd
Bulk resistivity (μΩ cm)	7.1	6.0	5.2	13	40	10
Density (kg/m^3) 273 K	12,370	8900	10,280	16,650	4507	12,023
Melting point (°C)	2250	1495	2617	2996	1660	1552
Displacement reaction potential	−0.115	0.617	0.473	0.74	1.147	−0.575
pH range to remove the surface oxide	All pH values	*	−2 to 2 6 to 14	No pH values	−2 to 0	All pH values

layer deposition (ALD) method when preparing the ultra-thin film. All of those shortcomings mentioned above impose restrictions on the application of Pt and Pd as the diffusion barrier layer materials.

Ru, as a novel barrier layer material, shows good direct Cu electroplating property, and gains lots of attention during the past few years. The advantages of Ru as barrier layer are: (1) low resistivity (7.1 μΩ cm); (2) high melting point (2250 °C); (3) good adhesion and wetting properties; (4) immiscibility with Cu. Ru is inert to most of the chemicals and its oxidation at room temperature is extremely slow. Aqua regia, H_2SO_4, HCl and H_3PO_4 could not corrode Ru even at 100 °C. However, Ru could react with strong oxidants such as H_2O_2, ammonium persulfate and periodates (Cui et al. 2013; Kim et al. 2008). The common valances of Ru are 0, +3, +4, +7 and +8. The common Ru oxides are: solid state hydrous RuO_2 (black), RuO_3 and $Ru(OH)_3$; unstable soluble RuO_4; soluble RuO_4^- (green) and H_2RuO_5 (golden yellow). Among them, RuO_2 is very stable. When Ru reacts with strong oxidant, the product is often hydrous RuO_2 (Cheng et al. 2015). It should be noted that RuO_4 is toxic and volatile, which should be avoided in industrial productions (Zimmerman et al. 1990). Figure 1.9 shows the Eh-pH diagram of Ru, from which it is obvious that the equilibrium potential of electrode reactions, pH value of

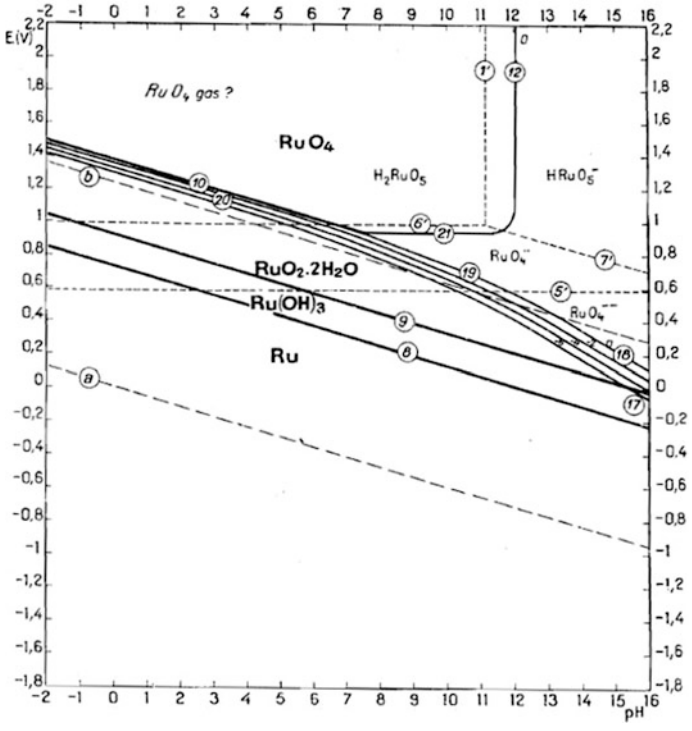

Fig. 1.9 Eh-pH diagram of Ru-H_2O system (25 °C)

solution, ionic activity, temperature and pressure will affect the stability of different valence states of Ru. Considering different pH values, the possible reactions of Ru as reductant are listed as follows (Connick and Hurley 1952; Seddon and Seddon 2013; Griffith 2010). In acidic solutions, Ru could be oxidized to RuO_2 and RuO_4. RuO_4 is quite soluble in water, forming H_2RuO_5. H_2RuO_5 could further decomposes to $RuO_2 \cdot 2H_2O$ in the presence of reductant. The reactions are shown in Eqs. 1.2 to 1.4.

$$Ru + 4H_2O = RuO_2 \cdot 2H_2O + 4H^+ + 4e^- \tag{1.2}$$

$$RuO_4 + H_2O = H_2RuO_5 \tag{1.3}$$

$$H_2RuO_5 + 4H^+ + 4e^- = RuO_2 \cdot 2H_2O + H_2O \tag{1.4}$$

In alkaline solutions, the following three reactions might happen apart from Eq. 1.2. Under this condition, Ru will be dissolved to form RuO_4^-.

$$RuO_2 + 2H_2O = RuO_4^{2-} + 4H^+ + 2e^- \tag{1.5}$$

$$RuO_2 + 2H_2O = RuO_4^- + 4H^+ + 3e^- \tag{1.6}$$

$$3RuO_4^{2-} + 4H_2O = 2RuO_4^- + RuO_2 \cdot 2H_2O + 4OH^- \tag{1.7}$$

It should be noted that the electrochemical and chemical reaction species are decided by the pH value, the electrode reaction equilibrium potential, and the ionic activity. With regard to a specific system, the actual Eh-pH diagram should be used instead of the empirical Ru-H_2O diagram. Besides, the Eh-pH diagram could only provide thermodynamic data. The actual reaction process is also affected by the kinetics of reaction.

1.2.3 Preparation of Ru as Barrier Film

The properties of barrier layer depend on not only the intrinsic properties of the material, but also the preparation method. Basically there are three kinds of preparation methods, that is, PVD, CVD and ALD. For the thin film preparation, PVD is the most widely used method. However, films made by PVD often have critical defects such as poor step coverage as the dimensions of trenches continuously shrink. On the contrary, the biggest advantage of CVD lies in the superb step coverage, that is, to keep the conformity of the film even in the trenches of high A/R (10:1) ratio. At the same time, high deposition efficiency and comparatively low requirement of vacuum are also highlights of CVD. The shortcoming of CVD method is the comparatively high reaction temperature, mostly above 600 °C, which brings about great challenges for the thermal stability of the interconnect

structure. ALD is a special modification of CVD technology by which precursors are pulsed onto the surface of the substrate, with the purge cycle of inert gas between the precursor cycles. The self-limiting feature of ALD enables the growth of highly uniform and conformal films, with the thickness controlled at the atom level (Chai et al. 2012). Therefore, ALD is quite suitable for the preparation of ultra-thin films (<5 nm). Apart from this, pure films can be deposited at relatively lower temperatures (Leskelä and Ritala 2003). Therefore, ALD will be the most promising method to be applied in the ultra-thin barrier layer deposition for the sub-14 nm interconnect structure.

Figure 1.10 shows the 20 nm Ru film deposited on Si substrate by magnetron sputtering (Chan et al. 2004). It is found that Ru has the columnar microstructure oriented vertically with respect to Si substrate, which could effectively hinder the diffusion between Cu and Si. The seedless electroplated Cu film on Ru is shiny, smooth, and without agglomeration observed by SEM. The investigation results reveal a well-defined interface and show that Cu interdiffusion could be impeded by Ru thin film up to 450 °C vacuum annealing.

Figure 1.11 shows a 5 nm Ru on Si substrate by the same preparation method mentioned above (Arunagiri et al. 2005a, b). The direct Cu plating on it yields a homogeneous Cu film with over 90% plating efficiency. It is demonstrated that the ultra-thin Ru film can function as a directly plateable Cu diffusion barrier up to at least 300 °C vacuum anneal. Transmission electron microscope (TEM) reveals an interlayer between Ru/Si, the composition of which is Ru_xSi_y. This silicidation is mainly attributed to the failure of the ultrathin Ru barrier at the higher annealing temperature.

As mentioned in Sect. 1.2.1, doping is an effective method to improve the diffusion barrier properties. For the industrial application, another easy way is to build the Ru/TaN bilayer structure in order to make full use of the "direct-on-barrier" property of Ru and the good diffusion barrier property of TaN. It is found that a Si/TaN (10 nm)/Ru (10 nm) structure could sustain an annealing

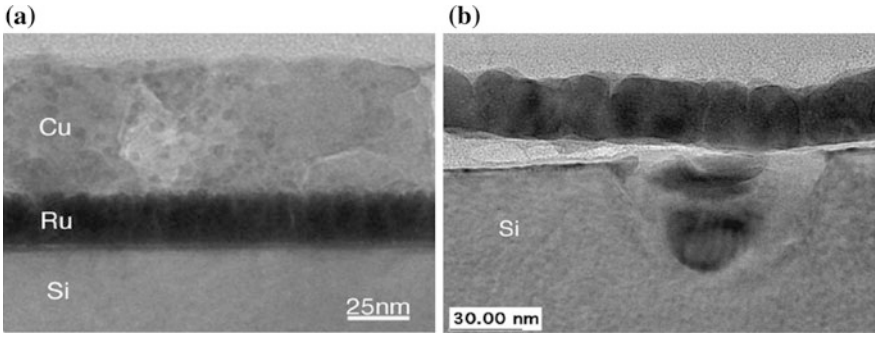

Fig. 1.10 Cross-sectional TEM image of **a** as-deposited Cu/Ru thin film on Si(100) showing Ru thin film's columnar microstructure; **b** the Cu/Ru/Si sample vacuum annealed at 550 °C, showing thin film delamination as well as diffusion into the Si substrate

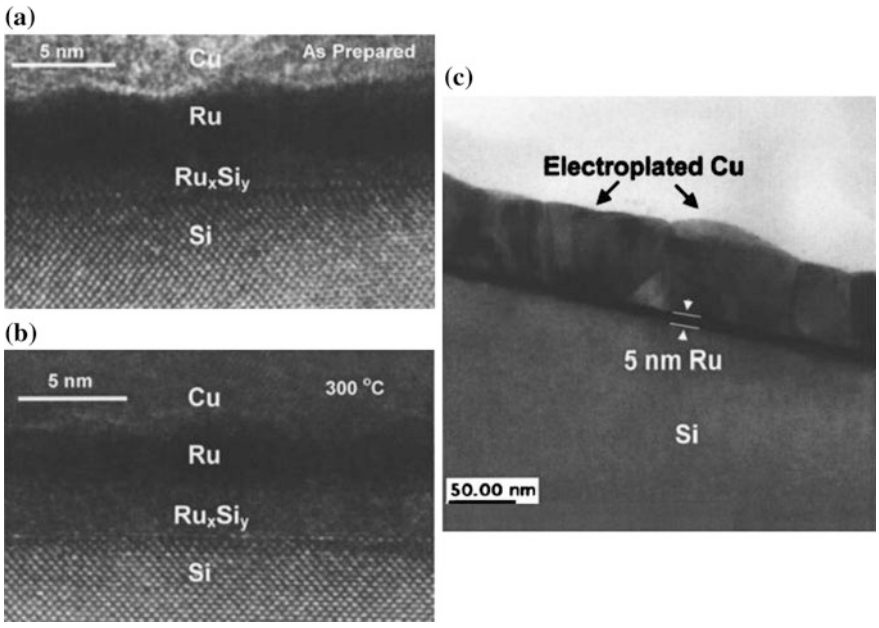

Fig. 1.11 TEM images of Si/Ru/Cu multilayer structure **a** before annealing; **b** after annealing at 300 °C; **c** the complete structure

temperature up to 900 °C (Tan et al. 2006). The only drawback is, the bilayer structure will definitely increase the thickness of the barrier layer and the resistivity of wiring.

1.3 Chemical Mechanical Polishing (CMP)

1.3.1 Introduction of CMP Technology

CMP is the key enabler for both the global and local planarization of the wafer surface. Throughout the whole production of integrated circuit, CMP plays a critical role, such as the shallow trench isolation (STI) CMP of the front end of line (FEOL), the W plug and interlayer dielectric material CMP of middle of line (MOL), and the Cu/barrier CMP of BEOL (Praveen et al. 2014; Balan et al. 2013; Oliver 2013). The material removal of CMP relies on the chemical, mechanical and the synergistic effects between them. The whole polishing process is to achieve a desirable material removal rate, surface quality and uniformity (Krishnan et al. 2009). The schematic diagram of a typical CMP tool is shown in Fig. 1.12. The working principle could be summarized as follows: Wafer is stuck to the polishing head and is in direct contact with the polishing pad under a certain down pressure;

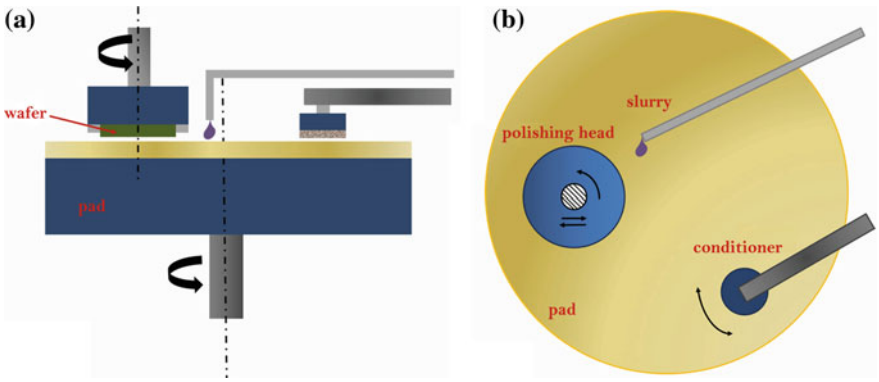

Fig. 1.12 Schematic plots of the CMP equipment: **a** front view; **b** top view

during polishing, both the polishing head and the pad rotate to the same direction, and the slurry is sprayed uniformly onto the polishing pad; the chemicals in the slurry will react with the wafer surface materials, forming more soluble products or mechanically weak nanoscale films. At the same time, the surface film is mechanically removed by the cooperation of the abrasive particles in the slurry and the asperities of the polishing pad, and finally the planarization of wafer surface is achieved.

During the CMP process, protrusions on wafer surface are in sufficient contact with the pad, thus bearing larger pressure, which have a higher MRR than that of the dishing area. The protrusions are apt to be removed by mechanical abrasion, while the dishing area is protected by the inhibitors in the slurry. In this way, a planarized surface is obtained during CMP. For the fabrication of integrated circuit, the requirements are more than that. Within wafer non-uniformity, defect rate and surface roughness are also important indicators to evaluate the CMP effects (Tano et al. 2014; Chenwei et al. 2013).

It is widely believed that the CMP process is the coupling action of the mechanical abrasion and chemical corrosion. The wafer surface undergoes "passivation-abrasion-repassivation" cyclic process, which is microscopic, dynamic and random. When the chemical and mechanical effects reach the equilibrium, the optimized CMP effects will be reached. The CMP technology involves knowledge of tribology, electrochemistry, chemistry, elastic-plastic mechanics, contact mechanics and so on. Considering the complexity of the polishing process, the material removal mechanism in it needs to be fully investigated. Undoubtedly there remains a lot of work to do because the polishing mechanism varies for different materials. The application of new technology and materials of the sub-14 nm node will as always propose challenges for the CMP technology. The fundamental investigations of the CMP process will be directive to the industrial production.

1.3.2 CMP of BEOL

The ultimate goal of CMP in Cu wiring is to remove the Cu overburden and barrier layer, thus completely isolating the Cu lines. The CMP process of Cu in BEOL could be empirically divided into three steps, as is schematically shown in Fig. 1.13.

- P1 step is the quick removal of Cu. In this stage, Cu is fast removed with a high material removal rate (>600 nm/min).The control of surface quality and defects are not the points. Therefore, normally high down pressure and hard polishing pad are applied in this stage to achieve a high polishing efficiency. A ca. 200 nm Cu film is left on the top at the end of the stage.
- P2 step is the clearing of the Cu residual. The polishing step is stopped onto the barrier layer after P2. Usually a low down pressure is applied and the MRR is lower than that of P1, about 200–300 nm/min. Investigations found that the way of combining high down pressure and low down pressure will achieve a better polishing effect (Rao et al. 2016). To make sure that no Cu residual is left, a short overpolishing process is needed. Adequate control of the overpolishing time is contributive to a good polished surface (Jiang et al. 2014a, b, c).
- P3 step is the polishing of barrier layer. The barrier layer is firstly removed and then the dielectric material. Capping layer and a small amount of dielectric material (30–40 nm according to different requirements) are removed and the process is stopped into dielectric material. This stage is characterized by the simultaneous removal of heterogeneous materials. P3 is the last polishing step and therefore the control of surface quality is quite important. Normally soft polishing pad and low down pressure are used. After this process, Cu wiring is completely isolated and the wafer is sent for post-CMP cleaning.

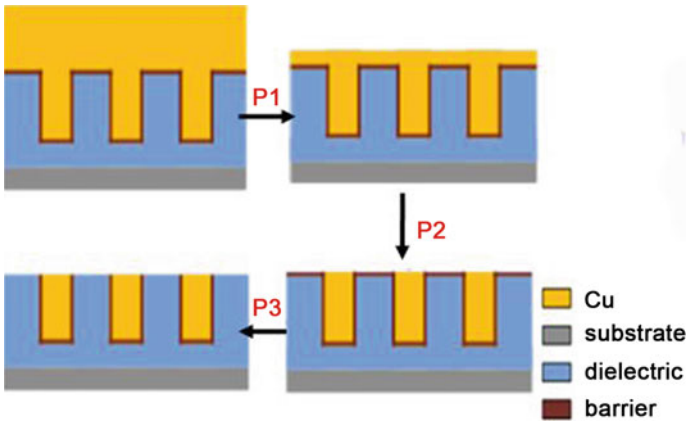

Fig. 1.13 Three polishing steps of Cu interconnects

As stated in Sect. 1.3.1, both the chemicals in slurries and mechanical parameters are decisive to the CMP effects. The mechanical parameters mainly include the polishing speed, down pressure, flow rate of slurry, polishing pad, and temperature (Tseng and Wang 1997; Li et al. 2004; Oliver et al. 2001; Kim et al. 2006). The chemical effects refer to the chemical and electrochemical reactions, the interfacial physicochemical properties between the slurry and the wafer surface (Steigerwald et al. 2008). The chemicals in the slurry are quite influential to the final polishing effects, and therefore they are the research focus in the thesis.

1.3.3 Challenges for CMP in Sub-14 Nm Technology Node

The low mechanical strength of low-*K* dielectric material has brought about issues for CMP such as delamination, material deformation and cracks, as is shown in Fig. 1.14. When the elastic modulus (*E*) of low-*K* dielectric material is over 4 GPa and the hardness (*H*) is over 0.5 GPa, traditional CMP method is feasible. However, *E* is often below 5 GPa as the *K* value (<2.2) continuously decreases for the advanced technology node (He et al. 2005; Zheng et al. 2000; Antonelli et al. 2012). The CMP process becomes quite challenging. The mechanical forces generated during polishing might damage the fragile surface of dielectric material and thus cause delamination. The vapor and chemicals in the polishing slurry might cause degradation of the dielectric property. As a consequence, weak mechanical force during polishing should be used. Meanwhile, suitable polishing and cleaning solutions should be chosen for the CMP process of sub-14 nm technology node (Ishikawa et al. 2006).

For the CMP of BEOL, the shrinking wiring width and fragile dielectric material ask for lower mechanical force during polishing. By combining the advantages of CMP, electrochemical mechanical polishing (ECMP), electrochemical polishing

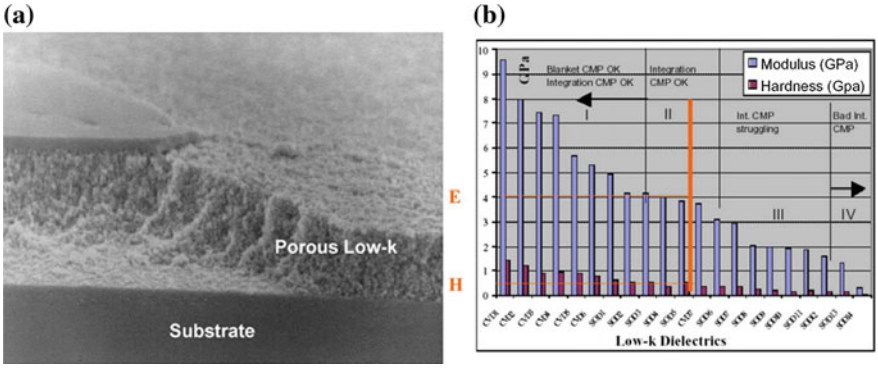

Fig. 1.14 **a** Delamination of low-*K* material after CMP; **b** issues caused by the application of low-*K* dielectric material

(ECP) and chemical etching (CE), a low-pressure CMP solution could be sought for. Under this condition, the mechanical effect is reduced, and the chemical effect is correspondingly enhanced. Therefore, the control of surface/interface corrosion will become the research focus of CMP.

Apart from the ultra-low down pressure, strict control of defects, within wafer non-uniformity and edge exclusion are also needed for the CMP tools. In addition, an effective polishing end point detection method is in urgent need because the barrier polishing (P3) is now using the in situ measuring technique, but the real end point detection is not applied yet.

Polishing consumables such as pad and slurry undergo great changes as well. The material removal during CMP is a three-body (abrasive, pad and wafer) abrasion process. In this process, the elastic deformation of polishing pad will generate problems such as overpolishing, dishing, erosion and difficulties of post-CMP cleaning. The development trend of slurry is to lower the abrasive content and enhance the chemical effect. In order to further reduce the mechanical force, abrasive-free polishing (AFP) is proposed. AFP uses slurry without abrasive particles, and the material removal largely relies on the chemical effects. By this method, the micro-scratches are reduced, but the surface quality after polishing is often far from satisfaction (Balakumar et al. 2005; Wei et al. 2009). Another more promising technique is the fixed abrasive polishing. The polishing slurry contains no abrasive particles. Sub-micro particles such as Al_2O_3, SiO_2 and CeO_2 are conglomerated by resin bond, forming small particles with specific shape. The small particles are then bonded to the polymer substrate in a certain order, and the composite-structured polishing pad is made, as is shown in Fig. 1.15c. There are enough spaces between abrasive chunks for the flow of polishing slurry, and the polishing process could be recognized as a two-body abrasion process, the material

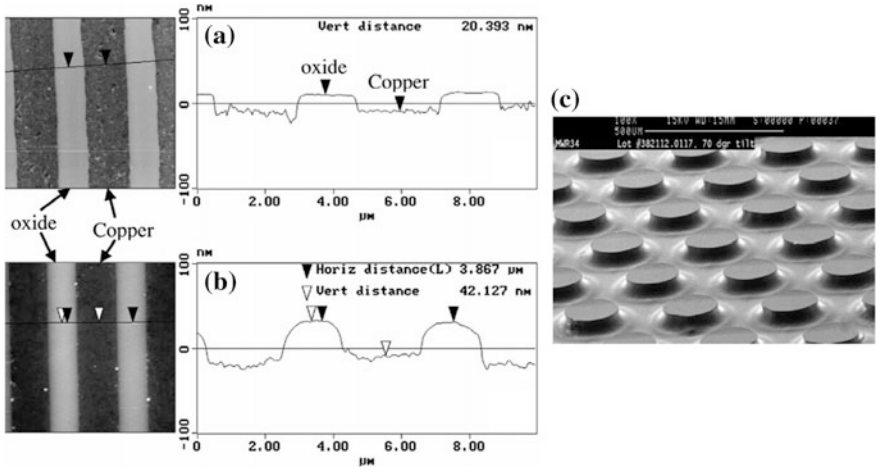

Fig. 1.15 Comparison of polishing effects with: **a** fixed-abrasive CMP; **b** traditional CMP. **c** The fixed-abrasive pad

removal selectivity of which is comparatively high. Apart from the advantages mentioned above, the fixed abrasive polishing has benefits as follows: strong rigidity of polishing pad, low within wafer non-uniformity, easy post-CMP cleaning and decreased dishing of Cu, as is shown in Fig. 1.15 (Nguyen et al. 2001; Van der Velden 2000).

1.4 CMP of Ru

1.4.1 Requirements of Ru CMP

The technical requirements of barrier layer polishing are different from those of Cu polishing:

- Ultra-low down force (≤ 1 psi) required to protect the low-*K* dielectric materials (Liu et al. 2011);
- Strict control of surface defects and within wafer non-uniformity;
- Material removal selectivity between different materials. To be specific, the same polishing rate of Cu, barrier and capping layer is required. Considering the dishing effect resulted from P1 and P2, the polishing rate of Cu should be slightly lower than that of barrier and capping layer. The material removal rate of low-*K* dielectric material should be as low as possible to avoid overpolishing and erosion.

There are all kinds of barrier layer materials, and the slurries used for barrier polishing should be adjusted according to the specific barrier layer material used. Quite different from Cu polishing, the barrier polishing process involves simultaneous polishing of different materials, and the material removal mechanism is not clear yet. The CMP technique for novel barrier layer materials is still under exploration. The methods to carry out relevant investigation are: firstly, the material removal mechanism of separated materials should be revealed; secondly, the best CMP condition should be chosen according to the relevant CMP study of separated materials; last but the most important, the patterned wafer should be used to conduct the CMP experiments in order to verify the polishing mechanism proposed above.

1.4.2 Advances of Ru CMP

Chosen of oxidants According to literature, the oxidants used in the polishing slurry of Ru mainly involve ceric ammonium nitrate (CAN), periodates, hydrogen peroxide (H_2O_2), bromates, potassium peroxymonosulfate (oxone) and persulfates (Lee and Park 2004; Kim et al. 2009; Jiang et al. 2014a, b, c; Victoria et al. 2010, 2011).

Oxone has strong oxidation ability because of the O-O bond. When the pH value is <3, oxone will decompose into potassium hydrogen sulfate. The pH of slurry is unstable and the oxidation ability will decrease. Therefore, oxone should be used in acidic slurries. However, toxic RuO_4 will be produced when the slurry is acidic, and thus alkaline slurries should be used for the CMP of Ru. Potassium bromate is similar to oxone. When potassium bromate is used as the oxidant, desirable MRR could be obtained only when the slurry pH is <2. Similarly, CAN could function well only when the slurry pH is <1. When pH is>1, CAN is in gel-like form and lose the oxidation ability (Lee et al. 2004).

Considering the stability, preparation method and the acidity of slurry, the ideal oxidants used for Ru polishing are H_2O_2 and periodates. Undoubtedly, H_2O_2 has many advantages as oxidant in polishing slurry: no extra ions are introduced in the polishing system; the potential differences between Cu and Ru in H_2O_2-based slurry is minimized (Shima et al. 2007). However, the biggest problem is the low MRR of Ru when using H_2O_2 as the oxidant. It is found that the MRR of Ru is only ca. 24 nm/min when the slurry contains 3% H_2O_2 and 2% SiO_2 abrasive at pH 10 (Jiang et al. 2014a, b, c). After the addition of 220 mM KNO_3, the MRR of Ru is elevated to 37 nm/min.

Nowadays periodates as oxidant are the research focus. When the slurry contains 0.1 M $NaIO_4$ and 2% Al_2O_3 at pH 9, the Ru lines on patterned wafer were successfully planarized and isolated, as is shown in Fig. 1.16 (Kim et al. 2008). Nevertheless, Na^+ is not desirable in the manufacturing process because it will cause electromigration, thus degenerating the electrical properties of integrated circuit (Widmann et al. 2013). Consequently, potassium periodate (KIO_4) is used as a substitute for $NaIO_4$, which is widely used in the CMP of Ru.

One disadvantage is that the solubility of KIO_4 is quite low, only 0.018 M at room temperature (20 °C). By adding KOH into the solution, the solubility of KIO_4 could be improved (Hill 1928). This unusual increase in solubility is attributed to the formation of a soluble dimesoperiodate complex (Peethala and Babu 2011). When the solution pH is 9, the solubility of KIO_4 is up to 0.36 M. Desirable

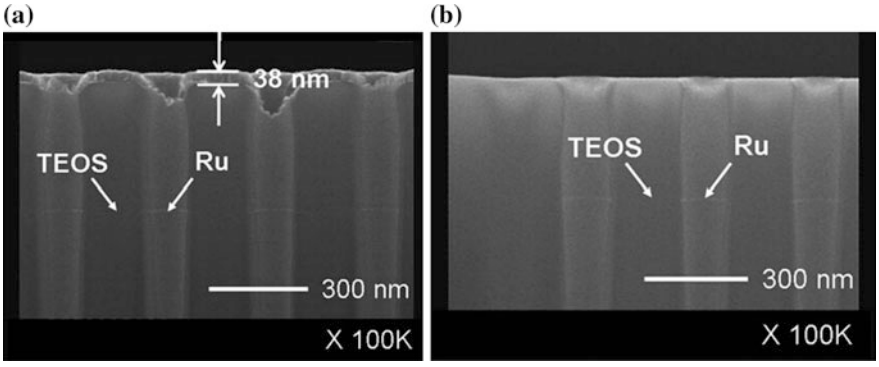

Fig. 1.16 Cross-sectional view of patterned Ru wafer: **a** before CMP; **b** after CMP

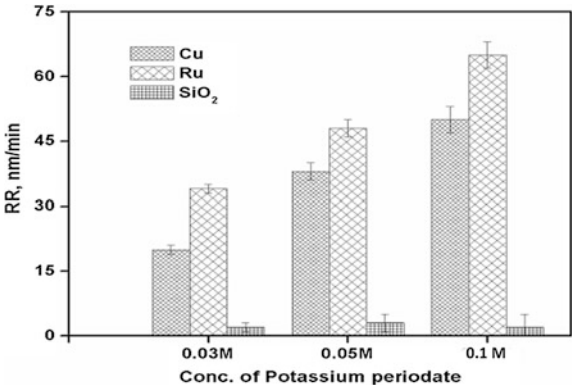

Fig. 1.17 Material removal selectivity between Ru, Cu and TEOS

polishing effects of Ru could be obtained when using KIO_4-based slurries. The material removal selectivity between Ru and Cu is 1.3:1, and that between Ru and TEOS is 30:1, as is shown in Fig. 1.17 (Brown 2012).

Other slurry additives The high hardness and chemical inertness of Ru result in a comparatively good surface quality after polishing. The other chemicals apart from oxidant will not easily react with Ru, but could change the physicochemical properties of the slurry/wafer interface by adsorption. Therefore, the functions of other additives in polishing slurry are: to adjust the material removal selectivity between different materials; to get a better surface quality (especially for Cu) after CMP; to reduce defects such as interfacial galvanic corrosion.

The pH value of the slurry has a significant effect on the polishing mechanism. The MRR of Ru as a function of slurry pH follows an arch trend, as is shown in Fig. 1.18 (Kim et al. 2009). In near neutral slurries, the MRR of Ru gets the maximum, and this is attributed to mechanically weak film formed on the surface under this condition. Other investigations include the effect of glycine on the material removal selectivity between Ru and Cu. It is found that Ru and Cu could get the same polishing rate in a slurry containing 0.05 M KIO_4, 5% SiO_2 and 2.23 mM glycine (Zeng et al. 2012). Glycine will suppress the corrosion of Ru but

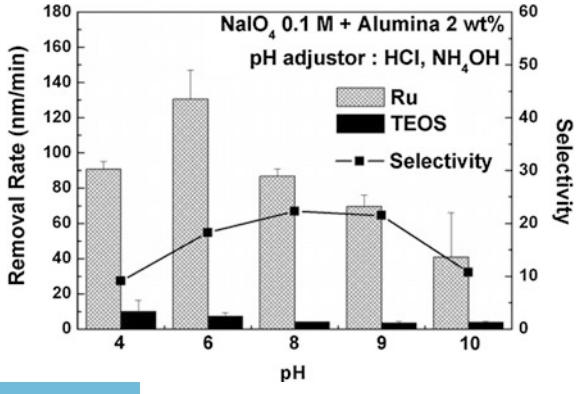

Fig. 1.18 The influence of pH value on the material removal selectivity between Ru and TEOS

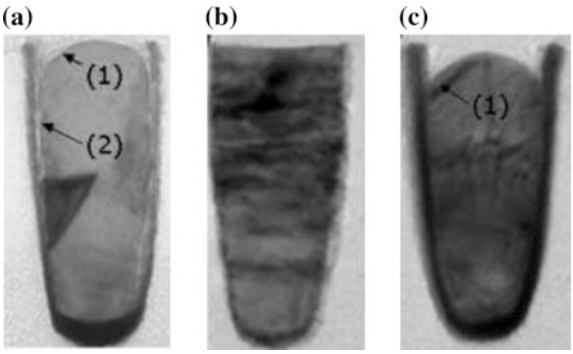

Fig. 1.19 The cross-sectional view of a 50 nm Cu wiring with a barrier layer of **a** Ta(N)/Co; **b** RuTa; **c** Ta(N)/Ta. *1* Galvanic corrosion; *2* chemical dissolution

boost the corrosion of Cu. After that, the MRR of Ru continuously decreases while that of Cu increases as the concentration of glycine goes up.

Investigation of Galvanic Corrosion Galvanic corrosion resulted from the direct contact of different metals in slurry is a severe problem generated during CMP. Normally, Ru has a higher corrosion potential, which acts as the cathode while Cu as the anode. Therefore, Ru is protected but the corrosion of Cu is often accelerated, that is, the galvanic corrosion between Ru and Cu. The galvanic corrosion between Cu and barrier will deteriorate the interfacial quality after CMP, even cause failure of interconnects. The galvanic corrosion between Ru and Cu is similar with that shown in Fig. 1.19c.

It is found that the potential difference (ΔE_{cor}) between Ru and Cu is up to 0.6 V in KIO_4-based slurry at pH 9 (Peethala et al. 2011). Researchers have tried to find suitable inhibitors to decrease ΔE_{cor} measured by electrochemical methods. Results show that when the slurry contains 5 mM benzotriazole (BTA) and 7 mM ascorbic acid (AA) as inhibitors, ΔE_{cor} could be effectively reduced, indicating that the galvanic corrosion between Ru and Cu is mitigated. However, due to the reducibility, AA might react with KIO_4, thus lowering the effective content of oxidant. At the same time, AA is oxidized to dehydroascorbate (DHA). Therefore, the galvanic corrosion inhibition of BTA and AA needs further investigation.

Non-ionic surfactant Pluronic® P123, together with BTA, could effectively lower the anodic polarization current of Cu in KIO_4-based slurry (Jiang et al. 2014a, b, c). By CMP experiments it is found that the MRR of Cu decreases after the addition of Pluronic® P123. The results show that BTA and Pluronic® P123 are suitable galvanic corrosion inhibitors for Ru/Cu coupling.

It should be noted that the detrimental effects resulted from galvanic corrosion are microscopic and local. To be exact, it is unsuitable to study the interfacial defects caused by galvanic corrosion using macroscopic methods. The development of micro-galvanic corrosion at Cu/Ru interface in 0.1 M ammonium citrate solution at pH 9.5 is displayed in Fig. 1.20 (Nalla 2006). Results show that the corrosion initiates at the Cu/Ru interface, resulting in pitting and dissolution of Cu. By further comparison with sodium citrate, it is found that the NH_4^+ plays an important role in boosting the galvanic corrosion of Cu.

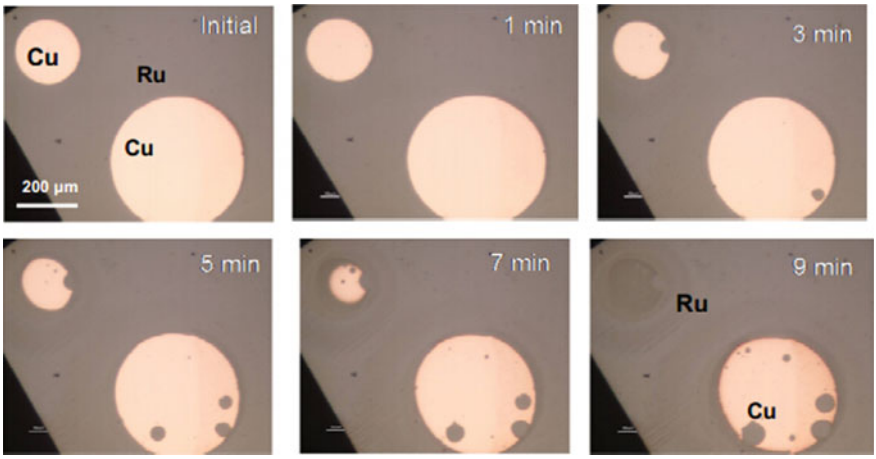

Fig. 1.20 Galvanic corrosion of Cu micro-pattern on Ru wafer observed by optical microscope

1.4.3 Existing Problems in the CMP of Ru

Ru, as a novel diffusion barrier material, the CMP process of which still needs in-depth and systematic investigations when polished using a specific slurry. The remaining problems are discussed as follows:

- The material removal mechanism of Ru and Cu during barrier layer polishing is not revealed yet. The dominating factor of material removal during polishing is not clear. Traditional investigations often focus on separated studies such as static corrosion, material removal rate, and surface quality. Therefore, investigations based on the chemical-mechanical synergistic effect need to be done to establish a tribocorrosion system, analyzing the relationship between surface chemistry, tribocorrosion properties, surface quality and polishing rate. On this basis, the material removal mechanism of Cu and Ru could be proposed.
- A proper selection of corrosion inhibitor is needed. Existing investigations of inhibitors are mainly about the corrosion inhibition effects on Ru. However, due to the high hardness and chemical inertness of Ru, it is easy to get a good polished surface of Ru after CMP. On the contrary, the surface quality of Cu after polishing in the KIO_4-based slurry is often bad because of the complex chemical reaction products formed on Cu surface. The corrosion inhibition mechanism on Cu should become the research emphasis.
- Microscopic investigations are needed for the initiation and development of galvanic corrosion between Ru and Cu. The commonly used method is the macroscopic electrochemical method, on the basis of which to calculate the corrosion rate. Therefore, this method is not suitable to thoroughly investigate the galvanic corrosion mechanism from the micro-perspective.

- The CMP data of patterned wafer with Ru as barrier layer are insufficient. Presently most of the labs carry out experiments using PVD Ru blanket wafer or target Ru. There is big difference generated in the CMP results using the patterned wafer and the blanket wafer. Therefore, relevant investigations should be carried out using the Ru patterned wafer, the results of which could be inspiring to the real industrial production.

1.5 Main Content of the Thesis

To solve the remaining critical issues during the CMP process of Ru, a systematic research work has been carried out in this thesis. The tribocorrosion properties and the material removal mechanism of Cu and Ru in KIO_4-based slurry were firstly investigated. The Cu/Ru galvanic corrosion was then studied from a new micro and in situ perspective, and on this basis, ways to mitigate corrosion using different inhibitors were subsequently sought for.

With a combination of the surface chemistry analysis, electrochemical experiments, and CMP test methods, the material removal mechanism of Cu and Ru was comprehensively investigated. Results show that for both Cu and Ru, the predominant material removal mechanism is the chemical-mechanical synergistic effect. When weak alkaline slurry is used during the barrier polishing process, an inhomogeneous $CuO/Cu(IO_3)_2 \cdot nH_2O$/Cu-periodate/CuI passive film is formed on Cu, while $RuO_2 \cdot 2H_2O/RuO_3$ on Ru. The surface films have good passivation property and weak mechanical strength, which result in a significant mechanical accelerated chemical effect during polishing. Therefore, under weak alkaline condition, ideal polishing results could be achieved, i.e., a better surface quality, and a good material removal selectivity between Cu and Ru.

CMP-electrochemical experiments combined with the traditional tribocorrosion experiments were conducted to investigate the tribocorrosion properties of Cu and Ru. Results show that the nature of tribocorrosion phenomenon is the galvanic corrosion between the mechanical abrasion induced depassivation area and the passivation area on metal surface. The external mechanical energy is imported into the system, accelerating the anodic reaction of Cu corrosion and cathodic reaction of Ru corrosion, respectively. When using alkaline slurry during CMP, there is obvious tribocorrosion effect for Cu and Ru, which is caused by both the convection enhanced corrosion and the mechanical abrasion enhanced corrosion.

The generation and development of galvanic corrosion within the Cu/Ru couple were studied from an in situ and micro perspective mainly using the scanning probe microscopy methods. The development of Cu/Ru micro-galvanic corrosion could be divided into three stages: (1) the galvanic corrosion immune stage, the Cu surface is passivated by the native oxide layer formed in the air, which could prevent Cu from the accelerated corrosion; (2) Cu corrosion accelerating stage, the breakdown of the native oxide layer results in the sharply accelerated corrosion of

Cu, and simultaneously large amount of insoluble reaction product Cu $(IO_3)_2 \cdot nH_2O$ initiates from the Cu/Ru interface and spreads to the whole Cu surface within a short period; (3) galvanic corrosion stabilization stage, the insoluble $Cu(IO_3)_2 \cdot nH_2O$ acts as the corrosion obstruction again, decelerating the corrosion of Cu, and the galvanic corrosion is stabilized henceforward.

The effects of different oxidants and corrosion inhibitors on the galvanic corrosion within Cu/Ru couple were investigated by electrochemical methods based on the principle of galvanic corrosion meter. It is proved that compared with hydrogen peroxide, the galvanic corrosion rate is lower when using KIO_4 as the oxidant. BTA and 1,2,4-triazole are effective galvanic corrosion inhibitors with high corrosion inhibition efficiency. Apart from this, BTA-potassium molybdate (K_2MoO_4) are effective compound corrosion inhibitors in KIO_4-based slurry. MoO_4^{2-} preferentially adsorbs on metal surface, increasing the activation energy of the electrode reactions. Meanwhile, the compound corrosion inhibitors could enhance the physical adsorption of MoO_4^{2-}-BTA passivation film, with insoluble molybdate salts deposited in the gaps, improving the surface passivation property. Not only could the compound corrosion inhibitors effectively suppress the galvanic corrosion within Cu/Ru coupling, but also achieve good material removal selectivity between Cu and Ru.

References

Alén P, Vehkamäki M, Ritala M, Leskelä M (2006) Diffusion barrier properties of atomic layer deposited ultrathin Ta_2O_5 and TiO_2 films. J Electrochem Soc 153(4):G304–G308

Antonelli GA, Jiang G, Shaviv R, Mountsier T, Dixit G, Park KJ, Karim I, Wu W, Shobha H, Spooner T (2012) Synergistic combinations of dielectrics and metallization process technology to achieve 22 nm interconnect performance targets. Microelectron Eng 92:9–14

Arunagiri TN, Zhang Y, Chyan O, Kim MJ, Hurd TQ (2005a) Interfacial diffusion studies of Cu/(5 nm Ru)/Si structures physical vapor deposited vs electrochemically deposited Cu. J Electrochem Soc 152(11):G808–G812

Arunagiri TN, Zhang Y, Chyan O, El-Bouanani M, Kim MJ, Chen KH, Wu CT, Chen LC (2005b) 5 nm ruthenium thin film as a directly plateable copper diffusion barrier. Appl Phys Lett 86(8):83104

Baklanov M, Maex K, Green M (2007) Dielectric films for advanced microelectronics. Wileys, Hoboken

Balakumar S, Haque T, Kumar AS, Rahman M, Kumar R (2005) Wear phenomena in abrasive-free copper CMP process. J Electrochem Soc 152(11):G867–G874

Balan V, Euvard C, Seognard A, Chaffard C, Gourvest E, Gaillard S, Rivoire M (2013) Tungsten CMP process Investigation for FDSOI 14 nm and beyond. Paper presented at the International Conference on Planarization/CMP Technology, Taipei, 29 October–1 November

Bard AJ, Parsons R, Jordan J (1985) Standard potentials in aqueous solution. CRC Press, New York

Behera SP, Wang Q, Kelber JA (2011) He plasma pretreatment effects on oxygen plasma-induced carbon loss and surface roughening in an ultralow-k organosilicate glass film. J Phys D Appl Phys 44(15):155204

Brown C (2012) Chemical mechanical polishing of Ruthenium, cobalt, and black diamond films. Dissertation, Clarkson University

Cao L, Zhang L, Ho PS, Justison P, Hauschildt M (2014) Scaling effects on microstructure and electromigration reliability for Cu and Cu (Mn) interconnects. Paper presented at the Reliability Physics Symposium, 2014 IEEE International, Waikoloa

Chai Z, Lu X, He D (2012) Atomic layer deposition of zinc oxide films: effects of nanocrystalline characteristics on tribological performance. Surf Coat Technol 207:361–366

Chan R, Arunagiri TN, Zhang Y, Chyan O, Wallace RM, Kim MJ, Hurd TQ (2004) Diffusion studies of copper on ruthenium thin film a plateable copper diffusion barrier. Electrochem Solid State Lett 7(8):G154–G157

Chen C, Liu C, Yang H, Tsao CY (2004a) Influence of the preferred orientation and thickness of zirconium nitride films on the diffusion property in copper. J Vac Sci Technol B 22(3): 1075–1083

Chen C, Chen J, Jeng J (2009) Characteristics of thermally robust 5 nm Ru-C diffusion barrier/Cu seed layer in Cu metallization. J Electrochem Soc 156(9):H724–H728

Cheng J, Wang T, Jiang L, Lu X (2015) Surface characteristics of ruthenium in periodate-based slurry during chemical mechanical polishing. Appl Surf Sci 351:401–409

Chenwei W, Suohui M, Yuling L, Rui C, Yang C (2013) CMP process optimization using alkaline bulk copper slurry on a 300 mm Applied materials reflexion LK system. J Semiconductors 34 (12):126001

Chuang J, Tu S, Chen M (1999) Sputter-deposited Mo and reactively sputter-deposited Mo-N films as barrier layers against Cu diffusion. Thin Solid Films 346(1):299–306

Connick RE, Hurley CR (1952) Chemistry of Ru(VI), -(VII) and -(VIII). Reactions, oxidation potentials and spectra. J Am Chem Soc 74(20):5012–5015

Cui H, Park J, Park J (2013) Effect of oxidizers on chemical mechanical planarization of ruthenium with colloidal silica based slurry. ECS J SOLID STATE SC 2(1):P26–P30

Fischer K, Agostinelli M, Allen C, Bahr D, Bost M, Charvat P, Chikarmane V, Fu Q, Ganpule C, Haran M (2015) Low-k interconnect stack with multi-layer air gap and tri-metal-insulator-metal capacitors for 14 nm high volume manufacturing. Paper presented at the Interconnect Technology Conference and 2015 IEEE Materials for Advanced Metallization Conference (IITC/MAM), 2015 IEEE International, Grenoble

Gibson JG, Sudworth JL (1973) Specific energies of galvanic reactions, and related thermodynamic data. Chapman and Hall, London

Goldberg C, Kuo S (2003) Analysis of flip-chip packaging challenges on copper/low-k interconnects. IEEE Trans Device MAT Reliab 3(4):111–118

Gottfried K, Schubert I, Schulz SE, Gessner T (2006) Cu/barrier CMP on porous low-k based interconnect schemes. Microelectron Eng 83(11):2218–2224

Griffith WP (2010) Ruthenium oxidation complexes: their uses as homogenous organic catalysts. Springer Science & Business Media, New York

He Y, Feng JY (2004) Diffusion barrier performances of direct current sputter-deposited Mo and Mo × N films between Cu and Si. J Cryst Growth 263(1):203–207

He ZW, Liu XQ, Xu DY, Su Q, Guo DF, Wang YY (2005) Characteristic of nanoporous SiO_2 thin film prepared by sol-gel method with catalyst HF. Mater Sci Forum 475:1733–1736

He GH, Yao L, Song ZX, Li, Xu KW (2012) Diffusion barrier performance of nano-structured and amorphous Ru-Ge diffusion barriers for copper metallization. Vacuum 86(7SI), 965–969

Hill AE (1928) Ternary systems. VII. The periodates of the alkali metals. J Am Chem Soc 50(10):2678–2692

Iacopi F, Brongersma SH, Vandevelde B, O'Toole M, Degryse D, Travaly Y, Maex K (2004) Challenges for structural stability of ultra-low-k-based interconnects. Microelectron Eng 75(1):54–62

Ingerly D, Agrawal A, Ascazubi R, Blattner A, Buehler M, Chikarmane V, Choudhury B, Cinnor F, Ege C, Ganpule C (2012) Low-k interconnect stack with metal-insulator-metal capacitors for 22 nm high volume manufacturing. Paper presented at the Interconnect Technology Conference (IITC), 2012 IEEE International, San Jose

Ishikawa A, Shishida Y, Yamanishi T, Hata N, Nakayama T, Fujii N, Tanaka H, Matsuo H, Kinoshita K, Kikkawa T (2006) Influence of CMP chemicals on the properties of porous silica low-k films. J Electrochem Soc 153(7):G692–G696

Iwai H (2009) Roadmap for 22 nm and beyond. Microelectron Eng 86(7):1520–1528

Jiang L, Lan Y, He Y, Li Y, Luo J (2014a) Functions of Trilon® P as a polyamine in copper chemical mechanical polishing. Appl Surf Sci 288:265–274

Jiang L, He Y, Li Y, Luo J (2014b) Effect of ionic strength on ruthenium CMP in H_2O_2-based slurries. Appl Surf Sci 317:332–337

Jiang L, He Y, Lu X, Luo J (2014c) Investigation on the galvanic corrosion of copper during chemical mechanical polishing of ruthenium barrier layer. Paper presented at the International Conference on Planarization/CMP Technology, Kobe

Josell D, Wheeler D, Witt C, Moffat TP (2003) Seedless superfill: copper electrodeposition in trenches with ruthenium barriers. Electrochem Solid State Lett 6(10):C143–C145

Josell D, Witt C, Moffat TP (2006) Osmium barriers for direct copper electrodeposition in damascene processing. Electrochem Solid State Lett 9(2):C41–C43

Kim H, Koseki T, Ohba T, Ohta T, Kojima Y, Sato H, Shimogaki Y (2005) Cu wettability and diffusion barrier property of Ru thin film for Cu metallization. J Electrochem Soc 152(8): G594–G600

Kim N, Seo Y, Lee W (2006) Temperature effects of pad conditioning process on oxide CMP: polishing pad, slurry characteristics, and surface reactions. Microelectron Eng 83(2):362–370

Kim I, Kang Y, Kwon T, Cho B, Park J, Park J, Park H (2008) Effect of sodium periodate in alumina-based slurry on Ru CMP for metal-insulator-metal capacitor. Electrochem Solid State Lett 11(6):H150–H153

Kim I, Cho B, Park J, Park J, Park H (2009) Effect of pH in Ru slurry with sodium periodate on Ru CMP. J Electrochem Soc 156(3):H188–H192

Kohama K, Ito K, Sonobayashi Y, Mori K, Maekawa K, Shirai Y, Murakami M (2010) Characterization of self-formed Ti-based barrier layers in Cu (Ti)/dielectric-layer samples using X-ray Photoelectron Spectroscopy. Paper presented at the Interconnect Technology Conference (IITC), 2010 International, Burlingame

Kohn A, Eizenberg M, Shacham-Diamand Y, Sverdlov Y (2001) Characterization of electroless deposited Co (W, P) thin films for encapsulation of copper metallization. Mater Sci Eng, A 302(1):18–25

Krishnan M, Nalaskowski JW, Cook LM (2009) Chemical mechanical planarization: slurry chemistry, materials, and mechanisms. Chem Rev 110(1):178–204

Kumar S (2008) ALD growth of a novel mixed-phase barrier for seedless copper electroplating applications. Dissertation, State University of New York at Albany

Lee W, Park H (2004) Development of novel process for Ru CMP using ceric ammonium nitrate (CAN)-containing nitric acid. Appl Surf Sci 228(1):410–417

Lee W, Park H, Lee S, Sohn H (2004) Effects of ceric ammonium nitrate (CAN) additive in HNO3 solution on the electrochemical behaviour of ruthenium for CMP processes. J Appl Electrochem 34(1):119–125

Leskelä M, Ritala M (2003) Atomic layer deposition chemistry: recent developments and future challenges. Angew Chem Int Ed 42(45):5548–5554

Li Z, Borucki L, Koshiyama I, Philipossian A (2004) Effect of slurry flow rate on tribological, thermal, and removal rate attributes of copper CMP. J Electrochem Soc 151(7):G482–G487

Li Z, Gordon RG, Farmer DB, Lin Y, Vlassak J (2005) Nucleation and adhesion of ALD copper on cobalt adhesion layers and tungsten nitride diffusion barriers. Electrochem Solid State Lett 8(7):G182–G185

Liu X, Liu Y, Liang Y, Liu H, Hu Y, Gao B (2011) Optimization of slurry components for a copper chemical mechanical polishing at low down pressure using response surface methodology. Microelectron Eng 88(1):99–104

Massalski TB, Okamoto H, Subramanian PR, Kacprzak L (1990) Binary alloy phase diagrams (seconded). ASM international, Metals Park

Mosig K, Jacobs T, Brennan K, Rasco M, Wolf J, Augur R (2002) Integration challenges of porous ultra low-*k* spin-on dielectrics. Microelectron Eng 64(1):11–24

Nalla PR (2006) Interfacial studies of bimetallic corrosion in copper/ruthenium systems and silicon surface modification with organic and organometallic chemistry. Dissertation, University of North Texas

Nguyen VH, Hof AJ, Van Kranenburg H, Woerlee PH, Weimar F (2001) Copper chemical mechanical polishing using a slurry-free technique. Microelectron Eng 55(1):305–312

Oliver MR (2013) Chemical-mechanical planarization of semiconductor materials. Springer Science & Business Media, New York

Oliver MR, Schmidt RE, Robinson M (2001) CMP pad surface roughness and CMP removal rate. Electrochem Soc S 26:77–83

Ono H, Nakano T, Ohta T (1994) Diffusion barrier effects of transition metals for Cu/M/Si multilayers (M=Cr, Ti, Nb, MO, Ta, W). Appl Phys Lett 64(12):1511–1513

Peethala BC, Babu SV (2011) Ruthenium polishing using potassium periodate as the oxidizer and silica abrasives. J Electrochem Soc 158(3):H271–H276

Peethala BC, Roy D, Babu SV (2011) Controlling the galvanic corrosion of copper during chemical mechanical planarization of ruthenium barrier films. Electrochem Solid State Lett 14(7):H306–H310

Posseme N, Chevolleau T, David T, Darnon M, Barnes JP, Louveau O, Licitra C, Jalabert D, Feldis H, Fayolle M (2008) Efficiency of reducing and oxidizing ash plasmas in preventing metallic barrier diffusion into porous SiOCH. Microelectron Eng 85(8):1842–1849

Praveen B, Manivannan R, Umashankar TD, Cho B, Park J, Ramanathan S (2014) Abrasive and additive interactions in high selectivity STI CMP slurries. Microelectron Eng 114:98–104

Rao C, Wang T, Wang J, Liu Y, Lu X (2016) Improvement of via dishing and non-uniformity in TSV chemical mechanical planarization. Microelectron Eng 151:38–46

Roule A, Amuntencei M, Deronzier E, Haumesser PH, Da Silva S, Avale X, Pollet O, Baskaran R, Passemard G (2007) Seed layer enhancement by electrochemical deposition: the copper seed solution for beyond 45nm. Microelectron Eng 84(11):2610–2614

Seddon EA, Seddon KR (2013) The chemistry of ruthenium. Elsevier, Amsterdam

Shima S, Fukunaga A, Tsujimura M (2007) Effects of liner metal and CMP slurry oxidizer on copper galvanic corrosion. ECS Trans 11(6):285–295

Steigerwald JM, Murarka SP, Gutmann RJ (2008) Chemical mechanical planarization of microelectronic materials. Wiley, London

Tada M, Abe M, Ohtake H, Furutake N, Tonegawa T, Motoyama K, Tohara M, Ito F, Ueki M, Takeuchi T (2006) A metallurgical prescription for electromigration (EM) reliability improvement in scaled-down, Cu dual damascene interconnects. Paper presented at the Interconnect Technology Conference, 2006 International, Burlingame

Tan J, Qu X, Xie Q, Zhou Y, Ru G (2006) The properties of Ru on Ta-based barriers. Thin Solid Films 504(1–2):231–234

Tano H, Yokoi K, Nishimura H, Maekawa A, Hirao T, Kamo S (2014) Advanced Cu CMP pad for reducing scratches. Paper presented at the 2014 International Conference on Planarization/ CMP Technology (ICPT), Kobe

Tseng WT, Wang YL (1997) Re-examination of pressure and speed dependences of removal rate during chemical-mechanical polishing processes. J Electrochem Soc 144(2):L15–L17

Urzo LD, Schaltin S, Shkurankov A, Plank H, Kothleitner G, Gspan C, Binnemans K, Fransaer J (2012) Direct-on-barrier copper electroplating on ruthenium from the ionic liquid 1-ethyl-3-methylimidazolium dicyanamide. J Mater Sci Mater Electron 23(4):945–951

Usui T, Nasu H, Takahashi S, Shimizu N, Nishikawa T, Yoshimaru M, Shibata H, Wada M, Koike J (2006) Highly reliable copper dual-damascene interconnects with self-formed $MnSi_xO_y$ barrier layer. Electron Devices IEEE Trans 53(10):2492–2499

Van der Velden P (2000) Chemical mechanical polishing with fixed abrasives using different subpads to optimize wafer uniformity. Microelectron Eng 50(1):41–46

Venkataraman SS (2012) Interfacial chemistry in chemical mechanical planarization of metals and non-metals for microelectronic applications. Dissertation, Clarkson University

Victoria SN, Sharma PP II, Suni S Ramanathan (2010) Potassium bromate as an oxidizing agent in a titania-based Ru CMP slurry. Electrochem Solid State Lett 13(11):H385–H387

Victoria SN, Jebaraj J II, Suni S Ramanathan (2011) Chemical mechanical planarization of ruthenium with oxone as oxidizer. Electrochem Solid State Lett 15(3):H55–H58

Wang DH, Chiao S, Afnan M, Yih P, Rehayem M (2001) Stress-free polishing advances copper integration with ultralow-k dielectrics. Solid State Technol 44(10):101

Wang YH, Kumar R, Zhou X, Pan JS, Chai JW (2005) Effect of oxygen plasma treatment on low dielectric constant carbon-doped silicon oxide thin films. Thin Solid Films 473(1):132–136

Wei Z, Xinchun L, Yuhong L, Guoshun P, Jianbin L (2009) Effect of pH on material removal rate of Cu in abrasive-free polishing. J Electrochem Soc 156(3):H176–H180

Widmann D, Mader H, Friedrich H (2013) Technology of integrated circuits. Springer Science & Business Media, Berlin

Wilson L (2013) International Technology Roadmap for Semiconductors (ITRS). Semiconductor Industry Association

Wojcik H, Kaltofen R, Krien C, Merkel U, Wenzel C, Bartha JW, Friedemann M, Adolphi B, Liske R, Neumann V, Geidel M (2011) Investigations on Ru-Mn films as plateable Cu diffusion barriers. Paper presented at the Interconnect Technology Conference and 2011 Materials for Advanced Metallization (IITC/MAM), 2011 IEEE International, Dresden

Wong T, Liu B, Narayanan B, Ligatchev V, Kumar R (2004) Investigation of deposition temperature effect on properties of PECVD SiOCH low-k films. Thin Solid Films 462:156–160

Zeng X, Wang J, Lu H, Chen F, Zhang X, Qu X (2012) Improved removal selectivity of ruthenium and copper by glycine in potassium periodate (KIO_4)-based slurry. J Electrochem Soc 159(11): C525–C529

Zheng DW, Xu YH, Tsai YP, Tu KN, Patterson P, Zhao B, Liu Q, Brongo M (2000) Mechanical property measurement of thin polymeric-low dielectric-constant films using bulge testing method. Appl Phys Lett 76(15):2008–2010

Zhu Y, Dunn K, Kaloyeros A (2006) Platinum liner deposited by atomic layer deposition for Cu interconnect application. ECS Trans 1(10):63–69

Zimmerman GL, Riviello SJ, Glauser TA, Kay JG (1990) Photochemical decomposition of ruthenium tetroxide. J Phys Chem 94(6):2399–2404

Chapter 2
Material Removal Mechanism of Cu in KIO_4-Based Slurry

2.1 Experimental

2.1.1 Static Etch Experiments

To avoid any disturbing factors during immersion, the solutions only contained DI water and analytic reagents (Sinopharm Chemical Reagent Co., Ltd), excluding the abrasive particles. The reagent was 0.015 M KIO_4. The pH values of solutions were adjusted to 4, 6, 9 and 11, with diluted H_2SO_4/NaOH as pH adjustors. Samples were electroplated Cu on SiO_2/Si substrates (Wuhan Research Institute of Materials Protection). The thickness of Cu is 10 μm. Within an area of 173 μm × 173 μm, the surface roughness (Ra) is 53.6 (10.4) nm, and the local (5 μm × 5 μm) Ra is less than 1 nm, as is shown in Fig. 2.1.

Prior to the experiments, the Cu samples were cut into squares and immersed in 0.05 M citric acid (pH ≈ 2) for 5 min to remove the native oxide layer, and then cleaned in absolute ethyl alcohol and dried using a N_2 gas stream. After that, the Cu samples were immersed in the solutions for 5 min and cleaned in DI water.

2.1.2 Characterization of Surface Film

The chemical and electrochemical reaction products on Cu surface were analyzed by X-ray photoelectron spectroscopy (PHI Quantera Scanning XPS Microprobe, ULVAC-PHI Inc.). The Cu 2p and I 3d XPS peaks were analyzed and the data were fitted by the XPSPEAK software. The surface morphology of Cu after the immersion experiments was observed using AFM (MFP-3D, Asylum Research) and scanning electron microscopy (SEM, FEI Quanta 200 FEG).

J. Cheng, *Research on Chemical Mechanical Polishing Mechanism of Novel Diffusion Barrier Ru for Cu Interconnect*, Springer Theses,
DOI 10.1007/978-981-10-6165-3_2

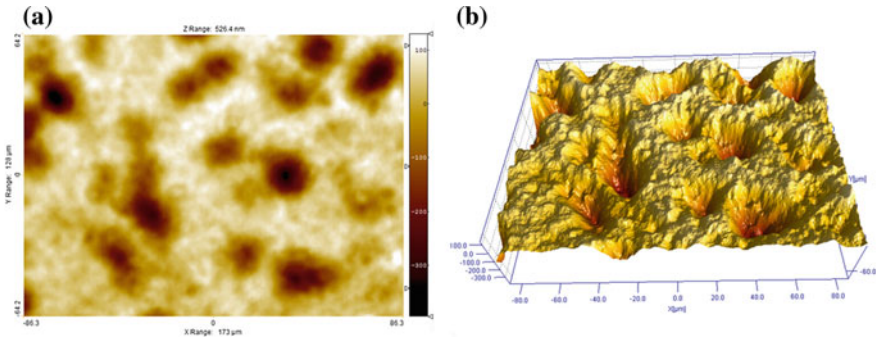

Fig. 2.1 The topography of electroplated Cu: **a** 2-D; **b** 3-D (MicroXAM, Veeco)

The thickness of the Cu surface passivation film was obtained by AES (PHI-700, Physical Electronics, Inc.) with a co-axial cylindrical mirror analyzer (CMA). The sputtering rate v was 5 nm/min or 18 nm/min according to the different surface film thickness. The v was calibrated by sputtering a standard SiO_2 film. During sputtering, when the percentage of Cu atom was up to 90%, the passivation film on Cu surface was believed to be totally removed, setting the terminal time (T). The calculation of film thickness δ is shown in Eq. 2.1.

$$\delta = \mathrm{T} \cdot v \tag{2.1}$$

2.1.3 Nano-Scratch Tests

During the CMP process, the film formed on wafer surface is often less than 100 nm in thickness, and the material removal process is an atomic-scale removal of surface film. The physical properties of surface film will be greatly influenced by the substrates if they are measured by nano-indentation method (Chen and Bull 2009). Therefore, AFM technique was applied to conduct the nano-scratch tests on Cu surface. Cu (99.99% purity) was cut into 20 mm × 20 mm × 2 mm squares. Before the experiments, the Cu samples were polished on a Struers bench top polisher (TegraPol-35) until Ra was below 3 nm, and then immersed into solutions containing 0.015 M KIO_4 with different pH values for 5 min as aforementioned. The nano-scratch experiments were performed using AFM (RTESP, Veeco Co.) with a silicon rectangular cantilever probe. Before each scratching, the surface topography (5 μm × 5 μm) was mapped under tapping mode. The scratching area was 2 μm × 2 μm and the constant applied force during scratching was 0.126 μN. The whole scratching process is illustrated in Fig. 2.2.

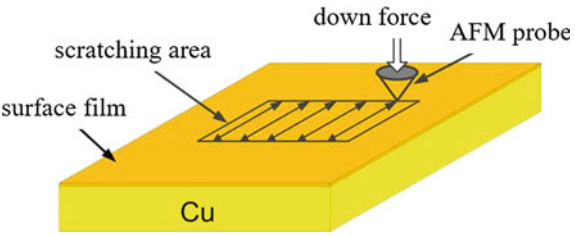

Fig. 2.2 Schematic diagram of nano-scratching experiment using AFM

2.1.4 CMP-Electrochemical Experiments

CMP-electrochemical experiments were carried out to study the electrochemical behavior of Cu during CMP. The apparatus was modified on a chemical mechanical polishing machine connected with an electrochemical workstation (CHI600C, Chenhua), as is shown in Fig. 2.3. The Cu sample (99.99%) was 12.5 mm in diameter and about 1 mm in thickness. The pad was IC1010/Suba IV and the slurry contained 0.015 M KIO_4 without abrasives. The pH was adjusted to 4, 6, 7, 9, 10 and 11, respectively. The counter electrode was Pt and the reference electrode was Ag/AgCl (3.5 M). Before polishing, the sample was hold at −1 V for 60 s to remove the native oxide. During polishing, the applied force on the Cu sample was 2.9 psi. The Cu sample was stationary and the pad rotated at a speed of 100 rpm. The potentiodynamic polarization experiments were conducted at a scan rate of 1 mV/s. The corrosion current density under both the polishing and static conditions has been calculated using the linear fitting method of E and Log (I) in Tafel strong polarization region thereafter (McCafferty 2005).

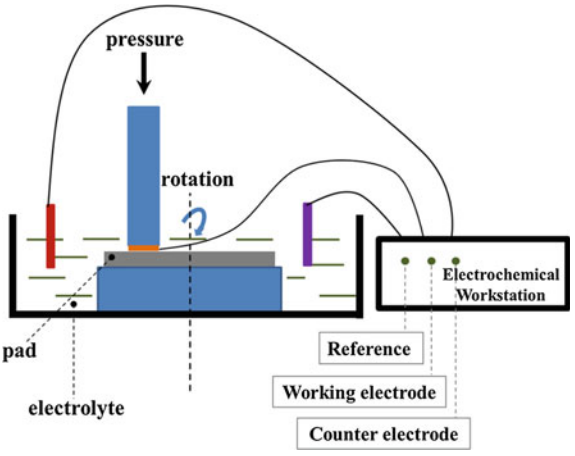

Fig. 2.3 The schematic diagram of CMP-electrochemical apparatus

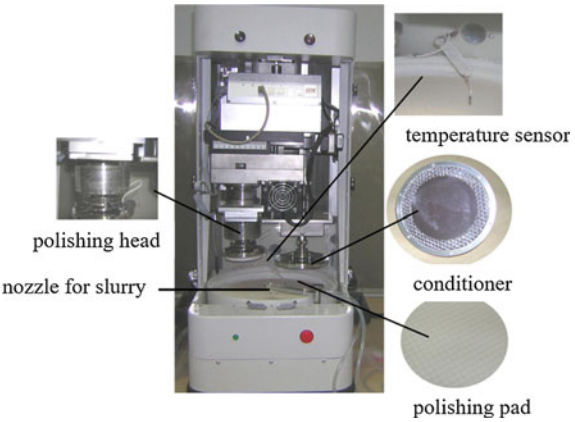

Fig. 2.4 CP-4 bench-top polisher

2.1.5 *Chemical Mechanical Polishing Experiments*

Electroplated Cu on a 2 inch wafer was used. A polisher (CP-4, CETR, shown in Fig. 2.4) was used with a platen/carrier speed of 100/100 and a slurry flow rate of 100 mL/min at a down pressure of 4 psi. The slurry contained 5% colloidal silica abrasive (Nexsil 85 k-40, Nyacol NanoTechnologies Inc.), and 0.015 M KIO_4 at different pH values. The pad was IC1010/Suba-IV (K-type groove, Dow Electronic Materials). The MRRs were measured using the weight-loss method after polishing for 1 min. Prior to the experiments, conditioning was carried out for 10 min. Between each polishing, a pad ex situ conditioning was executed for 45 s. The surface morphology after CMP was observed using an optical interferometer surface-mapping microscope (MicroXAM, Veeco).

The abrasive particle used in CMP experiments is colloidal SiO_2, the average diameter of which is 50 nm, negatively charged. The pH value of the sol is 8.6–9.8, and the dispersion morphology was observed by transmission electron microscope (TEM), as is shown in Fig. 2.5.

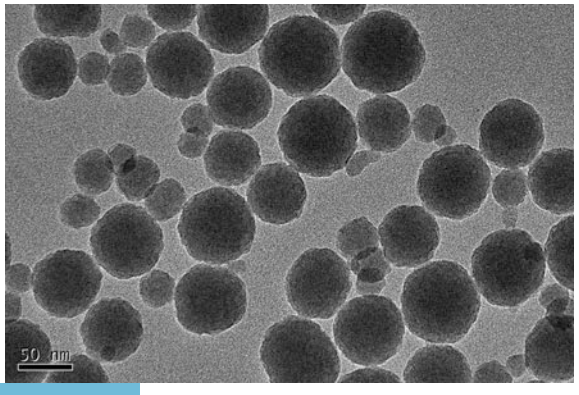

Fig. 2.5 The TEM image of colloidal SiO_2

2.2 Analysis of Cu Surface Chemistry

2.2.1 *Thermodynamic Parameters of Electrochemical Reactions*

During the corrosion of Cu, the electrode potential is the key factor to control the ionization of Cu while the pH value greatly affects the stability of the surface film. The relative stability regions of aqueous substances in a Cu-I-H_2O system are shown in the Pourbaix diagram (Eh-pH), presented in Fig. 2.6. The activities of I^- and Cu^{2+} are assumed equal to their [I^-] and [Cu^{2+}] concentrations, respectively. The equilibrium constant K used in Fig. 2.6 was calculated based on the change of Gibbs free energy, as is listed in Table 2.1, which corresponds well to the literature (Anik 2005). It is clear that the Cu surface reaction products in the periodate-based slurry are significantly more complex than those in H_2O_2-based slurry (Brusic et al. 1991; Zhang et al. 2009; Antonijevic and Petrovic 2008) The surface reaction products consist not only of copper oxides ($CuO/Cu_2O/Cu(OH)_2$), but also copper iodide (CuI), iodine (I_2) and copper iodate ($Cu(IO_3)_2 \cdot nH_2O$) (Luo 2000). However, as shown in Fig. 2.6, the Cu surface film composition varies with different pH values. The $Cu(IO_3)_2 \cdot nH_2O$ and I_2 are more likely to be present in more acidic solutions whereas the Cu surface tends to be covered with CuO and Cu_2O when the solution is extremely alkaline. The main cathodic reactions are listed below:

$$IO_4^- + H_2O + 2e^- = IO_3^- + 2OH^- \tag{2.2}$$

$$IO_3^- + 6H^+ + 6e^- = I^- + 3H_2O \tag{2.3}$$

$$2IO_3^- + 12H^+ + 10e^- = I_2 + 6H_2O \text{ (acidic solution)} \tag{2.4}$$

$$O_2 + 4H^+ + 4e^- = 2H_2O \tag{2.5}$$

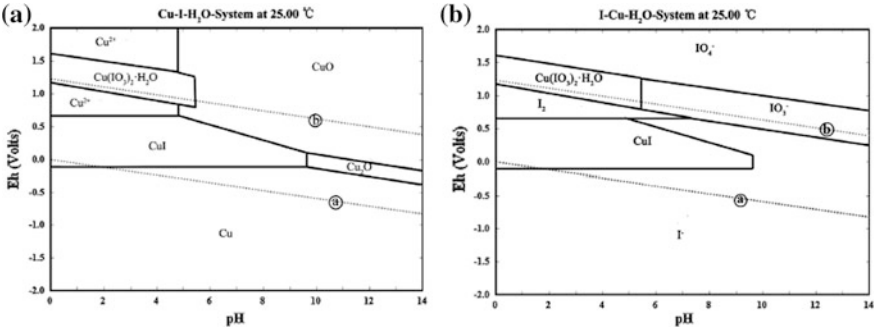

Fig. 2.6 Eh-pH diagram at 25 °C for **a** the Cu-I-H_2O system and **b** the I-Cu-H_2O system. [Cu^{2+}] = 10^{-2} M and [I^-] = 10^{-2} M

Table 2.1 Thermodynamic data for the Eh-pH diagrams of the Cu-I-H_2O system

Reactions	Log *K*
$Cu^{2+} + 2e^- \rightarrow Cu$	11.49
$2Cu^{2+} + H_2O + 2e^- \rightarrow Cu_2O\ (s) + 2H^+$	7.36
$Cu_2O\ (s) + 2H^+ + 2e^- \rightarrow 2Cu + H_2O$	15.625
$CuO\ (s) + 2H^+ \rightarrow Cu^{2+} + H_2O$	7.59
$Cu^{2+} + I^- + e^- \rightarrow CuI\ (s)$	15.30
$IO_4^- + 2e^- + 2H^+ \rightarrow IO_3^- + H_2O$	53.73
$IO_4^- + 8e^- + 8H^+ \rightarrow I^- + 4H_2O$	164.97
$Cu^{2+} + 2IO_3^- + H_2O \rightarrow Cu(IO_3)_2 \cdot H_2O\ (s)$	7.27
$IO_4^- + 7e^- + 8H^+ \rightarrow I_2\ (s) + 4H_2O$	155.87
$IO_3^- + 6H^+ + 6e^- \rightarrow I^- + 3H_2O$	111.27
$I_2\ (s) + 2e^- \rightarrow 2I^-$	18.20
$2IO_3^- + 12H^+ + 10e^- \rightarrow I_2\ (s) + 6H_2O$	204.28

In acidic solution, the main anodic reactions are:

$$2Cu + H_2O = 2H^+ + 2e^- \tag{2.6}$$

$$Cu = Cu^{2+} + 2e^- \tag{2.7}$$

In alkaline solution, the main anodic reactions are:

$$2Cu + 2OH^- = Cu_2O + H_2O + 2e^- \tag{2.8}$$

$$Cu_2O + 2OH^- = H_2O + 2CuO + 2e^- \tag{2.9}$$

Among the aforementioned chemical reaction products, Cu_2O, CuO, $Cu(OH)_2$, $Cu(IO_3)_2 \cdot nH_2O$, CuI and I_2 are slightly soluble or insoluble in water, which deposit or form on the Cu surface, together forming the surface layer on Cu in KIO_4 solutions.

2.2.2 *Characterization of Corrosion Products on Cu*

The opinion mentioned above is supported by XPS experiments. Figure 2.7 shows the XPS Cu 2p results on the Cu surface immersed into KIO_4 solutions with different pH values for 5 min. When the solution pH is 6 and 9, the Cu 2p3/2 peaks obviously shift to higher binding energies. At the same time, satellite peaks are observed between 940 and 945 eV, indicating the formation of CuO and $Cu(OH)_2$ (Deshpande et al. 2004; Hernandez et al. 2001). The deconvolution of the Cu 2p3/2 spectra on the untreated Cu surface show two peaks, at 933.8 eV (Peak 1) and 932.8 eV (Peak 2), corresponding to CuO and metallic Cu (Cu^0), respectively

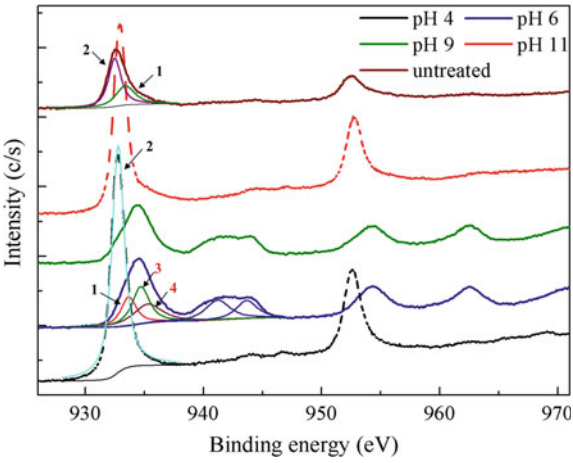

Fig. 2.7 The XPS data of Cu 2p on the Cu surface in 0.015 M KIO_4-based solutions at different pH values

(Du et al. 2004a, b; Cano et al. 2001). The similar analysis results are also obtained under pH 4 and 11 conditions, showing that the Cu surface is mainly composed of metallic Cu (Peak 2, 932.8 eV). However, for the pH 6 and 9 solutions, two peaks (Peak 3 and Peak 4) appear at higher binding energies (934.9 and 935.5 eV). There are insufficient supportive data to prove this, but the appearance of these two peaks is likely due to the formation of the $Cu(IO_3)_2 \cdot nH_2O$/Cu-periodate complex, which corresponds to previous Raman spectral data (Cheng et al. 2015; Sherwood 1976).

The deconvolution data of I 3d XPS spectra are shown in Fig. 2.8. The XPS of the I 3d core levels reveal two sharp and well-resolved peaks, corresponding to 3d5/2 (~620 eV) and 3d3/2 (~630 eV) spinorbit split levels. The peaks appearing at 619.4 and 630.5 eV indicate the presence of CuI (Lipton Duffin et al. 2009; Wijekoon et al. 1994; Gaarenstroom and Winograd 1977). The peak located at 619.9 eV refers to chemisorbed I_2, which clearly exists on the Cu surface under a pH 4 condition (Carley et al. 2004). It has been reported in the literature that the binding energy of the I 3d in $Cu(IO_3)_2$ is between 621.3 and 622.5 eV, but the binding energies for Cu-periodates are not clear because the reaction products are quite complex (Du et al. 2004a, b; NÄSÄNEN 1954; Wu et al. 1997). There is an apparent strong peak located at 624.2 eV, especially under the pH 6 and pH 9 conditions, which is the evidence for the presence of a $Cu(IO_3)_2 \cdot nH_2O$/Cu-periodate compound (Berry et al. 1989). Table 2.2 shows the atomic concentrations of the Cu, O, and I on Cu surface. The I concentration reaches the maximum at pH 6 and 9 (16.88% and 13.64%, respectively) due to the formation of the $Cu(IO_3)_2 \cdot nH_2O$ and $Cu(IO_4)_2$ complexes, as discussed earlier. The 11.20% I concentration under the pH 4 condition is caused by the formation of I_2 and CuI on Cu surface. However, when the solution is more alkaline, the element I on Cu surface was negligible (only 3.76%).

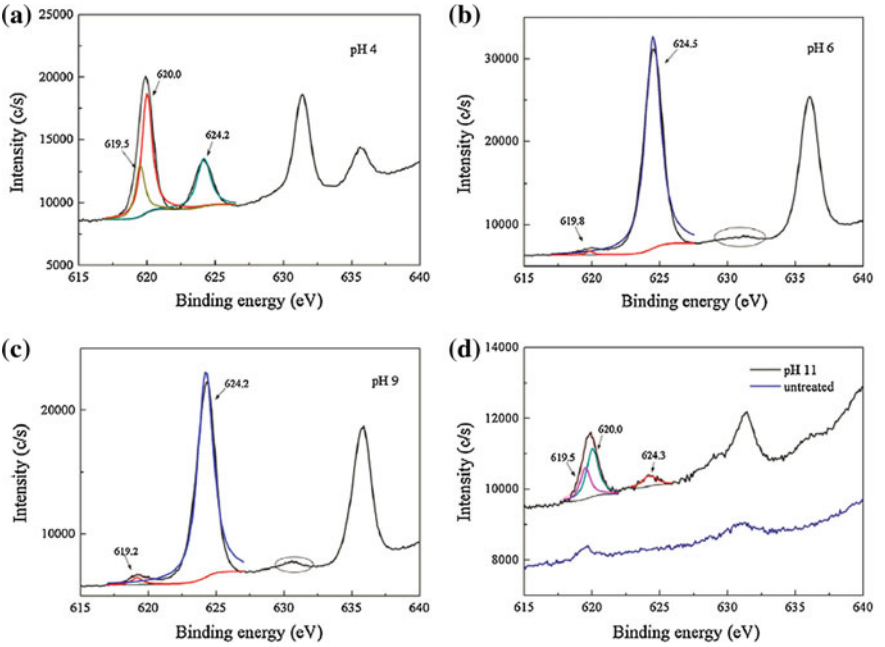

Fig. 2.8 The XPS data of I 3d on Cu surface in 0.015 M KIO_4-based solutions at pH values of **a** 4, **b** 6, **c** 9, **d** 11 and the untreated Cu surface

Table 2.2 Atomic concentrations obtained by XPS of the Cu surface

(%)	pH 4	pH 6	pH 9	pH 10	Untreated
Cu	41.09	19.69	18.59	36.33	24.90
O	47.71	63.43	67.77	59.91	73.10
I	11.20	16.88	13.64	3.76	2.00

2.3 Mechanical Properties of Cu Surface Film

2.3.1 Surface Morphology

The Cu surface morphology and surface average roughness after being immersed in the KIO_4 solutions are shown in Fig. 2.9. At pH 11, the surface roughness remained almost unchanged from the untreated Cu surface, indicating a uniform and mild corrosion proceeding on the Cu surface (Fig. 2.9d, e). However, severe corrosion occurred when the solution was acidic, especially when the pH value was 6, as is shown in Fig. 2.9a, b. These results correspond well with the SEM images of the immersed Cu surface, as are demonstrated in Fig. 2.10. It is obvious that at pH 6 and pH 9, the Cu surface was in the typical oxidized state, which is in line with the previous investigation (Liao et al. 2012). As can be seen in Fig. 2.10b, c, the

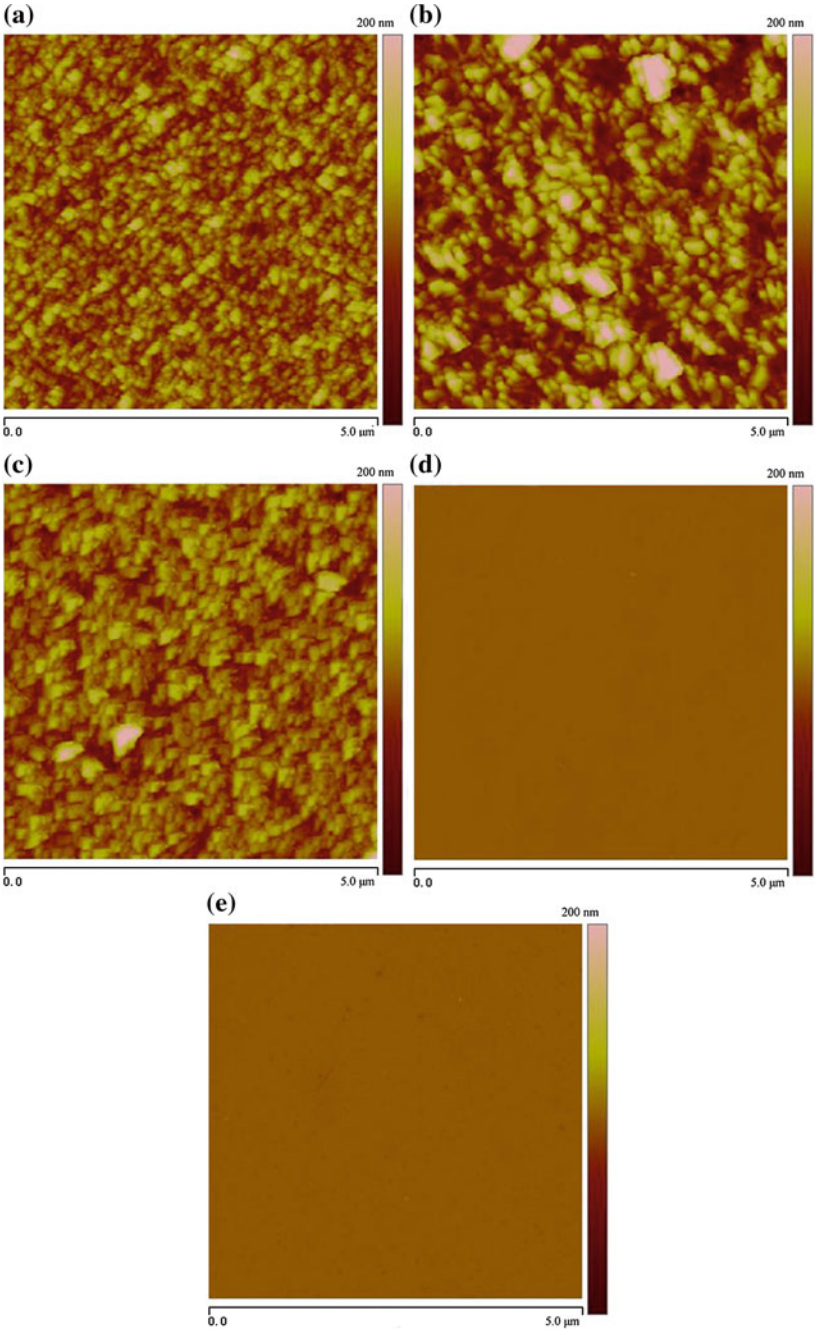

Fig. 2.9 The Cu surface topography after a 5 min immersion in 0.015 M KIO_4 at pH values of **a** 4, **b** 6, **c** 9, **d** 11, and **e** the untreated Cu surface. The average roughness (Ra) was **a** 23.84 nm, **b** 24.97 nm, **c** 12.70 nm, **d** 0.28 nm, and **e** 0.39 nm

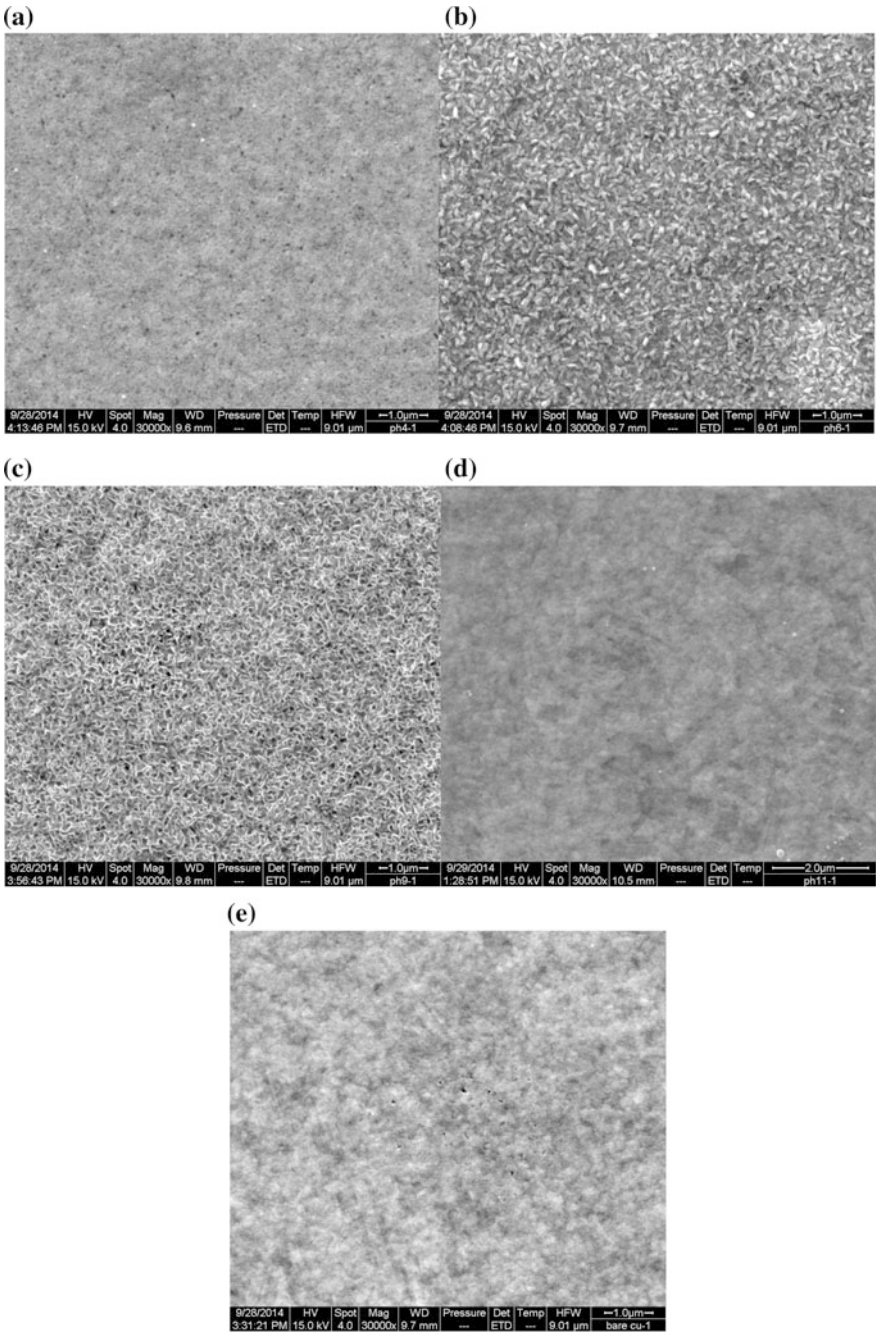

Fig. 2.10 SEM images of the Cu surface after a 5 min immersion in 0.015 M KIO_4 at pH values of **a** 4, **b** 6, **c** 9, **d** 11, and **e** the untreated Cu surface

surface oxidation films are non-uniform, indicating that the $Cu(IO_3)_2 \cdot nH_2O$/Cu-periodate/copper oxide films have a poor surface quality. The corrosion current during the CMP at pH 4 provides the highest value, due to the strong oxidative ability of KIO_4 under acidic conditions, in addition to the poor passivation effect of the CuI/I_2 surface films (Pourbaix 1974). The passivation and pitting properties of Cu could be evaluated by cyclic potentiodynamic polarization, which will be discussed later in Sect. 2.4.

2.3.2 *Corrosion-Enhanced Mechanical Abrasion*

In order to characterize the thickness of the corrosion products on Cu surface in KIO_4-based solutions, a semi-quantitative analysis was done by AES experiments. Figure 2.11a shows the element depth profiles of the Cu surface films under a pH 6 condition. After 4 min, the Cu atomic concentration increases to greater than 90%, and the film thickness is estimated to about 72 nm. Figure 2.11b shows the calculated surface film thickness based on the AES data. It is evident that the surface film thickness increases as the pH value decreases, indicating that in acidic solutions the Cu electrochemical and chemical reaction products are more likely to adsorb on the surface rather than directly dissolute in the solution. The explanation is supported by the Eh-pH diagram of Cu. When solution contains H_2O_2 as oxidant at pH 4, the existence form of Cu is Cu^{2+}. However, when solution contains KIO_4 as oxidant, Cu^{2+} could further react with iodine, forming insoluble compounds like CuI, I_2, and $Cu(IO_3)_2 \cdot nH_2O$. The insolubles could deposit on Cu surface, making the surface layer thicker under this condition.

It is worth noting that the element depth analysis by AES could only be used to semiquantitatively compare the thickness of Cu surface layer under different pH conditions. The reasons are listed as follows: (1) the sputtering speed v is calibrated by a standard SiO_2 sample, and v could vary according to different metal samples;

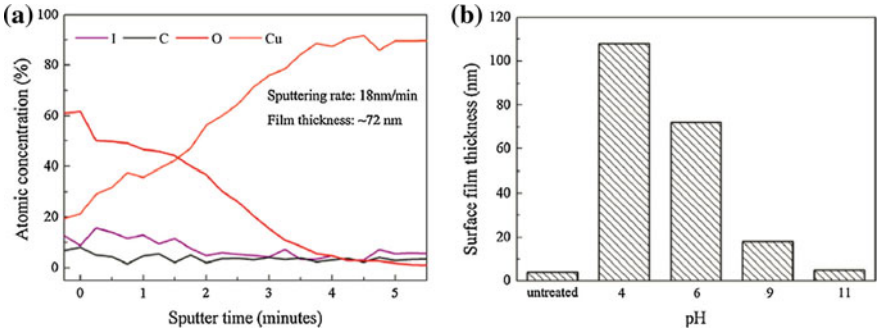

Fig. 2.11 AES results of the Cu surface after a 5 min immersion in 0.015 M KIO_4 with **a** element depth profiles at pH 6 and **b** the calculated surface film thickness according to the data

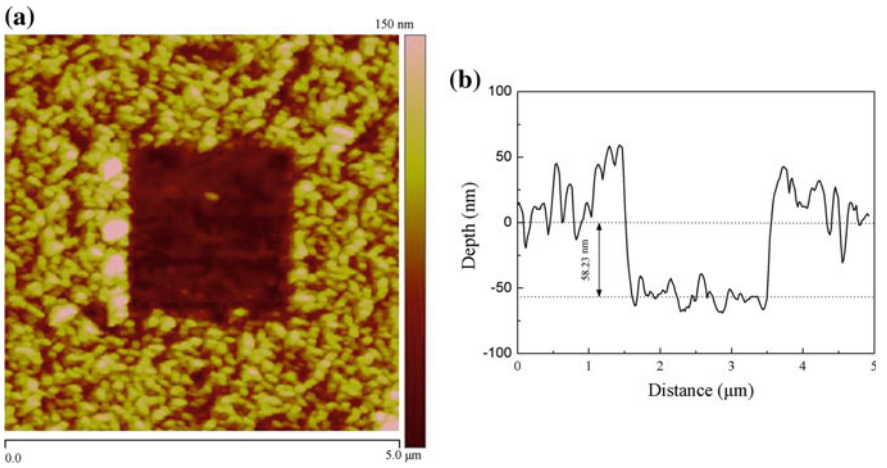

Fig. 2.12 Typical nano-scratch on Cu surface at pH 9 by AFM: **a** 2D image; **b** cross-sectional profile of the scratch trench

(b) the sputtering time T has an accuracy of 0.1 min, and therefore a lower sampling frequency could enlarge the error of thickness calculation.

In order to evaluate the corrosion enhanced mechanical abrasion of Cu in a KIO_4-based slurry, the nano-scratch tests were performed under a 0.126 μN force after immersing the samples into 0.015 M KIO_4 solutions for 5 min. Figure 2.12 shows the typical scratch morphology under a pH-9 condition. There is an obvious pileup around the scratch trench due to the probe pushing the removed material. The average scratch depth is shown in Fig. 2.13. It is apparent that the scratch depth is comparatively low ($\sim$2 nm) for Cu surfaces that were untreated or treated in the pH 11 solution, similar to the results obtained in H_2O_2-based solutions (Li et al. 2013). When the pH values of the solutions are 4, 6 and 9, the scratch depth sharply increases to more than 50 nm, with the maximum (79.29 nm) obtained at pH 6.

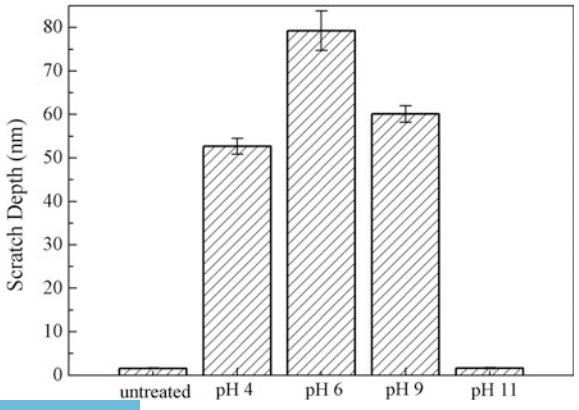

Fig. 2.13 The nano-scratch depth on Cu surface under different pH conditions

These results can be explained by two reasons. First, the surface films produced in the KIO_4-based solutions (at pH values of 4, 6, and 9) are significantly thicker than those under pH 11 and untreated conditions. Second, it is reported that the Cu $(IO_3)_2 \cdot nH_2O$/Cu-periodate formed on a Cu surface is non-uniform and could be easily removed due to its low mechanical strength (Jiang et al. 2014; Mischler et al. 1999; Varadarajan et al. 1997).

2.4 Chemical Corrosion of Cu

To study the chemical effect during CMP, the CMP-electrochemical experiments were conducted. In this chapter, two conditions are mainly investigated. (a) Polishing condition: the real CMP process was imitated (with down pressure of the head and rotational motion of the pad), and the electrochemical signals are measured. (b) Static condition: the static corrosion experiments are carried out (without down pressure of the head nor rotational motion of the pad), and the electrochemical signals are measured. The total MRR attributed to chemical corrosion during CMP (MRR_{cc}) could be calculated by Eq. 2.10:

$$\mathrm{MRR_{cc}} = I_{\mathrm{cc}} \cdot M/(n \cdot \rho \cdot F) \tag{2.10}$$

where I_{cc} is the corrosion current density of Cu under polishing condition, M is the relative atomic mass of Cu (64), n is the valence of Cu (usually n = 2), ρ is the density of Cu (8.9 g/cm^3), and F is the Faraday constant (96,500 c/M).

The corrosion current densities under both the polishing and static conditions could be used to quantitatively evaluate the mechanical abrasion-enhanced chemical corrosion during CMP. K is defined as the ratio of the abrasion-enhanced corrosion to the total chemical effect, and K could be calculated as follows:

$$\mathrm{K} = (I_{cc} - I_c)/I_{cc} \tag{2.11}$$

where I_c refers to the corrosion current density of Cu under static condition. A higher K means a stronger mechanical abrasion-enhanced chemical corrosion during polishing.

2.4.1 Static Etching of Cu

The corrosion current density with and without polishing is shown in Table 2.3. Over the entire pH range (pH 4-11) I_c is lower than I_{cc}. However, I_{cc} and I_c follow the same trend: the current density is at its minimum when pH is near neutral, while it increases as the solution is either more acidic or more alkaline. At pH 4, the current reaches the maximum (∼21 and ∼29 μA for the static and polishing

Table 2.3 The results of the CMP-electrochemical tests

pH	4	6	7	9	10	11
I_{cc} (μA)	29.2388	15.9281	5.4806	6.0502	8.5894	9.4843
I_c (μA)	21.1017	14.7398	3.6118	2.7661	3.5311	6.8139
E_{cc} (V)	0.178	0.106	0.069	0.067	0.086	0.001
E_c (V)	0.100	0.071	0.044	0.000	0.030	−0.02
ΔI_c (μA)	8.1372	1.1883	1.8688	3.2841	5.0584	2.6705
$\Delta I_c/I_{cc}$	0.2783	0.0746	0.3410	0.5428	0.5889	0.2816
ΔE_{corr} (V)	0.078	0.035	0.025	0.067	0.056	0.021

condition, respectively), which is significantly larger than that of other pH conditions.

Cyclic polarization curve could be used to investigate the pitting properties. Figure 2.14 shows the cyclic polarization curve of Cu in KIO_4 solutions. The forward scan and backward scan curves meet in one point, and the corrosion potential of the forward scan is lower than that of the backward scan, both of which indicate that pitting corrosion of Cu has happened in KIO_4 solutions.

In acidic solutions (pH = 4 and 6), when the potential rises to ca. 0.4 V (0.6 V vs. SHE), the corrosion current density dramatically increases. According to the Eh-pH diagram (Fig. 2.6), Cu dissolves in the solution, forming Cu^{2+}. Therefore, in acidic solutions the pitting corrosion of Cu is active dissolution pitting. In alkaline solutions (pH = 9 and 11), when potential is higher than 0.2 V, Cu oxide with passivation effect could stably form on the surface according to the Eh-pH diagram. Within the potential range of 0.2–0.8 V, the corrosion current density decreases a little bit due to passivation, as shown in Fig. 2.14b. However, when the potential is higher than 1.0 V (1.2 V vs. SHE), the anodic current density significantly increases. At this time, the increase of the current is due to the breakdown of passive film, namely the passivity breakdown pitting.

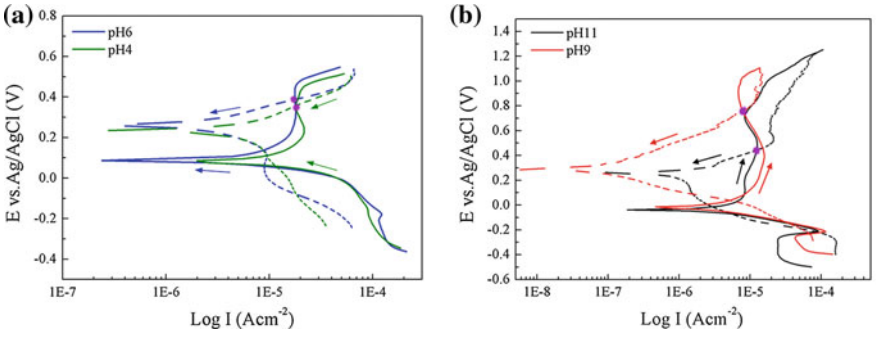

Fig. 2.14 The cyclic polarization curves of Cu in KIO_4 solutions under: **a** acidic conditions; **b** alkaline conditions

E_b is defined as the initial potential of the forward scan when the corrosion current density significantly increases, and E_p is defined as the intersection of the forward and backward scan curves. A higher E_b means better anti-pitting corrosion property. When both E_b and E_p are high, the pits have better self-healing property. Under alkaline conditions, the E_p for pH 9 is higher than that of pH 11, indicating better passivation properties of the Cu surface film. The findings coincide well with the corrosion rate results in Table 2.3, that is, low static corrosion rate is obtained under weak alkaline conditions. E_p is comparatively low for acidic conditions, and the passivation of Cu is not good enough to prevent Cu from active dissolution pitting, resulting in a high corrosion rate.

2.4.2 *Mechanical Abrasion-Enhanced Chemical Corrosion of Cu*

With respect to the abrasion-enhanced corrosion effect, K reaches its maximum when the solutions are weakly alkaline (0.5428 for pH 9 and 0.5889 for pH 10). This trend is plotted in Fig. 2.15. Considering the difference between the real polishing condition and the CMP-electrochemical condition, the K value should be larger. In acidic solutions, static corrosion rate is high but K is comparatively low. This is due to the poor passivation property of the Cu surface film, which will be discussed in detail in Chap. 4.

Figure 2.16 shows the MRR and COF as a function of slurry pH value during CMP. It is interesting to find that the change of MRR is in line with that of K in the CMP-electrochemical experiments, indicating that the mechanical abrasion-enhanced chemical corrosion plays an important role in the MRR. The COF could be affected by various factors during polishing, such as the reaction products, physicochemical properties of the wafer/abrasive interface, and the pad (Liang et al. 2001, 2002). At pH 9, the COF and MRR reach the maximum at the same time.

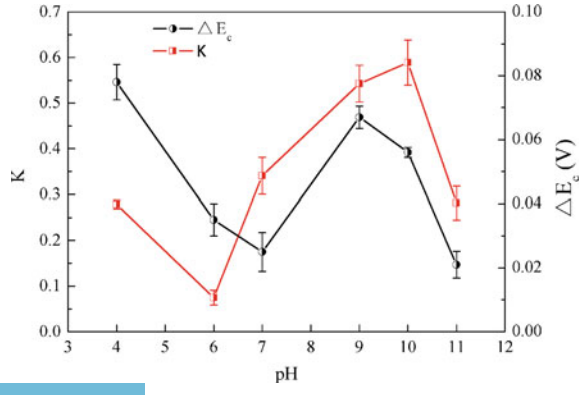

Fig. 2.15 K and ΔE_{corr} during CMP as a function of slurry pH in CMP-electrochemical experiments

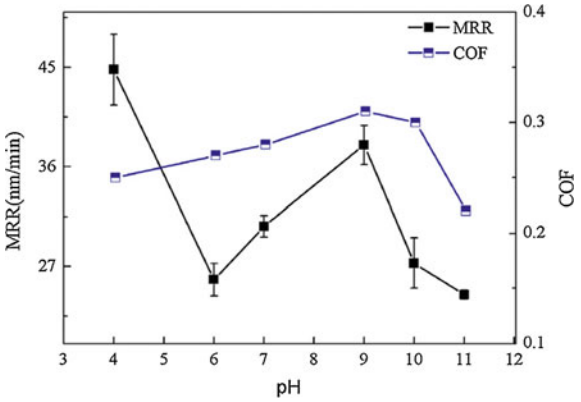

Fig. 2.16 MRR and COF of Cu as a function of slurry pH in CMP experiments

The high COF is probably due to the friction generated during the rapid removal of passive film with low mechanical strength.

The surface topography after polishing is shown in Fig. 2.17. It could be seen that the surface quality of Cu after CMP using slurries containing KIO_4 only is not ideal, and the surface is more or less covered by defects like scratches and pits.

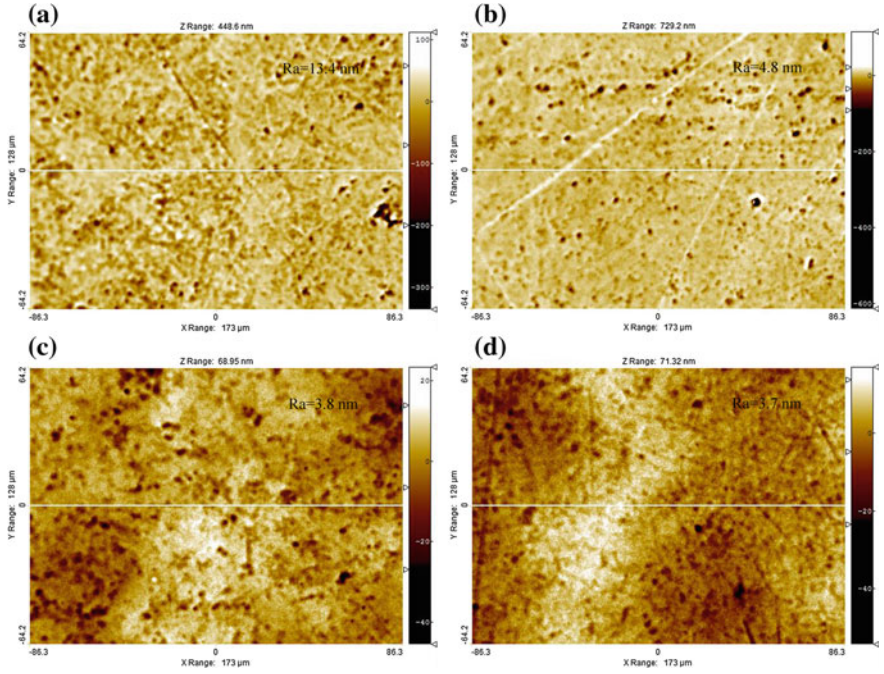

Fig. 2.17 The surface topography of Cu after CMP in KIO_4 slurry: **a** pH 4; **b** pH 6; **c** pH 9; **d** pH 11

To further improve the surface quality after polishing, inhibitors and complexing agents should be added to the slurry, which is not discussed in this chapter.

2.5 Material Removal Mechanism of Cu

According to Eq. 2.10, the MRR resulted from the static corrosion of Cu could be calculated, denoted as MRR_c. MRR due to the pure mechanical force (with no chemical effect) is MRR_w, which could be measured by CMP experiments using slurry without KIO_4. The MRR_c, MRR_w and total MRR at different pH values are shown in Table 2.4. Compared with that with H_2O_2 as oxidant, the surface films formed on Cu in KIO_4-based slurry are complex, and the static corrosion rate of Cu is low (μA scale, normally mA scale in H_2O_2 slurry) (Li et al. 2013). According to Table 2.4, the MRR_c is quite low, which is less than 1 nm/min at different pH values. MRR_w is ca. 5 nm/min, constant at all pH values. Therefore, the sum of MRR_c and MRR_w accounts for a low proportion of the total MRR, which is only about 10% ~ 20%. According to Eq. 2.12, using the slurry containing KIO_4 as oxidant, the chemical-mechanical synergistic effect (ΔMRR) dominates the material removal of Cu during polishing.

$$\mathrm{MRR} = \mathrm{MRR_c} + \mathrm{MRR_w} + \Delta\mathrm{MRR} \tag{2.12}$$

Based on the aforementioned analysis in this chapter, the surface and polishing properties of Cu in KIO_4-based slurry are summarized in Table 2.5. It could be concluded that the material removal mechanism of Cu in KIO_4 largely relies on the chemical-mechanical synergistic effect. However, it differs according to the pH value of the slurry:

- in acidic slurries, the abrasion-enhanced corrosion is comparatively strong, but the corrosion-enhanced abrasion is the weakest;
- in weak acidic slurries, the abrasion-enhanced corrosion is comparatively weak, but the corrosion-enhanced abrasion is comparatively strong;
- in weak alkaline slurries, both the abrasion-enhanced corrosion and the corrosion-enhanced abrasion are comparatively strong;
- in alkaline slurries, both the abrasion-enhanced corrosion and the corrosion-enhanced abrasion are comparatively weak.

Table 2.4 The MRR_c, MRR_w and total MRR of Cu during CMP

	pH 4	pH 6	pH 7	pH 9	pH 10	pH 11
MRR_c (nm/min)	0.65	0.35	0.12	0.12	0.19	0.21
MRR_w (nm/min)	~5					
MRR (nm/min)	44.80	25.79	30.62	37.96	27.29	24.43

Table 2.5 Summary of surface and polishing properties of Cu in KIO_4-based slurry

pH	Acidic	Weak acidic	Weak alkaline	Alkaline
Surface chemistry	Cu_2O $Cu(IO_3)_2 \cdot nH_2O$ Cu-periodate CuI I_2	CuO $Cu(IO_3)_2 \cdot nH_2O$ Cu-periodate CuI	CuO $Cu(IO_3)_2 \cdot nH_2O$ Cu-periodate CuI	Cu_2O
Mechanical properties of surface films	High thickness Micropore High mechanical strength	Moderate porous Low mechanical strength	Moderate porous Low mechanical strength	Low thickness uniform –
Corrosion rate	Highest	High	Lowest	Low
Passivation	Weak	Weak	Strongest	Strong
Corrosion-enhanced abrasion	Weak	Strong	Strongest	–
Abrasion-enhanced corrosion	Strongest	Weakest	Strong	Weak
MRR of CMP	Highest	Low	High	Low
Surface quality after CMP	Bad	Comparatively bad	Better	Better

As for the real polishing process, a high MRR and ideal surface quality could be obtained when abrasion-enhanced corrosion and corrosion-enhanced abrasion are balanced and play a major part of the total MRR. Therefore, the weak alkaline slurries are the ideal polishing slurry during the P3 stage of Cu CMP.

2.6 Conclusions

The chapter presents a study of material removal mechanism of Cu in KIO_4-based slurries from perspectives of surface chemistry and mechanics, chemical-mechanical synergism and CMP experiments. The following conclusions have been drawn:

(1) In acidic slurries, the main composition of Cu surface films is Cu_2O/Cu $(IO_3)_2 \cdot nH_2O$/Cu-periodate/CuI/I_2, the mechanical strength and thickness of which are comparatively high, thus not easy to be mechanically removed; in near neutral slurries, Cu is oxidized to CuO/$Cu(IO_3)_2 \cdot nH_2O$/Cu-periodate/CuI, and the film is mechanically weak, which could be easily removed by abrasion; in alkaline slurries, the Cu surface is only covered with thin and uniform Cu_2O.

(2) The lowest corrosion rate of Cu is obtained in weak alkaline slurries, indicating a better passivation property. Pitting of Cu could happen in KIO_4-based slurries. The pH value of slurries plays a significant role in the formation of pitting, that is, passivity breakdown pitting and active dissolution pitting in alkaline and acidic slurries, respectively.
(3) The chemical-mechanical synergistic effect plays the dominant role in the material removal mechanism of Cu. When both the corrosion-enhanced abrasion and abrasion-enhanced corrosion are significant, a high polishing rate and good surface quality could be obtained. Therefore, weak alkaline slurry is the most suitable for the CMP of Cu.

References

Anik M (2005) Selection of an oxidant for copper chemical mechanical polishing: copper-iodate system. J Appl Electrochem 35(1):1–7

Antonijevic MM, Petrovic MB (2008) Copper corrosion inhibitors: a review. Int J Electrochem Sci 3(1):1–28

Berry GM, Bravo BG, Bothwell ME, Cali GJ, Harris JE, Mebrahtu T, Michelhaugh SL, Rodriguez JF, Soriaga MP (1989) Spectroscopic and electrochemical studies of iodine coordinated to noble-metal electrode surfaces. Langmuir 5(3):707–713

Brusic V, Frisch MA, Eldridge BN, Novak FP, Kaufman FB, Rush BM, Frankel GS (1991) Copper corrosion with and without inhibitors. J Electrochem Soc 138(8):2253–2259

Cano E, López MF, Simancas J, Bastidas JM (2001) X-ray photoelectron spectroscopy study on the chemical composition of copper tarnish products formed at low humidities. J Electrochem Soc 148(1):E26–E30

Carley AF, Coughlin M, Davies PR, Morgan DJ, Wyn Roberts M (2004) Chemisorption and reaction of phenyl iodide at Cu (110) surfaces: a combined STM and XPS study. Surf Sci 555(1):L138–L142

Chen J, Bull SJ (2009) On the factors affecting the critical indenter penetration for measurement of coating hardness. Vacuum 83(6):911–920

Cheng J, Wang T, Chai Z, Lu X (2015) Tribocorrosion study of copper during chemical mechanical polishing in potassium periodate-based slurry. Tribol Lett 58(1):1–11

Deshpande S, Kuiry SC, Klimov M, Obeng Y, Seal S (2004) Chemical mechanical planarization of copper: role of oxidants and inhibitors. J Electrochem Soc 151(11):G788–G794

Du T, Luo Y, Desai V (2004a) The combinatorial effect of complexing agent and inhibitor on chemical-mechanical planarization of copper. Microelectron Eng 71(1):90–97

Du T, Tamboli D, Luo Y, Desai V (2004b) Electrochemical characterization of copper chemical mechanical planarization in KIO_3 slurry. Appl Surf Sci 229(1):167–174

Gaarenstroom SW, Winograd N (1977) Initial and final state effects in the ESCA spectra of cadmium and silver oxides. J Chem Phys 67(8):3500–3506

Hernandez J, Wrschka P, Oehrlein GS (2001) Surface chemistry studies of copper chemical mechanical planarization. J Electrochem Soc 148(7):G389–G397

Jiang L, He Y, Niu X, Li Y, Luo J (2014) Synergetic effect of benzotriazole and non-ionic surfactant on copper chemical mechanical polishing in KIO_4-based slurries. Thin Solid Films 558:272–278

Li J, Liu Y, Lu X, Luo J, Dai Y (2013) Material removal mechanism of copper CMP from a chemical-mechanical synergy perspective. Tribol Lett 49(1):11–19

Liang H, Martin J, Lee R (2001) Influence of oxides on friction during Cu CMP. J Electron Mater 30(4):391–395

Liang H, Le Mogne T, Martin J (2002) Interfacial transfer between copper and polyurethane in chemical-mechanical polishing. J Electron Mater 31(8):872–878
Liao C, Guo D, Wen S, Luo J (2012) Effects of chemical additives of CMP slurry on surface mechanical characteristics and material removal of copper. Tribol Lett 45(2):309–317
Lipton Duffin JA, Ivasenko O, Perepichka DF, Rosei F (2009) Synthesis of polyphenylene molecular wires by surface-confined polymerization. Small 5(5):592–597
Luo Q (2000) Copper dissolution behavior in acidic iodate solutions. Langmuir 16(11):5154–5158
McCafferty E (2005) Validation of corrosion rates measured by the Tafel extrapolation method. Corros Sci 47(12):3202–3215
Mischler S, Spiegel A, Landolt D (1999) The role of passive oxide films on the degradation of steel in tribocorrosion systems. Wear 225:1078–1087
Näsänen R (1954) Studies on copper (II) periodates. Acta Chem Scand 8(9):1587–1592
Pourbaix M (1974) Atlas of Electrochemical Equilibria in Aqueous Solutions. National Association of Corrosion Engineers, Houston
Sherwood PM (1976) X-ray photoelectron spectroscopic studies of some iodine compounds. J Chem Soc Faraday Trans 2 Mol Chem Phys 72:1805–1820
Varadarajan TK, Ramakrishna TV, Kalidas C (1997) Ion solvation of some copper (II) salts in water + N-Methyl-2-pyrrolidinone solvent mixtures at 30 °C. J Chem Eng Data 42(3):453–457
Wijekoon W, Lyktey M, Prasad PN, Garvey JF (1994) The nature of copper in thin films of copper iodide grown by laser-assisted molecular beam deposition: comparative ESCA and EDXS studies. J Phys D Appl Phys 27(7):1548
Wu Z, Zhang Z, Liu L (1997) Electrochemical studies of a Cu (II)-Cu (III) couple: Cyclic voltammetry and chronoamperometry in a strong alkaline medium and in the presence of periodate anions. Electrochim Acta 42(17):2719–2723
Zhang DQ, Goun Joo H, Yong Lee K (2009) Investigation of molybdate-benzotriazole surface treatment against copper tarnishing. Surf Interface Anal 41(3):164–169

Chapter 3
Material Removal Mechanism of Ru in KIO_4-Based Slurry

3.1 Experimental

The experimental methods used in this chapter are similar to those in Chap. 2. To further investigate the corrosion properties of Ru, the electrochemical impedance spectroscopy (EIS) experiments were carried out, see Sect. 3.1.2. Micro-region chemistry on Ru surface after the static etch experiments were also analyzed, see Sect. 3.1.3.

3.1.1 Sample Preparations

The Ru blanket wafer (SKW Associates, Inc.) was used for the static etch experiments. The stack structure is Si/SiO_2 (500 nm)/Ta (25 nm)/Ru (200 nm). To observe the cross-sectional structure of the Ru blanket wafer, the focused ion beam (FIB) cutting technique was used to prepare the sample, and the process is shown in Fig. 3.1. After the FIB cutting process, the sample was observed by scanning electron microscopy (SEM), and the results are shown in Fig. 3.2. It could be seen that the Ru thin film made by physical vapor deposition (PVD) is uniform and well prepared, with no diffusion at interfaces. It is clear in Fig. 3.2b that the Ru film has a columnar crystal structure and there exists a 5 nm thin film between Ru and Pt, which is due to the native oxides formed on Ru surface in the air. Figure 3.3 shows the surface topography measured by optical interferometer surface-mapping microscope (MicroXAM, Veeco). The surface roughness Ra is 1.7 (0.1) nm, indicating a good surface quality (Fig. 3.4).

J. Cheng, *Research on Chemical Mechanical Polishing Mechanism of Novel Diffusion Barrier Ru for Cu Interconnect*, Springer Theses,
DOI 10.1007/978-981-10-6165-3_3

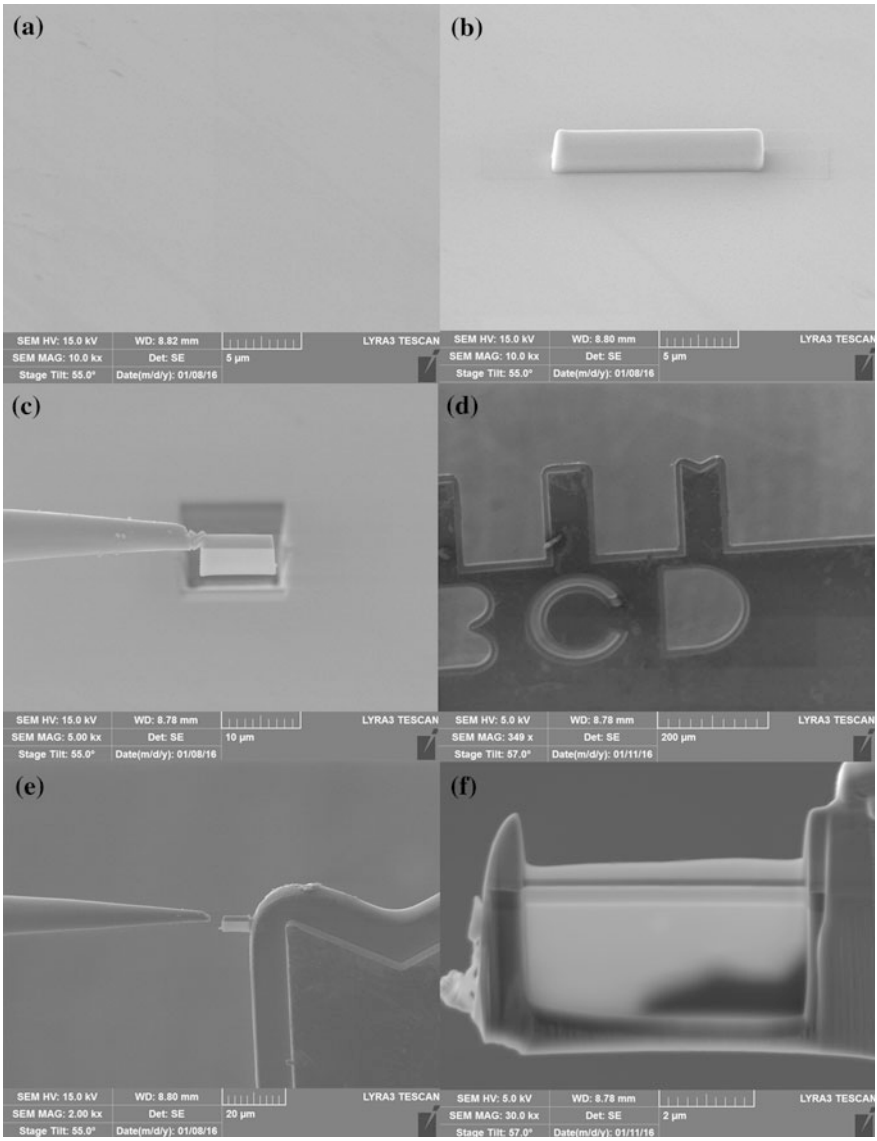

Fig. 3.1 The process of FIB cutting: **a** bulk Ru sample; **b** depositing Pt on the surface; **c** rough cutting and extracting the sample; **d** Cu mesh support; **e** fixing the sample onto the Cu mesh support; **f** thinning of the sample

3.1.2 Electrochemical Measurement

Potentiodynamic polarization and EIS experiments were used to study the steady state chemical properties of Ru such as corrosion and passivation behaviors in

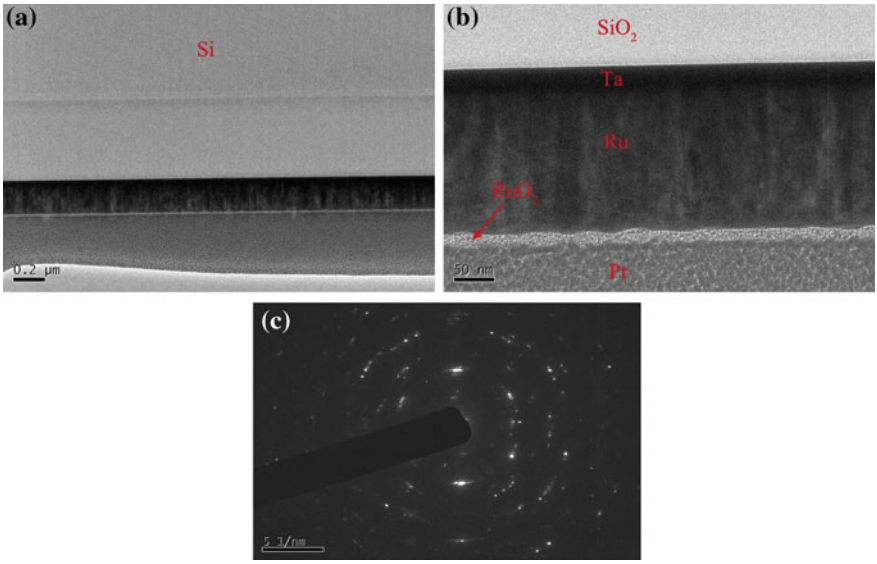

Fig. 3.2 The cross-sectional view of the Ru film: **a** the complete $Si/SiO_2/Ta/Ru$ structure; **b** the local map of (**a**); **c** the diffraction pattern of Ru

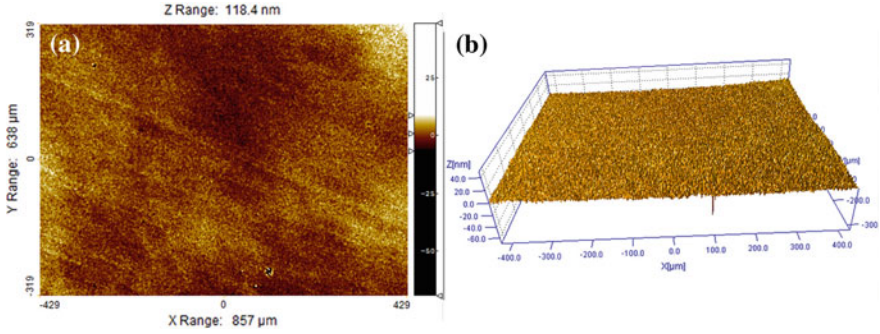

Fig. 3.3 The surface topography of Ru sample: **a** 2D; **b** 3D

KIO_4-based solutions. An Ag/AgCl (3.5 M) electrode and a bright platinum plate acted as the reference electrode and counter electrode, respectively. A sealed Ru, 5 mm in diameter, served as the working electrode. Before each measurement, the Ru was abraded on 2000 # SiC abrasive papers, rinsed with DI water, and dried in N_2 gas. The electrolytes were prepared using DI water with KIO_4 as the oxidant. The pH of the solutions was adjusted to 4, 6, 8, 9, and 11, respectively with H_2SO_4 and KOH as pH adjustors.

The potentiodynamic polarization experiments were conducted using M273A EG&G potentiostat (Princeton Applied Research) with a scan rate of 1 mV/s and a scan range of 1 V (from −0.45 V vs. OCP to 0.55 V vs. OCP). Before each

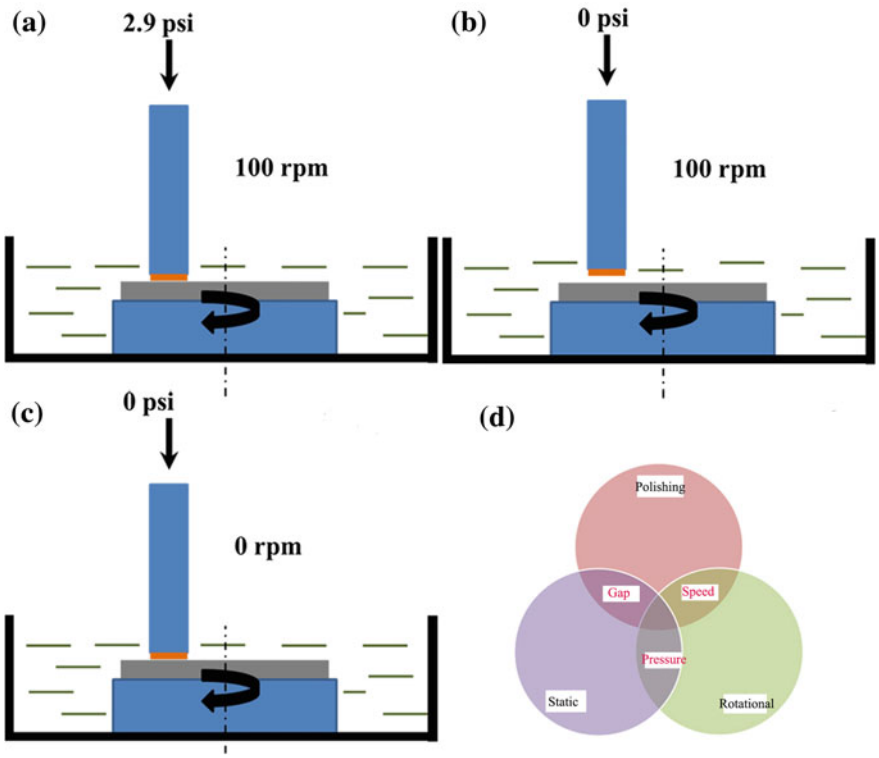

Fig. 3.4 The three different conditions the CMP-electrochemical experiments: **a** polishing condition; **b** rotational condition; **c** static condition. **d** The relationship between the three conditions

scanning, the open circuit potential (OCP) was measured for 600 s. The EIS experiments were carried out using PGSTAT302 N (Metrohm Autolab) at the OCPs. Before each experiment, the OCP was measured until the working electrode reached the equilibrium state ($dE/dt < 10^{-10}$). The applied AC voltage amplitude was 5 mV and the scan frequency range was from 10 MHz to 100 kHz.

3.1.3 Analysis of Surface Chemistry in Micro-Region

After the static etch experiments, the local chemistry should be determined if the surface topography on Ru is not uniform. The confocal Raman spectra were obtained to analyze the chemical products within small areas (2 μm × 2 μm) on the Ru surface. The Raman spectra were measured using a Raman spectrometer (Horiba Jobin–Yvon) with a HeNe laser (632.8 nm). The sampling time is 60 s, and each measurement was repeated for at least 3 times.

3.1.4 CMP-Electrochemical Experiments

Based on the presentation in Chap. 2, the CMP-electrochemical experiments could measure the electrochemical signals under different conditions (static and polishing). In this Chapter, the rotational condition was added to in-depth analyze the abrasion-enhanced corrosion process of Ru during CMP. The relationship and differences among the three conditions are shown below.

Under polishing condition, Ru is polished with a down pressure (2.9 psi) and rotational speed (100 rpm), and the Ru sample is in direct contact with the polishing pad. Under rotational condition, the gap between Ru and the pad is ca. 2 mm, and the rotational speed is 100 rpm. Under static condition, Ru is in contact with the pad without rotation nor down pressure. For example, the same between the rotational and the static conditions is the same pressure (0 psi), and that between the polishing and static conditions is the gap distance (0 mm).

3.2 Ru Surface Chemistry Analysis

3.2.1 Thermodynamic Parameters of Electrochemical Reactions

The stable regions of different substances in the Ru-I-H_2O system are shown in the Pourbaix diagram (Fig. 3.5) calculated using Medusa software, which is widely adopted for the calculation of complex chemical reactions (Madden and Scully 2014). The diagram is drawn with Ru as the predominant element in Fig. 3.5a, while with iodine (I) as the predominant element in Fig. 3.5b. The reaction products formed in the Ru-I-H_2O system are similar to those formed in the Ru-H_2O system with no additional Ru-I reaction products (Pourbaix 1974). It can be seen from

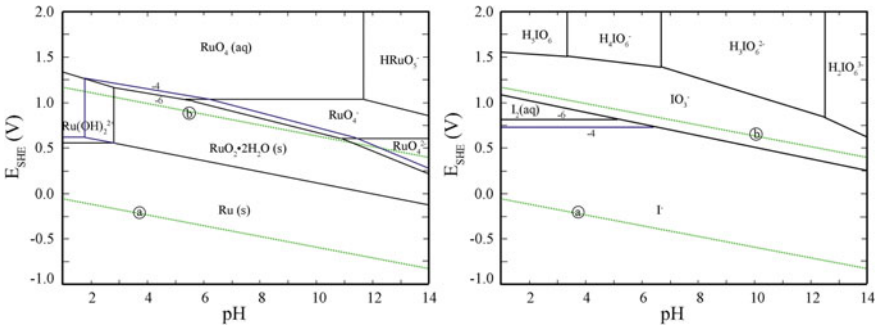

Fig. 3.5 Eh-pH diagram for the Ru-I-H_2O system at 25 °C **a** with Ru as the predominant element **b** with I as the predominant element. $[RuO_4^{2-}]_{TOT} = 10^{-6}$ M, $[I^-]_{TOT} = 10^{-6}$ M for the *black line* and $[RuO_4^{2-}]_{TOT} = 10^{-4}$ M, $[I^-]_{TOT} = 10^{-4}$ M for the *blue line* (color figure online)

Fig. 3.5 that, in the KIO_4-based solution, the electrochemical and chemical reactions on Ru surface vary significantly as a function of the solution pH. The main cathodic reactions are the reduction of IO_4^- and oxygen as follows (Jiang et al. 2014a, b):

$$IO_4^- + H_2O + 2e^- = IO_3^- + 2OH^- \tag{3.1}$$

$$O_2 + 2H_2O + 4e^- = 4OH^- \tag{3.2}$$

The main anodic reactions are shown in Eq. 3.3, which lead to formation of oxides on the surface so that Ru exhibits passivation behavior. $RuO_2 \cdot 2H_2O$ often acts as a passive film on Ru surface, which is stable and protects Ru from fast corrosion. Although the Pourbaix diagram of the Ru-I-H_2O system does not show the existence of RuO_3, it has been reported that RuO_3 exists together with $RuO_2 \cdot 2H_2O$, forming inhomogeneous oxide film on the surface under neutral conditions (Victoria et al. 2010; Cui et al. 2012; Chan et al. 1997).

$$Ru + 4H_2O = RuO_2 \cdot 2H_2O + 4H^+ + 4e^- \tag{3.3}$$

When the electrode potential of Ru increases to higher values, other reactions also may occur, as has been discussed in Sect. 1.2.2. It was reported that RuO_4, with the formation of H_2RuO_5, is very soluble in water (0.13 M, 25 °C) (Kim et al. 2009; Connick and Hurley 1952). Because RuO_4 is believed to be toxic, the formation of RuO_4 should be avoided during the CMP process (Victoria et al. 2011; Zeng et al. 2012; Seddon and Seddon 2013).

3.2.2 *Characterization of Corrosion Products on Ru*

Based on the analyses mentioned above, it could be inferred that the Ru is more likely to be passivated in acidic or neutral solutions while it is chemically dissolved under alkaline conditions. This opinion is supported by Ru surface XPS data obtained after the immersion experiments. The metallic Ru binding energies for 3d5/2 and 3d3/2 are located at 280.5 and 284.7 eV, respectively (Cui et al. 2013; Kim et al. 2009). The Ru binding energies for $RuO_2 \cdot 2H_2O$ are found to be 281.2 and 285.6 eV (Kötz et al. 1983). However, the existence of RuO_3 has been the subject of controversy in many XPS studies (Huang and Pollak 1982; Chan et al. 1997). Because $RuO_2 \cdot 2H_2O$ is a metallic oxide with partially filled conduction band, core-hole coupling may occur on this surface. Therefore, RuO_3 is believed to be present on the bulk-phase $RuO_2 \cdot 2H_2O$ featuring the peaks at 282.1 and 288.2 eV. Figure 3.6 shows the XPS Ru 3d results on the Ru surface immersed into KIO_4 solutions under different pH conditions. It is clear that for the deconvolution of the Ru 3d spectra, there is no obvious difference between the as deposited Ru surface and that immersed in solutions under pH 11. However, when the pH value

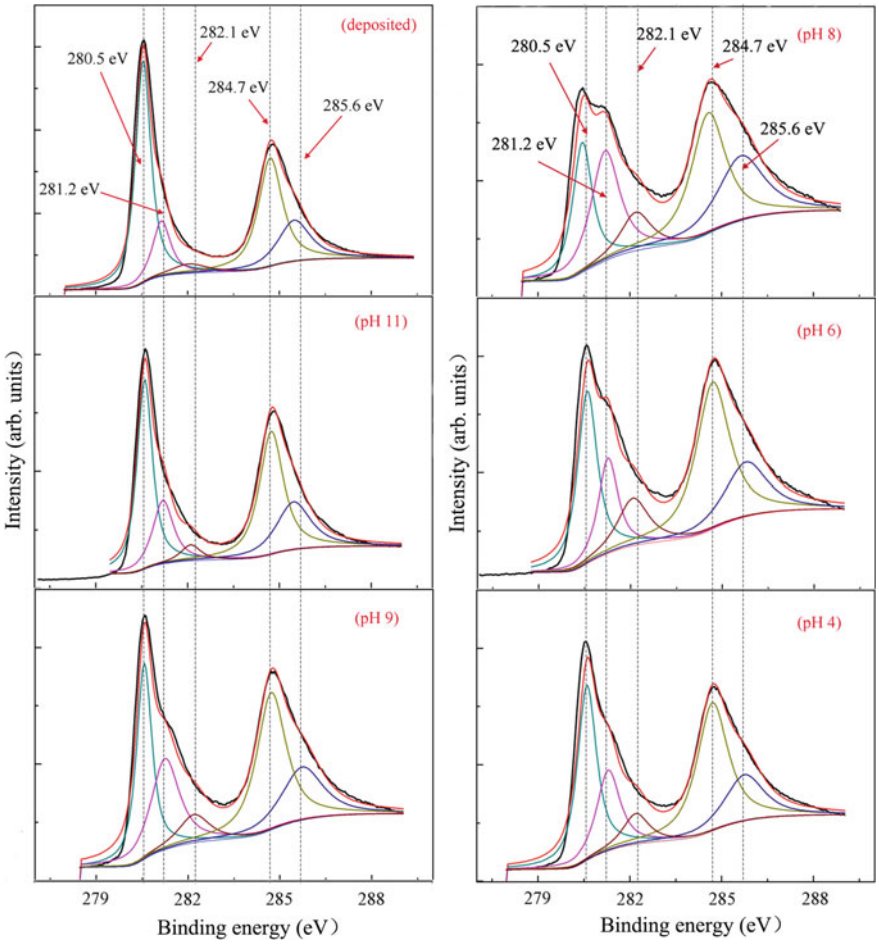

Fig. 3.6 The XPS data of Ru 3d on Ru surface after the immersion experiments in 0.015 M KIO_4 at different pH values

of the solution continues to decrease from 11 to 8, or increase from 4 to 8, the $RuO_2 \cdot 2H_2O$ (281.2 eV) and RuO_3 (282.1 eV) peaks become increasingly obvious, accounting for the asymmetry of the Ru metallic peaks. As is shown in Fig. 3.7, the O: Ru ratio reaches the maximum (2.55) at pH 8, indicating that Ru tends to be oxidized to a higher valence when the solution is near neutral regions. The relative low content of RuO_3 compared with $RuO_2 \cdot 2H_2O$ indicates that RuO_3 is incorporated into $RuO_2 \cdot 2H_2O$ passivation films. The surface is covered with inhomogeneous $RuO_2 \cdot 2H_2O/RuO_3$ layer, as is preferentially formed at neutral pH regions (Lee and Park 2004).

The Ru surface morphology and surface average roughness (Ra) after the immersion experiments are shown in Fig. 3.8. It could be seen that the surface

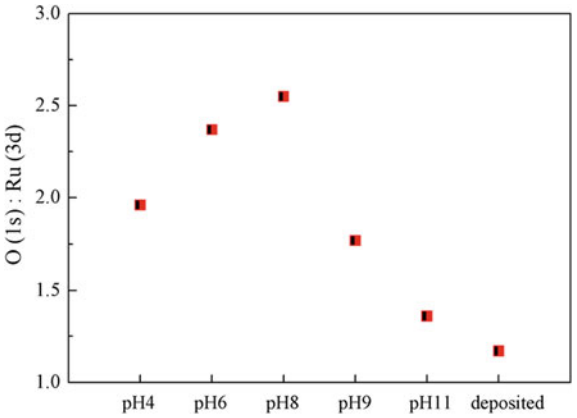

Fig. 3.7 Calculated oxygen to ruthenium (O: Ru) ratio from XPS results in Fig. 3.6

quality of Ru is bad at pH 8, with a Ra value of 35.83 nm. However, the surface quality improves when the solution is more acidic or alkaline. The results agree well with the surface chemistry analysis, proving that the surface passivation films under near neutral conditions are non-uniform. When the scan region expands to larger areas, it is found that the corrosion behaviors of Ru surface under different pH conditions vary greatly. Figure 3.9 shows the SEM image with an area of 8 μm 8 μm. At pH 11, the surface is smooth and uniformly corroded, indicating the mild active dissolution behavior of Ru under alkaline conditions. When the solution is near neutral, the surface is quite non-uniform, corresponding to the rough surface measured in Fig. 3.8. Several microscopic discontinuous structures on Ru surface could be observed, especially at pH 6 in Fig. 3.9d (Liao et al. 2012).

Figure 3.10 is the AFM image of the surface topography within 8 μm × 8 μm area. It could be seen from Fig. 3.10b that the discontinuous structures observed at pH 6 is the protrusion over the surface, with a height of 2–4 nm. Based on the analysis above, the formation of the structure might be due to the formation of RuO_3. To verify the conjecture, confocal Raman spectra were measured between the protrusion and the substrate at pH 6. Figure 3.11 shows the Raman spectra of the Ru surface with corrosion structures at pH 6. The vibration peaks at 515 and 626 cm^{-1} indicate the presence of $RuO_2 \cdot 2H_2O$ (Mar et al. 1995; Huang and Pollak 1982). Areas A and B in Fig. 3.11 refer to the protrusion structure and the substrate area on the Ru surface, respectively. It is clear that compared with the protrusion structure in area A, the area B has apparently formed $RuO_2 \cdot 2H_2O$. The results coincide well with the analysis discussed above. It could be inferred from the Raman spectra results that the micro-protrusion structures on Ru surface at pH 6 are caused by non-uniform corrosion. For lack of sufficient references, the Raman spectra could not be further analyzed. Apart from this, it is difficult to detect useful vibration signals by Raman spectroscopy due to the low content of RuO_3.

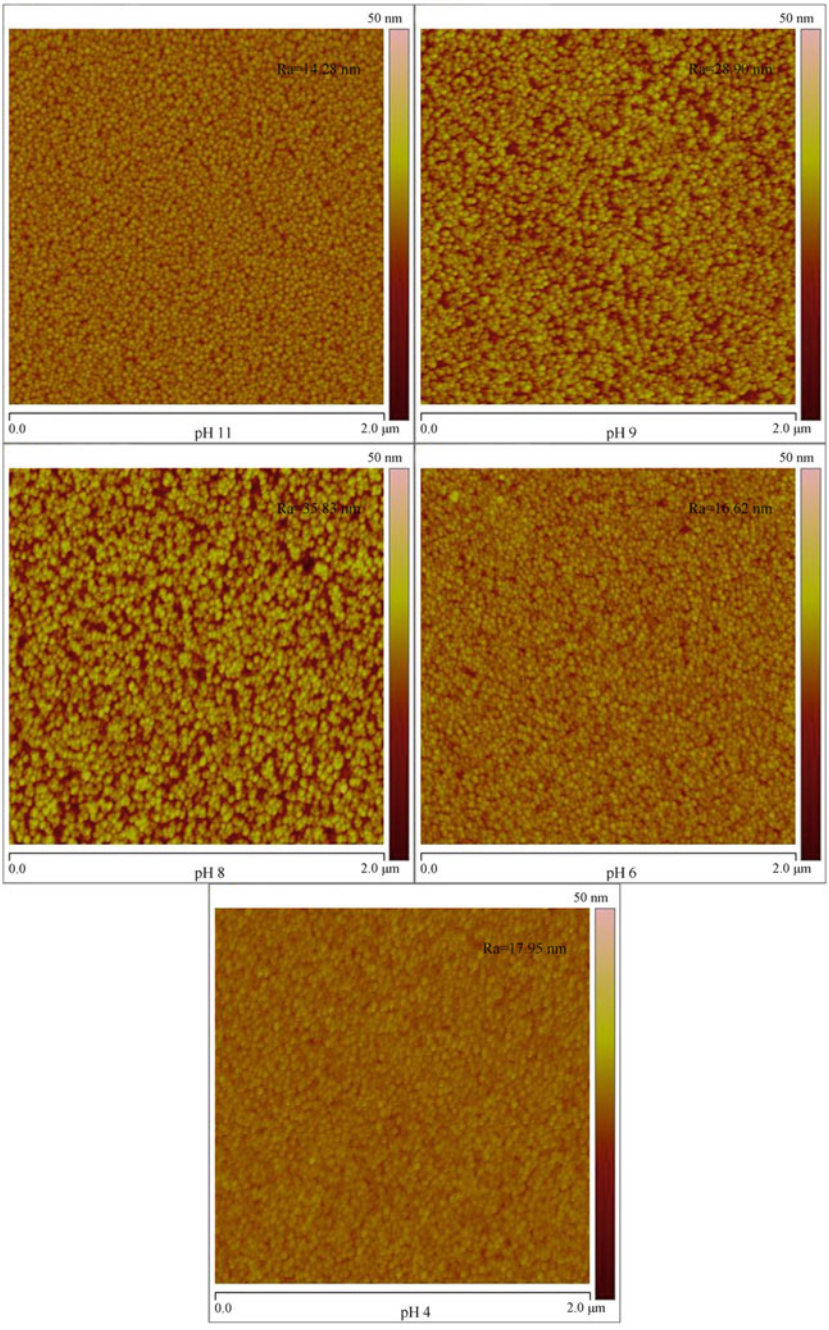

Fig. 3.8 Ru surface morphology and Ra measured by AFM after the immersion experiments in 0.015 M KIO_4

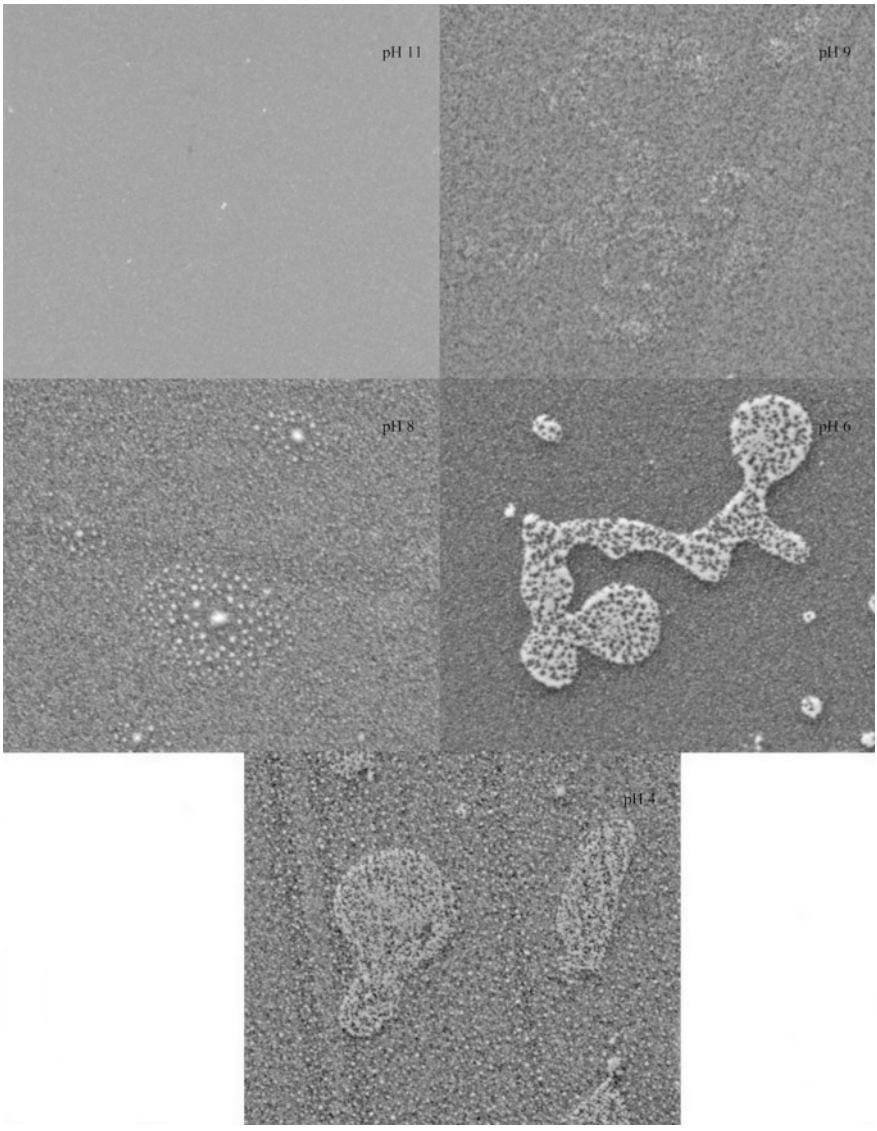

Fig. 3.9 SEM images of the Ru surface within the scan area of 8 μm × 8 μm after the immersion experiments

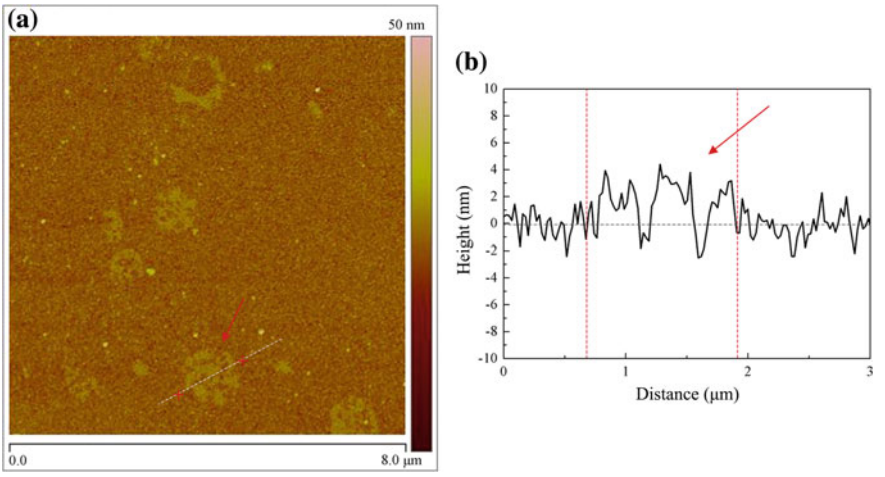

Fig. 3.10 **a** The AFM image of Ru surface under pH 6 within an 8 μm × 8 μm scan area; **b** the cross-sectional profile of the area indicated in **a**

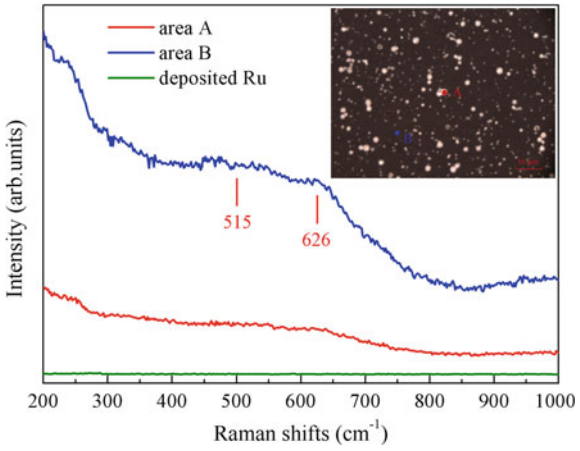

Fig. 3.11 Raman spectra of the corrosion structures on Ru surface at pH 6 and as deposited Ru as comparison

3.3 Thickness of the Passive Film on Ru Surface

In order to characterize the passive film thickness on Ru surface in KIO_4-based solutions, a semi-quantitative analysis was done by AES experiments. Figure 3.12a shows the element depth profiles of the Ru surface under the pH 6 condition. After 20 min, the Ru atomic concentration increases to greater than 90%, and the film thickness is thereby estimated to be about 80 nm (Zhang et al. 2009). Figure 3.12b shows the calculated surface film thickness as a function of solution pH values. It is evident that the surface film thickness reaches the maximum when the solution is

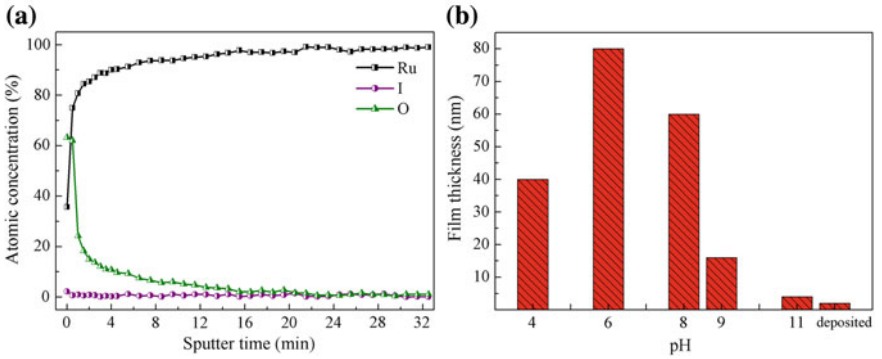

Fig. 3.12 **a** The AES results of element depth profiles on the Ru surface after the immersion experiment at pH 6; **b** the calculated Ru surface film thickness based on the AES results

near neutral (more than 50 nm), whereas the surface is no more passivated when the solution is alkaline (only 4 nm). The results are in line with the SEM results in Fig. 3.9. In alkaline solutions, Ru is under active dissolution and dissolves in solutions in the form of RuO_4^-. In acidic solutions, Ru is oxidized to $RuO_2 \cdot 2H_2O$, which is insoluble and covers on the Ru surface.

3.4 The Corrosion Properties of Ru

3.4.1 Passivation Properties of Ru

The electrochemical measurements were repeated at least three times and the data show a good reproducibility of the results. Figure 3.13 compares typical potentiodynamic polarization curves obtained in the solution with different pH values. At

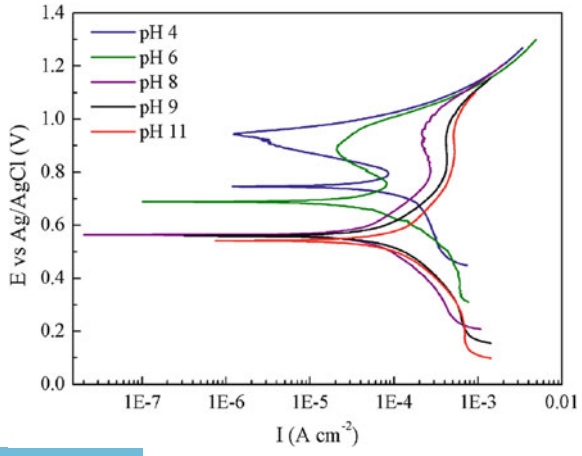

Fig. 3.13 Potentiodynamic polarization curves of Ru in 0.015 M KIO_4 solutions as a function of solution pH

pH 4 and 6, the anodic part of the polarization curves exhibits a S shape, with an active-passive transition around 0.8 V versus Ag/AgCl, and the current density decreases sharply to the magnitude of 10^{-5} A/cm^2 at pH 6 and 10^{-6} A/cm^2 at pH 4, respectively. These results indicate the formation of a passive oxide film on the Ru electrode, i.e., $RuO_2 \cdot 2H_2O$ according to the Pourbaix diagram (Fig. 3.5). The passivation effect is more pronounced at pH 4 than pH 6, probably because of the formation of a more homogeneous $RuO_2 \cdot 2H_2O$ passive film. However, when the solution pH is in alkaline range (8–11), no active-passive transition peak could be observed in the polarization curves. When the potential increases from 0.75 V to higher, the current density remains to be quite stable up to ca. 1.0 V, but it is at the magnitude of 10^{-3} A/cm^2, which is too high to be regarded as passive condition. It is probably that the stable current density is due to a diffusion-limited electrochemical reaction (anodic dissolution) taking place on the electrode, which is in agreement with the EIS results (will be shown in Sect. 3.4.2). When the potential further increases above 1.0 V, the current density starts to increase again independent of the solution pH. The formation of soluble species may occur at high potential, as mentioned above. Moreover, it is likely that oxygen evolution reaction also takes place on the electrode at high potentials and contributes to the increased current density, since Ru and Ru oxides are well known catalysts for such reaction (Alonso-Vante et al. 1995; Chang and Wen 1997).

The corrosion current density (I_{corr}) was obtained by curve fitting using the Levenburg-Marquardt model at around 100 mV near the corrosion potential (E_{corr}). Note that the passivation behavior at lower pH values may give large errors in the fitting results. The I_{corr} and E_{corr} obtained at different pH values are listed in Table 3.1. The E_{corr} steadily increases when the solution pH changes from alkaline to acidic. According to the Evans diagram, E_{corr} is the mixed potential, which is determined by the intersection of the anodic reaction curves and the cathodic reaction curves. The rise of the E_{corr} could be attributed to the increase of the Ru/Ru^{2+} equilibrium potential when the pH of the solution changes to more acidic, as is illustrated in Fig. 3.14. The I_{corr} is the lowest when the solution is near neutral (pH 6 and 8), and increases to a certain extent when the solution is more acidic or alkaline. The reason for this could be the formation of the heterogeneous passive film composed of $RuO_2 \cdot 2H_2O/RuO_3$ in near neutral solutions. $RuO_2 \cdot 2H_2O$ is a metallic oxide with partially filled conduction band, core-hole coupling may occur on its surface, and it has been proved to have a superb electron-proton conductivity than other Ru oxides (Dmowski et al. 2002; Norlin et al. 2005; Bhaskar et al. 2001).

Table 3.1 E_{corr} and I_{corr} determined from Fig. 3.13 in 0.015 M KIO_4 solutions

pH	4	6	8	9	11
E_{corr} (V) versus Ag/AgCl	0.747 ± 0.015	0.688 ± 0.022	0.564 ± 0.005	0.560 ± 0.003	0.542 ± 0.015
I_{corr} (10^{-5} A/cm^2)	14.1 ± 0.38	5.56 ± 0.27	4.76 ± 0.21	8.05 ± 0.16	8.42 ± 0.16

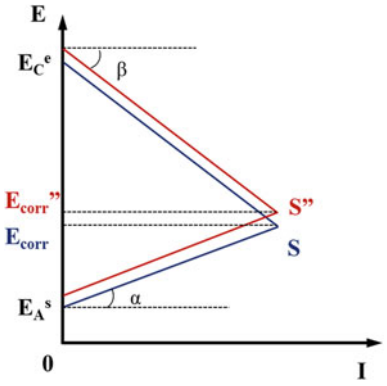

Fig. 3.14 Corrosion polarization diagram

It is reported that some impurities may change the defect structure and thereby reduce the conductivity of RuO_2 (Atanasoska et al. 1990; Hawk and Gadepally 1991). In our case, RuO_3 can be formed on the bulk-phase $RuO_2 \cdot 2H_2O$, and may also have the same effect as the impurities, thus reducing the conductivity of the surface passive film. Besides, a lower I_{corr} is obtained under near neutral conditions compared with that under acidic conditions, where only $RuO_2 \cdot 2H_2O$ is present in the passive film. As has been discussed in AES experiments, at pH 11 the surface film formed on Ru is much thinner than that formed at lower pH, indicating that Ru does not exhibit considerable passivity under this condition, which could explain the higher I_{corr} than near neutral conditions. This explanation is supported by the EIS experiments in the following section.

The potentiodynamic polarization curves of Ru with different KIO_4 concentrations at fixed pH value (pH 9) are shown in Fig. 3.15. In Fig. 3.15a, it can be seen that with the KIO_4 concentration going up, the diffusion-limited mass transfer effect

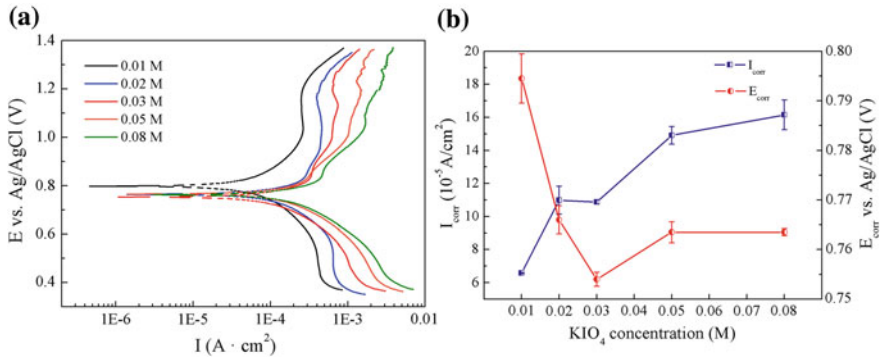

Fig. 3.15 **a** Potentiodynamic polarization curves of Ru in 0.010 M KIO_4 solutions as a function of KIO_4 concentration; **b** the calculated I_{corr} and E_{corr} from (a)

becomes more obvious, which could be observed on the anodic branch. The plateau zone, where the current stops increasing or increases slowly, expands with the elevated KIO_4 concentration. This could be ascribed to the thickening of the surface film with the increased slurry oxidability, thus causing resistance to the reactants and products transportation process. When the KIO_4 content increases, the corrosion current continuously goes up, indicating that the corrosion rate of Ru is improved, as indicated in Fig. 3.15b. Actually no significant difference could be observed for E_{corr}, because the variation range of the Y axis for E_{corr} is as narrow as 0.05 V.

3.4.2 *The Corrosion Kinetics of Ru*

Typical EIS spectra obtained for Ru immersed in the KIO_4 solutions are shown in Fig. 3.16, in both Nyquist and Bode plots. The EIS results were analyzed by spectra fitting using simple equivalent circuits commonly used for metal corrosion purposes. It is obvious that the pH of the solution has a strong influence on the

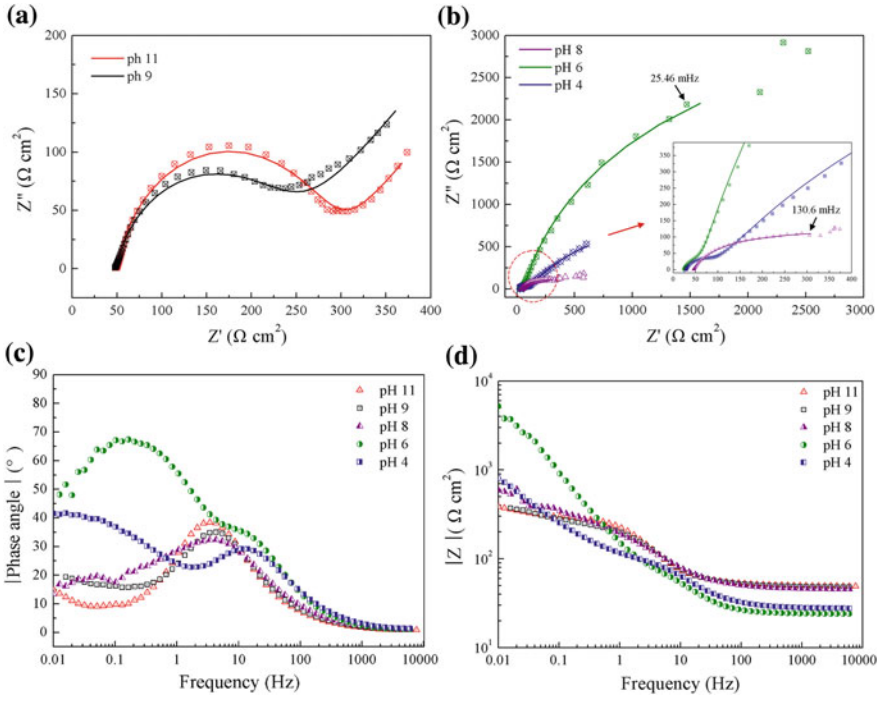

Fig. 3.16 EIS data for Ru in 0.015 M KIO_4 solutions: **a** Nyquist diagram at pH 11 and 9; **b** Nyquist diagram at pH 8, 6, and 4; **c** phase diagram of Bode plots; (d) modulus diagram of Bode plots

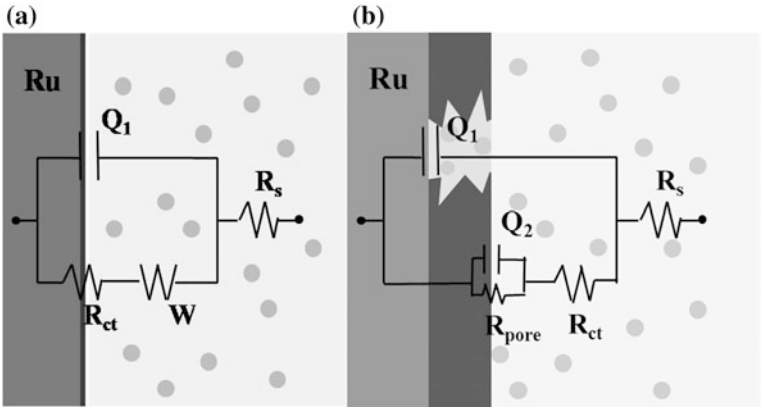

Fig. 3.17 Equivalent circuits of the impedance spectra obtained for Ru in 0.015 M KIO_4

electrochemical behavior of Ru in the KIO_4 solutions. The Nyquist plots of the spectra obtained at pH 9 and 11 (Fig. 3.16a) show one semi-circle capacitive loop at high frequencies and a near 45° linear tail at low frequencies, and only one phase-angle peak appears in the Bode plots (Fig. 3.16c). This is in accordance with the results in Fig. 3.12b, i.e., only a very thin oxide film forms on the Ru surface at these pH values. In this case, the EIS spectra can be fitted by using the equivalent circuit (a) in Fig. 3.17. In this circuit, R_s refers to the solution resistance, the Warburg impedance (W) represents a diffusion-limited mass transfer, indicating a uniform corrosion process on the Ru surface (Chen et al. 2002). The high frequency loop is attributed to the impedance response of the charge-transfer resistance R_{ct} and the double layer capacitance Q_1 (Barik et al. 2005). Here, a constant phase element (CPE) is used instead of a pure capacitor to take account of the deviation from the ideal dielectric behavior, such as the surface heterogeneities. Its impedance function can be expressed as:

$$Z_{CPE} = [Q(j\omega)^n]^{-1} \tag{3.4}$$

where ω is the angular frequency, j is the imaginary number, Q is the admittance constant and n is a constant power ($-1 \leq n \leq 1$) (Mcdonald 1987; Bommersbach et al. 2005). In general, Z_{CPE} could be taken for an inductance ($n = -1$), resistance ($n = 0$), Warburg impedance ($n = 0.5$), and ideal capacitance ($n = 1$), respectively (Cui et al. 2012). A smaller value of n implies a more heterogeneous electrode surface (Morad and El-Dean 2006; Hussin and Kassim 2011; Ma et al. 2003).

In the case of the near neutral and acidic conditions, the EIS spectra exhibit different features, see Fig. 3.16b. A close look reveals that the Nyquist plots consist of two capacitive loops, and two phase-angle peaks appear in the Bode plots (Fig. 3.16c). The two capacitive loops are probably caused by the thick heterogeneous oxide ($RuO_2 \cdot 2H_2O/RuO_3$) film, as discussed above. In these cases, the

impedance modulus at low frequencies is much higher than that under alkaline conditions, as can be seen in Fig. 3.16d. The polarization resistance, a measure of corrosion resistance, is mainly determined by the impedance modulus at low frequencies. In this case, the resistance of the oxide film dominates the impedance response at low frequencies. Meanwhile, the Warburg impedance is not observed, implying that the mass transport in the bulk solution has a minor influence on the corrosion process (de Assis et al. 2006). The EIS spectra of Ru under acidic and neutral conditions can be fitted by using the equivalent circuit (b) in Fig. 3.17. In this circuit, Q_1, R_{ct}, and R_s have the same physical meaning as the elements in Fig. 3.17a. Q_2 represents non-ideal capacitance for the interface between the surface passive film and the solution, and R_{pore} is the pore resistance of the passive film (Díaz et al. 2011). For the Nyquist plot obtained at pH 8, the two capacitive loops seem to overlap, which makes the spectrum fitting quite uncertain. Moreover, there are some scattered data points at low frequencies in the Nyquist plots for pH 8 and 6, which might be caused by the unstable system, e.g., due to local dissolution since the passive films formed under neutral conditions are not uniform, or local detachment of the surface film resulted from condensation of ion vacancies as the passive film becomes thicker (Pan et al. 1996).

The values of the circuit elements obtained from the spectra fitting are given in Table 3.2. The fitted values at pH 8 is not explained here for better analytical accuracy. In acidic solutions, the value of R_{pore} is significantly large, and the polarization resistance is dominated by the resistance of passive film. R_{ct} is smaller than that in alkaline solutions, indicating a smoother charge-transfer process. Based on the calculated parameters listed in Table 3.2, the corrosion rate of Ru in alkaline solutions are controlled by both the diffusion and charge-transfer process, that is, a mixed-controlled process. However for the near neutral and acidic solutions, the rate-determining process of Ru corrosion is the high corrosion resistance of passive film, i.e., a low rate of Ru ion release and oxide growth (Diomidis et al. 2010).

Table 3.2 EIS fitting parameters using the equivalent circuits shown in Fig. 3.17

pH	R_s $\Omega\ cm^2$	Q_1 $\Omega^{-1}\ cm^{-2}\ s^n$	n_1	R_{pore} $\Omega\ cm^2$	R_{ct} $\Omega\ cm^2$	Q_2 $\Omega^{-1}\ cm^{-2}\ s^n$	n_2	W $\Omega^{-1}\ cm^{-2}\ s^{0.5}$
4	27.8	6.46×10^{-03}	0.64	2552.0 (33.6)	78.9 (6.5)	5.61×10^{-4}	0.82	
6	24.0	9.96×10^{-4}	0.89	6453.0 (165.2)	87.8 (8.9)	5.76×10^{-4}	0.86	
8	45.4	6.74×10^{-3}	0.68	237.6 (6.6)	240.2 (5.8)	9.74×10^{-4}	0.73	
9	48.9	6.59×10^{-4}	0.84		191.8 (3.2)			1.72×10^{-2}
11	50.3	5.92×10^{-4}	0.88		235.3 (8.4)			3.28×10^{-2}

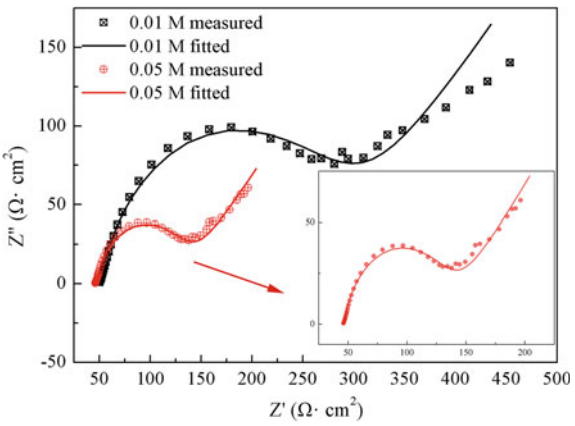

Fig. 3.18 Nyquist plots of Ru in 0.01 M and 0.05 M KIO_4 solutions at pH 9

The EIS results with different KIO_4 concentrations (0.01 M and 0.05 M) are shown in Nyquist plots in Fig. 3.18, fitted by the Z_{view} software. Both the Nyquist plots have one semi-circle capacitive loop at high frequencies and a near 45° linear-like tail at low frequencies. The slope of the linear-like tail is more or less deviated from 45°, and this could be due to the following two reasons: the electrode surface is rough; there exists another state-variable, which could cause inductance during the EIS measurement. Therefore, the EIS Nyquist plots could be fitted by the equivalent circuit with one time constant and a Warburg impedance, as is shown in Fig. 3.17a. This equivalent circuit is widely adopted for metal or alloy with mild and uniform corrosion process, and each element in it has a strong physical meaning (Chen et al. 2002). The high frequency semi-circle loop is concerned with the charge-transfer resistance R_{ct} and the double layer capacitance Q_1, while the Warburg impedance W implies the diffusion-limited mass transfer process. The fitted values of the elements in the circuit are shown in Table 3.3. It is obvious that the corrosion of Ru is a mixed-controlled process. When the KIO_4 concentration increases from 0.01 M to 0.05 M, the R_{ct} distinctively decreases from 236 to 89 $\Omega\ cm^2$ while the W increases from $\sim 0.02\ \Omega^{-1}\ cm^{-2}\ s^{0.5}$ to $\sim 0.04\ \Omega^{-1}\ cm^{-2}\ s^{0.5}$. The decreased R_{ct} value implies a quicker charge transfer process of the redox reactions, while the increased Warburg impedance indicates that the corrosion of Ru is becoming a more diffusion-controlled mass transfer process because of the thickened surface film. The analysis coincides well with the potentiodynamic polarization data in Fig. 3.15.

Table 3.3 EIS fitting parameters of Fig. 3.18 using the equivalent circuit in Fig. 3.17(a)

KIO_4 Con. (M)	R_s ($\Omega\ cm^2$)	Q_1 ($\Omega^{-1}\ cm^{-2}\ s^n$)	n_1	R_{ct} ($\Omega\ cm^2$)	W ($\Omega^{-1}\ cm^{-2}\ s^{0.5}$)
0.01	50.49	6.779×10^{-4}	0.83	236.30 (7.41)	0.0178
0.05	46.41	1.044×10^{-3}	0.85	89.08 (4.63)	0.0393

3.5 The CMP Mechanism of Ru

The CMP-electrochemical experiments could be used to analyze the underlying mechanism of the mechanical abrasion-enhanced chemical corrosion during CMP. The corrosion current density (I_{corr}) of Ru under static, rotational and CMP conditions are shown in Fig. 3.19. Compared with the I_{corr} under static etch condition, the increase of I_{corr} during CMP may result from the following two reasons.

- The mechanical abrasion-enhanced chemical corrosion. The nature of the process is the conversion from mechanical energy to chemical energy. During CMP, the surface film of Ru is removed by mechanical force, and bare Ru surface is exposed to the slurry. As a result, the corrosion reaction equilibrium positively shifts. In addition, the surface layer stress might be enhanced by the mechanical force, generating stress corrosion.
- The convection of slurry during CMP. During CMP, the rotational movement of the pad and the wafer will result in strong convection of the slurry. In most cases, the mass transfer within the liquid layer near the electrode is influenced by both the convection and the diffusion, i.e., the convective-diffusion. The convection of the slurry will influence the mass transfer, and then affects the electrode reaction current density I, which could be calculated by Eq. 3.5.

$$I = n \cdot F \cdot D \cdot (c^o - c^s)/\sigma_{effective} \tag{3.5}$$

where n is the charge of a unit of an ion, F is the Faraday constant, D is the diffusion coefficient, c^s it the concentration of the ion at the electrode surface, c^o is the concentration of the ion in the bulk solution, and $\sigma_{effective}$ is the effective thickness of the diffusion layer. When the convection of the slurry is enhanced, the $\sigma_{effective}$ is obviously compressed, resulting in an increase of I. During the corrosion process,

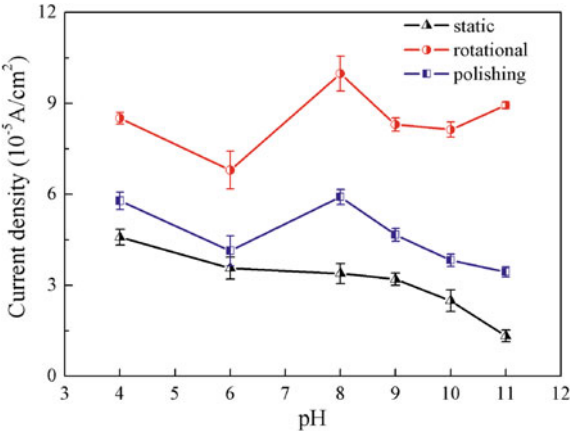

Fig. 3.19 The calculated corrosion current density under three conditions in the CMP-electrochemical experiments

the enlargement of *I* will further give rise to the corrosion current density I_{corr}, and thereby the corrosion rate of Ru will ascend.

As expected, the I_{corr} under static condition is the lowest, and that for the rotational and polishing conditions is obviously larger. However, the I_{corr} under rotational condition is higher than that under polishing condition. This phenomenon could be explained as follows. There exists a gap ($\sim$2 mm) between the pad and the Ru sample under rotational condition while that under polishing condition is 0 mm. For the rotational condition, the convection of the slurry provides good conditions for mass transfer, and thereby enhances the corrosion of Ru. From the results in Fig. 3.19 it is obvious that the mass transfer is more significant than the mechanical abrasion-enhanced chemical corrosion during CMP process.

Comparing the static and rotational conditions, it is obvious that the largest increase of I_{corr} occurs at pH 11, and that at pH 8 takes the second place. From the investigations in Sect. 3.4.2, the corrosion of Ru is partially controlled by diffusion in alkaline solutions, and the rotational movement can bring about the most prominent increase of I_{corr}. Therefore, in alkaline solutions (pH $\geq$ 8), the enhancement of Ru corrosion during CMP is mainly caused by the good fluidity of the slurry. Comparing the polishing and static conditions, I_{corr} significantly goes up under polishing at pH 8. Based on the analysis above, the increase of I_{corr} is due to the combined effect of mechanical-enhanced and the diffusion abrasion-enhanced chemical corrosion of Ru.

Different surface passivation state and topography could significantly affect the Ru CMP process (Jiang et al. 2014a, b; Liang et al. 2001). The passivation (or chemical dissolution) of Ru is almost immediate when Ru is exposed to slurry (Liang and Craven 2005). Therefore, the Ru CMP process is more like an alternant process of surface film formation and removal. When the slurry contains only SiO_2 abrasives, the MRRs are less than 2 nm/min. In addition, no obvious MRR trend with slurry pH can be observed in the Ru CMP. However, when the slurry contains abrasives and oxidant, the MRR significantly differs according to the slurry pH. The MRR at pH 11 is much lower than that of other pH conditions, as is depicted in Fig. 3.20. This is because the surface is slightly passivated, as has been discussed

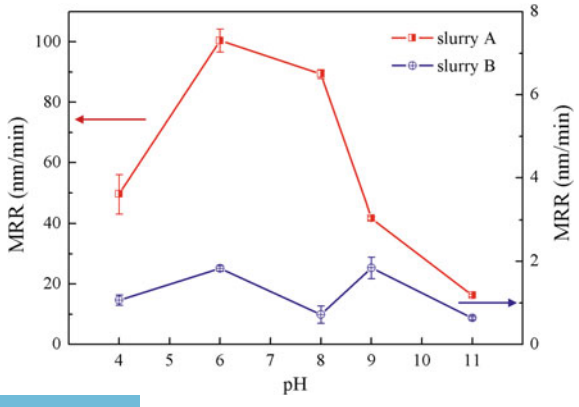

Fig. 3.20 The Ru MRR as a function of slurry pH. Slurry A contains 5% SiO_2 and 0.015 M KIO_4. Slurry B contains 5% SiO_2 only

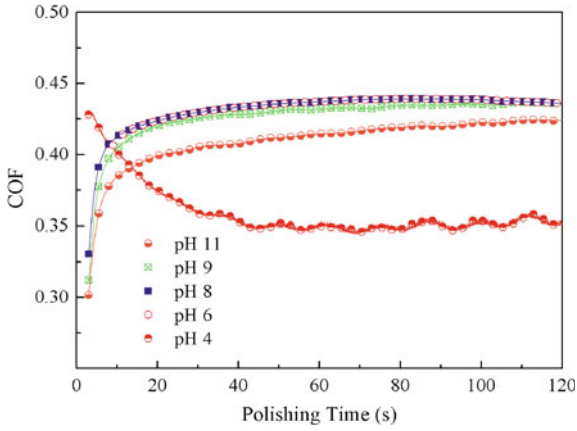

Fig. 3.21 The COF during the Ru CMP process as a function of slurry pH

above. Therefore, the CMP process under this condition is more like a direct abrasion of metallic Ru. In near neutral slurries, the MRRs get to the utmost. The MRR at pH 6 is up to 100.4 nm/min, while it is only 16.3 nm/min at pH 11. At the same time, the OCP in Fig. 3.21 is the highest ($\sim$0.43) under near neutral condition. The comparatively high COF is due to the rough surface as well as the inhomogeneous passivation film structure. The COF at pH 4 is lower than that of pH 11, and this is due to the comparatively low hardness of $RuO_2 \cdot 2H_2O$ passivation films formed on the Ru surface.

The MRRs attributed to pure static corrosion of Ru and the pure mechanical abrasion are quite low (both are less than 2 nm/min, according to Eq. 2.10 and Fig. 3.20). Therefore, the material removal of Ru in KIO_4 slurry is mainly caused by the mechanical-chemical synergistic effect. The MRR in near neutral slurries is over 80 nm/min, which is desirable during CMP. However, when the slurry is more alkaline or acidic, the MRR is low. Based on the analysis above, the abrasion-enhanced corrosion is the strongest when the pH value slurry is 8, while that for pH 6 is not remarkable. The highest MRR at pH 6 indicates a strong corrosion-enhanced mechanical abrasion. In acidic solutions, the static corrosion of Ru is the strongest. The surface and CMP properties of Ru in KIO_4-based slurry are summarized in Table 3.4.

As a consequence, the material removal mechanism of Ru in KIO_4-based slurry is proposed as below. The material removal of Ru is mainly caused by the mechanical-chemical synergistic effect, and the material removal mechanism varies according to the slurry pH values. In near neutral slurries, the passive film formed on Ru is composed of heterogeneous $RuO_2 \cdot 2H_2O/RuO_3$, which is mechanically weak and has a good passivation property. In weak alkaline slurries, the abrasion-enhanced corrosion is stronger, while in weak acidic slurries, the corrosion-enhanced abrasion is predominant.

Table 3.4 Summary of surface and CMP properties of Ru in KIO_4-based slurry

pH	Acidic	Weak acidic	Weak alkaline	Alkaline
Surface chemistry	$RuO_2 \cdot 2H_2O$	$RuO_2 \cdot 2H_2O/RuO_3$	$RuO_2 \cdot 2H_2O/RuO_3$	Ru
Mechanical properties of surface films	Highest thickness High mechanical strength	Highest thickness Low mechanical strength	High thickness Low mechanical strength	Lowest thickness –
Corrosion rate	Highest	Low	Lowest	High
Rate-determining process of corrosion	Resistance of surface film	Resistance of surface film	Resistance of surface film	mixed-controlled
Corrosion-enhanced abrasion	–	Strong	–	–
Mechanical-enhanced corrosion	Weak	Weak	Strong	Strong
MRR of CMP	Low	Highest	High	Low

3.6 Conclusions

This chapter presents investigations of material removal mechanism of Ru in KIO_4-based slurries. Especially, the corrosion and passivation properties of Ru have been thoroughly studied. The main conclusions are as follows:

(1) In near neutral slurries, the surface of Ru is oxidized to heterogeneous $RuO_2 \cdot 2H_2O/RuO_3$, with good passivation properties. In acidic slurries, the composition of surface film is $RuO_2 \cdot 2H_2O$, which is a superb electron-proton conductor. In alkaline slurries, Ru is under active dissolution.
(2) The corrosion of Ru is the lowest in near neutral slurries. In acidic and near neutral slurries, the corrosion process is controlled by the resistance of passivation film. In alkaline slurries, the corrosion process is a mixed-controlled process by both diffusion and charge-transfer.
(3) The chemical-mechanical synergistic effect plays the dominant role in the material removal of Ru during CMP. In near neutral slurries, the surface film of Ru is mechanically weak and easy to be abraded by mechanical force. In weak alkaline slurries, the abrasion-enhanced corrosion is evident while the corrosion-enhanced abrasion plays an important role in weak acidic slurries.
(4) To avoid the formation of toxic RuO_4 and the erosion of dielectric material, the weak alkaline slurries are the most suitable for Ru polishing.

References

Alonso-Vante N, Tributsch H, Solorza-Feria O (1995) Kinetics studies of oxygen reduction in acid medium on novel semiconducting transition metal chalcogenides. Electrochim Acta 40(5): 567–576

Atanasoska L, Atanasoski RT, Pollak FH, O'Grady WE (1990) Single crystal RuO_2/Ti and RuO_2/TiO_2 interface: LEED, auger and XPS study. Surf Sci 230(1):95–112

Barik RC, Wharton JA, Wood R, Stokes KR, Jones RL (2005) Corrosion, erosion and erosion-corrosion performance of plasma electrolytic oxidation (PEO) deposited Al_2O_3 coatings. Surf Coat Technol 199(2):158–167

Bhaskar S, Dobal PS, Majumder SB, Katiyar RS (2001) X-ray photoelectron spectroscopy and micro-Raman analysis of conductive RuO_2 thin films. J Appl Phys 89(5):2987–2992

Bommersbach P, Alemany-Dumont C, Millet J, Normand B (2005) Formation and behaviour study of an environment-friendly corrosion inhibitor by electrochemical methods. Electrochim Acta 51(6):1076–1084

Chan HYH, Takoudis CG, Weaver MJ (1997) High-pressure oxidation of ruthenium as probed by surface-enhanced Raman and X-ray photoelectron spectroscopies. J Catal 172(2):336–345

Chang C, Wen T (1997) Kinetics of oxygen reduction at RuO_2-coated titanium electrode in alkaline solution. J Appl Electrochem 27(3):355–363

Chen W, Wen T, Hu C, Gopalan A (2002) Identification of inductive behavior for polyaniline via electrochemical impedance spectroscopy. Electrochim Acta 47(8):1305–1315

Connick RE, Hurley CR (1952) Chemistry of Ru(VI), -(VII) and -(VIII). Reactions, oxidation potentials and spectra. J Am Chem Soc 74(20):5012–5015

Cui H, Park J, Park J (2012) Study of ruthenium oxides species on ruthenium chemical mechanical planarization using periodate-based slurry. J Electrochem Soc 159(3):H335–H341

Cui H, Park J, Park J (2013) Corrosion inhibitors in sodium periodate slurry for chemical mechanical planarization of ruthenium film. ECS J Solid State Sci and Technol 2(3):P71–P75
de Assis SL, Wolynec S, Costa I (2006) Corrosion characterization of titanium alloys by electrochemical techniques. Electrochim Acta 51(8):1815–1819
Díaz B, Härkönen E, Światowska J, Maurice V, Seyeux A, Marcus P, Ritala M (2011) Low-temperature atomic layer deposition of Al_2O_3 thin coatings for corrosion protection of steel: surface and electrochemical analysis. Corros Sci 53(6):2168–2175
Diomidis N, Celis J, Ponthiaux P, Wenger F (2010) Tribocorrosion of stainless steel in sulfuric acid: identification of corrosion-wear components and effect of contact area. Wear 269(1): 93–103
Dmowski W, Egami T, Swider-Lyons KE, Love CT, Rolison DR (2002) Local atomic structure and conduction mechanism of nanocrystalline hydrous RuO_2 from X-ray scattering. J Phys Chem B 106(49):12677–12683
Hawk RM, Gadepally K (1991) Properties of ruthenium oxide coatings. Proceed Arkansas Acad Sci 45:33–36
Huang YS, Pollak FH (1982) Raman investigation of rutile RuO_2. Solid State Commun 43 (12):921–924
Hussin MH, Kassim MJ (2011) The corrosion inhibition and adsorption behavior of Uncaria gambir extract on mild steel in 1 M HCl. Mater Chem Phys 125(3):461–468
Jiang L, He Y, Niu X, Li Y, Luo J (2014a) Synergetic effect of benzotriazole and non-ionic surfactant on copper chemical mechanical polishing in KIO_4-based slurries. Thin Solid Films 558:272–278
Jiang L, Lan Y, He Y, Li Y, Luo J (2014b) Functions of Trilon® P as a polyamine in copper chemical mechanical polishing. Appl Surf Sci 288:265–274
Kim I, Cho B, Park J, Park J, Park H (2009) Effect of pH in Ru slurry with sodium periodate on Ru CMP. J Electrochem Soc 156(3):H188–H192
Kötz R, Lewerenz HJ, Stucki S (1983) XPS studies of oxygen evolution on Ru and RuO_2 anodes. J Electrochem Soc 130(4):825–829
Lee W, Park H (2004) Development of novel process for Ru CMP using ceric ammonium nitrate (CAN)-containing nitric acid. Appl Surf Sci 228(1):410–417
Liang H, Craven D (2005) Tribology in chemical-mechanical planarization. CRC Press, Boca Raton
Liang H, Martin J, Lee R (2001) Influence of oxides on friction during Cu CMP. J Electron Mater 30(4):391–395
Liao C, Guo D, Wen S, Luo J (2012) Effects of chemical additives of CMP slurry on surface mechanical characteristics and material removal of copper. Tribol Lett 45(2):309–317
Ma H, Chen S, Yin B, Zhao S, Liu X (2003) Impedance spectroscopic study of corrosion inhibition of copper by surfactants in the acidic solutions. Corros Sci 45(5):867–882
Madden SB, Scully JR (2014) Inhibition of AA2024-T351 corrosion using permanganate. J Electrochem Soc 161(3):C162–C175
Mar SY, Chen CS, Huang YS, Tiong KK (1995) Characterization of RuO_2 thin films by Raman spectroscopy. Appl Surf Sci 90(4):497–504
Mcdonald JR (1987) Impedance spectroscopy: emphasizing Solid materials and systems. Wiley, New York
Morad MS, El-Dean AK (2006) 2,2′-Dithiobis(3-cyano-4,6-dimethylpyridine): a new class of acid corrosion inhibitors for mild steel. Corros Sci 48(11):3398–3412
Norlin A, Pan J, Leygraf C (2005) Investigation of electrochemical behavior of stimulation/sensing materials for pacemaker electrode applications II. Conducting oxide electrodes. J ELECTROCHEM SOC 152(7):J85–J92
Pan J, Thierry D, Leygraf C (1996) Electrochemical impedance spectroscopy study of the passive oxide film on titanium for implant application. Electrochim Acta 41(7):1143–1153
Pourbaix M (1974) Atlas of electrochemical equilibria in aqueous solutions. National Association of Corrosion Engineers, Houston
Seddon EA, Seddon KR (2013) The Chemistry of ruthenium. Elsevier, Amsterdam

Victoria SN, Sharma PP II, Suni S Ramanathan (2010) Potassium bromate as an oxidizing agent in a titania-based Ru CMP slurry. Electrochem Solid-State Lett 13(11):H385–H387

Victoria SN, Jebaraj J II, Suni S Ramanathan (2011) Chemical mechanical planarization of ruthenium with oxone as oxidizer. Electrochem Solid-State Lett 15(3):H55–H58

Zeng X, Wang J, Lu H, Chen F, Zhang X, Qu X (2012) Improved removal selectivity of ruthenium and copper by glycine in potassium periodate (KIO_4)-based slurry. J Electrochem Soc 159(11): C525–C529

Zhang DQ, Goun Joo H, Yong Lee K (2009) Investigation of molybdate-benzotriazole surface treatment against copper tarnishing. Surf Interface Anal 41(3):164–169

Chapter 4
Tribocorrosion Investigations of Cu/Ru Interconnect Structure During CMP

4.1 Experimental

The two basic experimental methods in this chapter are the tribocorrosion experiments and the CMP-electrochemical experiments.

4.1.1 Tribocorrosion Experiments

Cu and Ru (99.99% purity), which acted as the lower samples as well as the working electrodes during the experiments, were cut into 20 mm × 20 mm × 2 mm squares. Before the experiments, the samples were polished on a Struers bench top polisher (TegraPol-35) until the surface roughness was below 3 nm. Then the samples were cleaned in DI water and dried in a N_2 gas stream. The upper sample was a Al_2O_3 ball with a diameter of 4.763 mm. The solution contained 0.015 M KIO_4 as oxidant. The pH value was adjusted to 4, 6, 9, and 11 with KOH and H_2SO_4 as pH adjustors. The surface area of the Cu samples exposed to the solution was 1.526 cm^2.

The tribocorrosion experiments were conducted with a universal micro-tribometer (UMT-3, CETR) and a potentiostat (273A EG&G, Princeton Applied Research) in a three electrode electrochemical cell mounted on the tribometer. The reciprocating sliding tribometer is shown in Fig. 4.1. A platinum electrode was used as the counter electrode and an Ag/AgCl (3.5 M) electrode was used as the reference electrode. During the experiments, the Al_2O_3 ball did reciprocating sliding against the Cu surface. The sliding distance was 2 mm, the frequency was 4 Hz, and the applied force was 6 N. Firstly, the open circuit potential (OCP) was measured for 500 s to reach a comparatively stable state for the working electrode. The sliding duration was 100 s and the interval between slidings was 300 s. By this experiment, the following parameters could be measured: (1) the

J. Cheng, *Research on Chemical Mechanical Polishing Mechanism of Novel Diffusion Barrier Ru for Cu Interconnect*, Springer Theses,
DOI 10.1007/978-981-10-6165-3_4

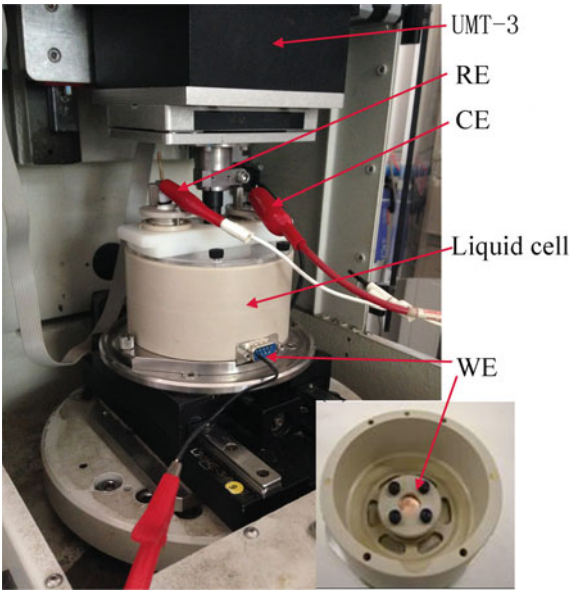

Fig. 4.1 The apparatus for the tribocorrosion experiments

OCP changes under the influence of abrasion; (2) the electrode current changes at the pre-set OCP (constant voltage mode). According to the settings of the potentiostat, the anodic current is negative and the cathodic current is positive. The schematic diagram of the tribocorrosion experiments is shown in Fig. 4.2.

The surface topography of the samples after tribocorrosion tests was observed using a Veeco MicroXAM optical interferometer. The samples were cleaned in DI

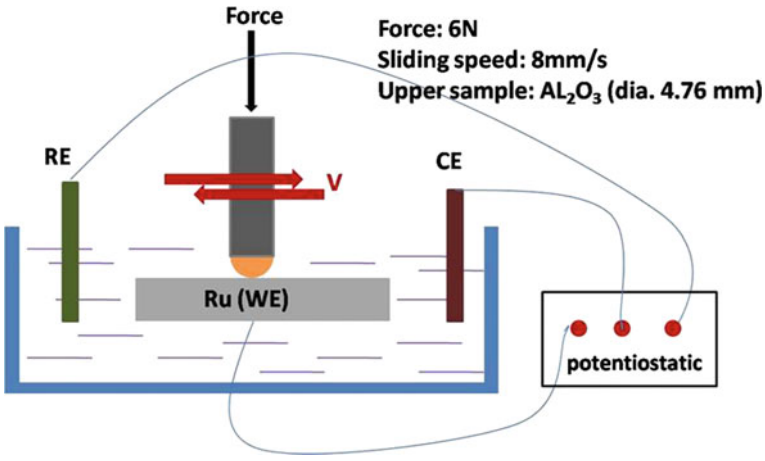

Fig. 4.2 Schematic diagram of the tribocorrosion experiments

water and dried in a N_2 gas stream after the tribocorrosion tests. To characterize the surface chemistry, Raman spectra were used to analyze the chemical reaction products inside and outside the wear tracks. The Raman spectra were measured using a Horiba Jobin–Yvon Raman spectrometer with a HeNe laser (632.8 nm).

4.1.2 The CMP-Electrochemical Experiments

The CMP-electrochemical tests are the same as those stated in Chaps. 2 and 3. The potentiodynamic polarization curves were continuously measured under static, rotational and polishing conditions. By the analysis of the polarization curves and the corrosion current density, the deciding factors to the abrasion-accelerated corrosion of Cu and Ru during CMP were further revealed.

4.2 Tribocorrosion Properties of Cu in KIO_4-Based Solution

4.2.1 Comparison Between the Wear Track and Unworn Surface

Figure 4.3 shows the surface topography of the unworn surface after the experiments. It can be seen that in acidic solutions, the Cu surface undergoes severe corrosion. Obvious pitting corrosion could be seen on the Cu surface at pH 6 and pH 4. The surface roughness (Ra) is listed in Table 4.1. The results correspond well with the surface topography shown in Fig. 2.9. Under acidic conditions, surface

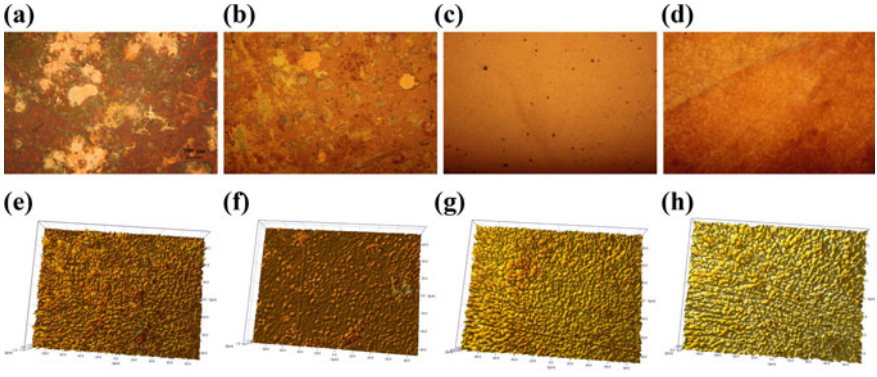

Fig. 4.3 **a**–**d** Optical microscope pictures of the Cu unworn surface (200×) after tribocorrosion experiments; **e**–**h** surface micrographs by white light interferometer; **a** and **e** are at pH 4; **b** and **f** are at pH 6; **c** and **g** are at pH 9; **d** and **h** are at pH 11

Table 4.1 The surface roughness of the unworn Cu as a function of solution pH

pH	4	6	9	11
Ra (nm)	69.5	32.6	12.8	12.9
Standard error (nm)	9.6	7.5	1.6	1.5

roughness is obviously high but it remains comparatively low (about 13 nm) under alkaline conditions.

Cu polishing in KIO_4-based slurry is quite different from that in the H_2O_2-based slurry. Apart from copper oxides and copper hydroxide reported in early literature, the surface passivation film also contains copper iodate and copper periodate, both of which are insoluble in water, as has been stated in Chap. 2. The chemical composition of the unworn Cu surface was analyzed by Raman spectroscopy. More than one kind of copper oxide may exist on the surface, i.e., CuO, Cu_2O and $Cu(OH)_2$. There are often several frequency peaks for a certain material because of the various vibration forms and their overlap. For CuO, the peaks in the Raman spectra are mainly located at the wavenumbers 160, 250, 330, 410 and 635 cm^{-1} (Melendres et al. 1998; Hamilton et al. 1986). The Raman peak associated with the Cu-OH stretch is assigned to $Cu(OH)_2$, which often covers a wide range of wavenumbers between 450–470 cm^{-1} and 540–580 cm^{-1} (Niaura 2000). The most commonly reported peak for the Cu-OH vibration is 488 cm^{-1} (Texier et al. 1998). The peaks located at 220, 588, 633 and 645 cm^{-1} indicate the existence of Cu_2O (Persson and Leygraf 1993; Kliche and Popovic 1990; Biton et al. 2006). The peaks at 124 and 147 cm^{-1} can be assigned to $Cu^+(I^-)OH^-$ complex and the peak at 124 cm^{-1} is assigned to Cu-I vibration in CuI (Irish et al. 1985). The Raman spectra for iodine are located at 180 and 195 cm^{-1} (Deplano et al. 1992; Anderson and Sun 1970). The Raman spectra results may vary little (10 cm^{-1} error) due to the preparation of the sample and the experimental conditions.

For $Cu(IO_3)_2$, the reported Raman spectra data are scarce. It has been reported that for the anhydrated copper iodate, the peaks are located at 697, 737 and 797 cm^{-1} in the 550 to 4000 cm^{-1} region. However, for hydrated Cu iodate ($Cu(IO_3) \cdot nH_2O$), the frequency locates at 720, 745 and 767 cm^{-1}, which are obviously different with those of the anhydrated form. In the lower wavenumber region of 35 to 550 cm^{-1}, there exist many peaks with strong vibrations in the absorbance curve (Nassau et al. 1973). With regard to copper periodate, as mentioned previously, complex reaction products are formed in the periodate-based slurry, thus, the Raman spectra are hard to analyze. It is found that for $CuH_4I_2O10 \cdot 6H_2O$ the frequency peaks were located at 620–630, 671 and 704 cm^{-1} (Botova et al. 2004).

The Raman spectra in Fig. 4.4 indicate the obvious existence of I_2, Cu_2O and $CuH_4I_2O_{10}$–$6H_2O$ on Cu surfaces at pH 4 and pH 6. The formation of copper iodate and copper periodate is more likely to occur on the Cu surface in acidic solutions. I_2 could only exist in acidic solutions, while CuI could form within a comparatively wide pH range. To sum up, the chemical composition on the unworn surface of Cu varies greatly according to the pH value of the KIO_4 solutions. The surface passivation film mainly consists of copper oxides, copper hydroxide and copper iodide.

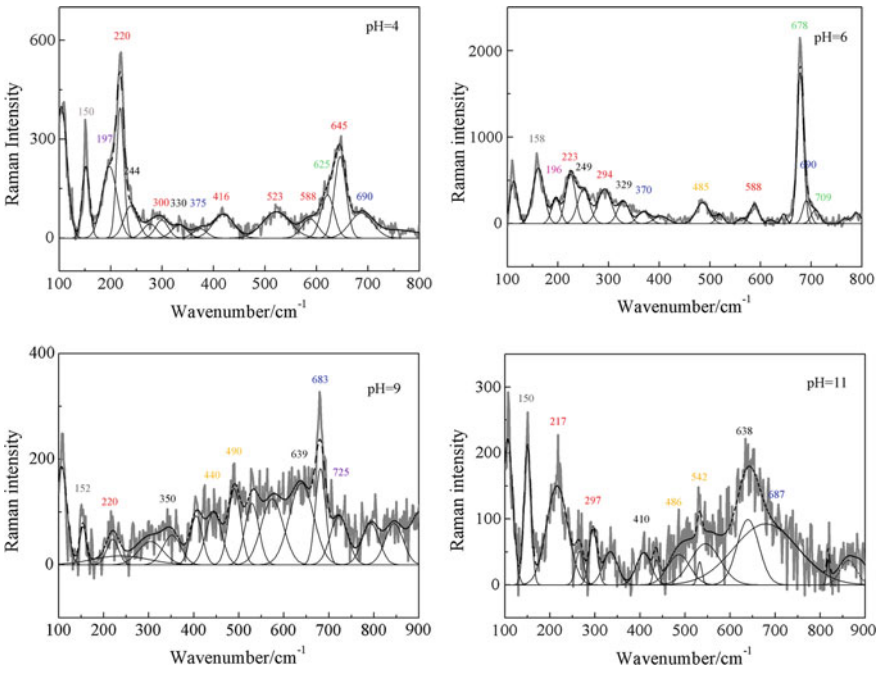

Fig. 4.4 Raman spectra of the unworn Cu surface. The numbers in *red, black, yellow, blue, purple, green, gray* and *pink* color represent Cu_2O, CuO, $Cu(OH)_2$, $Cu(IO_{3)2}$, $Cu(IO_3)_2 \cdot nH_2O$, $CuH_4I_2O_{10} \cdot 6H_2O$, CuI and I_2 peaks, respectively

Copper iodate, copper periodate and iodine can exist under specific pH conditions. The results agree well with the findings in Chap. 2.

Figure 4.5 shows the typical wear track morphology after reciprocating sliding. It can be seen that under acidic conditions, the wear track exhibits a rough surface while it has smooth sidewalls under alkaline conditions (Fig. 4.5b). The wear track

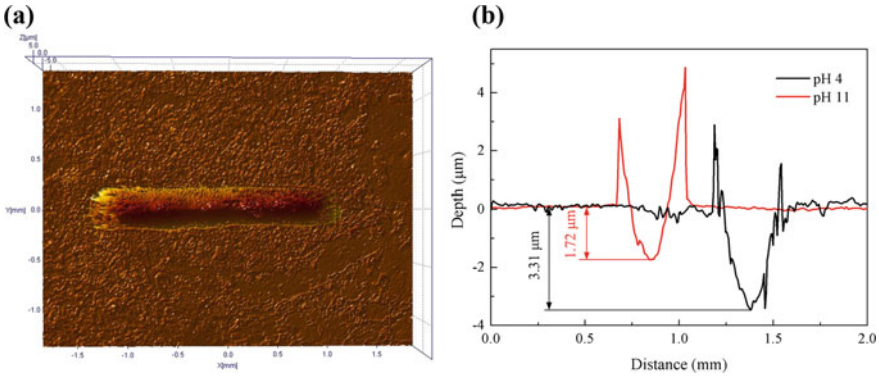

Fig. 4.5 **a** Typical scratch topography of Cu at pH 6; **b** cross sectional view of the scratch in tribocorrosion experiments at pH 4 and 11

Table 4.2 The wear track depth of Cu as a function of solution pH

pH	4	6	9	11
Scratch depth (μm)	3.31	2.70	1.97	1.72
Standard error (μm)	0.20	0.10	0.14	0.22

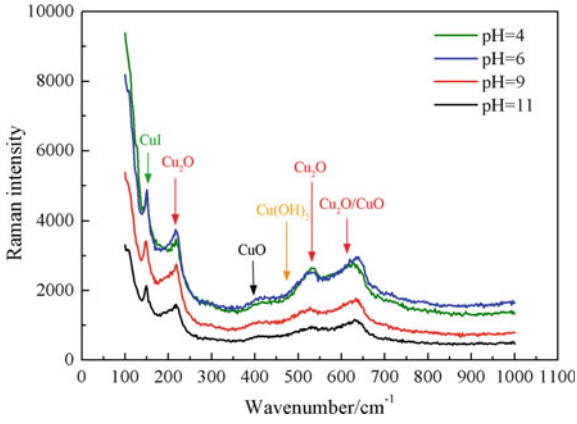

Fig. 4.6 Raman spectra of the wear track on Cu

depth of Cu was extracted from the cross sectional profile, which is shown in Table 4.2. It is obvious that the scratch depth is greatly affected by the pH value and it increases as the solution becomes more acidic.

Figure 4.6 shows the Raman spectra of the wear track in the tribocorrosion experiments. It can be seen that when the pH value decreases, the Raman spectra intensity increases, which indicates a higher content of the reaction products. However, the peak positions for all the pH values are almost the same. The main reaction products on the Cu surface are Cu_2O, CuO, $Cu(OH)_2$ and CuI. Copper periodate, copper iodate and iodine could be barely seen on the rubbed surface. It could be inferred that copper periodate, copper iodate and iodine are mechanically weak, which could be easily removed by abrasion force.

4.2.2 The Electrochemical Signals

The OCP changes of Cu during the tribocorrosion experiments are shown in Fig. 4.7. The arrows in the picture indicate the commencement of rubbing in the reciprocating sliding process. The OCP decreases with an increase of the pH value. Under alkaline conditions, the obvious change of the OCP to lower values is caused by the rubbing process while this trend is unobservable under acid conditions. At the beginning of the rubbing, the OCP sharply jumps to a lower value compared with the initial OCP (pH 9 and 11). However, the OCP evolution during the rubbing

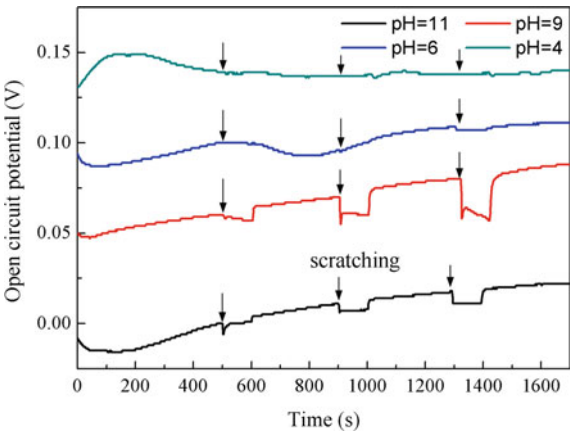

Fig. 4.7 OCP changes of Cu before, during, and after rubbing in KIO_4-based solutions for tribocorrosion experiments

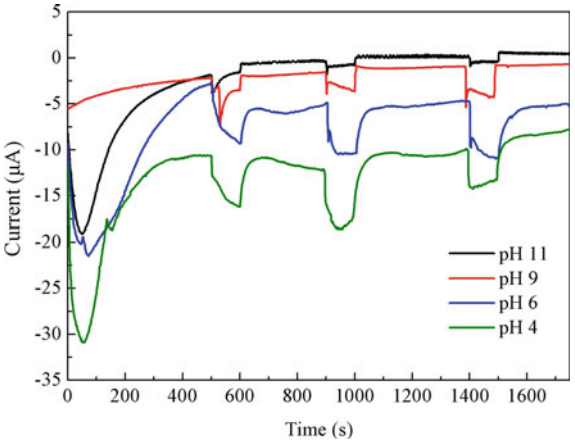

Fig. 4.8 Current changes of Cu before, during, and after rubbing in KIO_4-based solutions for tribocorrosion experiments at the pre-set COFs

process is not the same. At pH 9, the OCP progressively decreases, while for pH 11 it remains almost unchanged at a specific value during the whole rubbing process.

An increase in current during rubbing is observed in Fig. 4.8. The rise in anodic current is evident in both acidic and alkaline solutions. The current jump becomes increasingly larger when the pH value decreases. At the end of the rubbing period, the mechanical abrasion ceases and the current recovers the initial value. It is observed that after each rubbing process, the drop in the current for the acidic solutions is slower and smoother than that of the alkaline solutions. The re-passivation current is defined as the current returning back to the equilibrium state after abrasion. A quicker recover of the re-passivation current often means a better re-passivation property of the metal surface.

The phenomena in Figs. 4.7 and 4.8 could be explained by analyzing the passivation properties of Cu in KIO_4 solutions. A better passivation property will often

result in a remarkable tribocorrosion effect. The following explanations would support this idea.

- The nature of tribocorrosion is the local galvanic corrosion between the fresh metal surface (caused by abrasion) and the unworn surface (often covered by passive film);
- Generally, the unworn surface often has a higher potential, while that of the fresh metal surface is comparatively low. The unworn surface acts as the cathode and the fresh metal surface is the anode. The total corrosion rate is accelerated due to the local galvanic corrosion between the unworn and the fresh metal surface;
- When the passivation of a metal surface is poor, there is no big difference between the de-passivation area and the passivation area, and the potential difference is small. Under this condition, the galvanic corrosion effect is inconspicuous, resulting in a weak tribocorrosion effect and vice versa.

In a galvanic couple, the polarization potential for the cathode is E_c, and the corrosion potential for the cathode before coupling is E_{corr}. A_a and A_c refer to the de-passivation area and the passivation area, respectively, and i_a is the anodic current density of de-passivation area after coupling. Therefore, E_c could be expressed as (Vieira et al. 2012):

$$E_c = E_{corr} + a_c - b_c \log i_a - b_c \log(A_a/A_c) \tag{4.1}$$

where a_c and b_c are constants related to the Tafel plots before coupling. From Eq. 4.1, it could be seen that the decisive factors of OCP (E_c) are the ratio of A_a/A_c and i_a.

Figure 4.9 shows two kinds of the galvanic corrosion during the tribocorrosion experiments (Landolt 2007; Vieira et al. 2012). When the passive film is totally removed within the wear track (Fig. 4.9a), the ratio of A_a/A_c will gradually increase

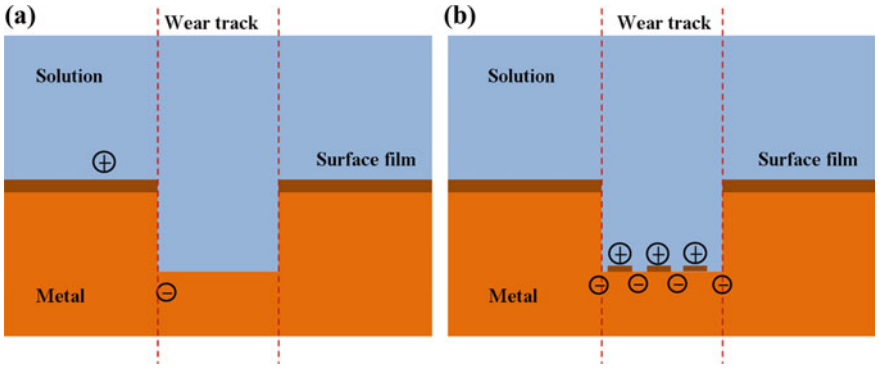

Fig. 4.9 Two kinds of the galvanic corrosion during the tribocorrosion experiments: **a** between the unworn surface and the wear track; **b** within the wear track

with time. Under this condition, E_c will decrease during abrasion, as the OCP curve shown at pH 9. If the galvanic corrosion happens in the form of Fig. 4.9b, E_c will remain almost constant during abrasion (pH 11), because A_a/A_c does not change obviously within the track. As a consequence, it could be concluded that the galvanic corrosion between the wear track and unworn surface dominates at pH 9, whereas the galvanic corrosion within the wear track dominates at pH 11.

Combining the analysis in Chap. 2, a brief summary could be made: The nature of tribocorrosion phenomenon during Cu CMP is that the mechanical abrasion accelerates the anodic reaction rate of the total corrosion process. In acidic KIO_4 solutions, the tribocorrosion phenomenon is not distinct due to the poor passivation properties of the surface film. In alkaline solutions, the passive film formed on Cu has good corrosion inhibition property, and the potentials between de-passivation and passivation areas are huge, which will cause strong galvanic corrosion and finally a prominent tribocorrosion phenomenon. At pH 9, the local galvanic corrosion occurs between the unworn surface and the wear track, while that for pH 11 occurs within the wear track.

4.3 Abrasion-Accelerated Corrosion of Cu During CMP

The typical potentiodynamic polarization curves of Cu under static and polishing conditions in the CMP-electrochemical experiments are shown in Fig. 4.10. When the potential is up to 0.25 V, the corrosion current under static condition (0 rpm) remains stable as the potential continues increasing, indicating that the Cu surface is passivated. However, the current continuously increases under polishing condition (100 rpm), because Cu surface is in active dissolution under the effect of mechanical abrasion during CMP.

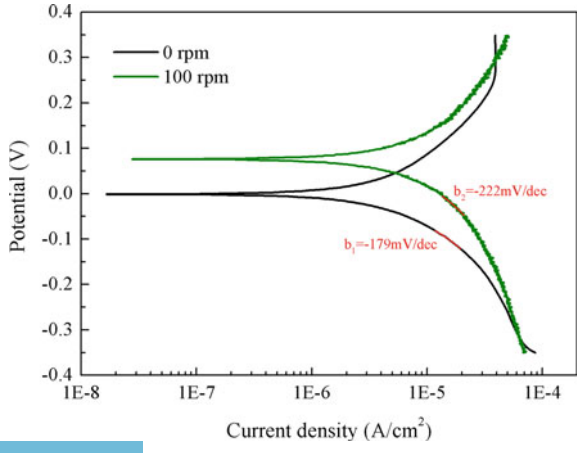

Fig. 4.10 Potentiodynamic polarization curves of Cu under static and polishing conditions at pH 9 in CMP-electrochemical experiments

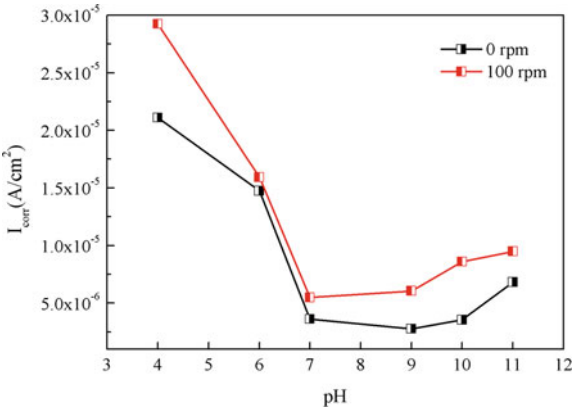

Fig. 4.11 Corrosion current density of Cu under static (0 rpm) and polishing (100 rpm) conditions in CMP-electrochemical experiments

Figure 4.11 calculates the corrosion current density of Cu under the polishing and static conditions, denoted as I_{cc} and I_c, respectively. In Chap. 2, K is defined as the ratio of abrasion-accelerated corrosion/total corrosion, as has been shown in Eq. 2.11. Here K' is defined as the ratio of abrasion-accelerated corrosion/pure corrosion, to represent the strength of abrasion-accelerated corrosion during CMP, and the equation is shown below:

$$K' = (I_{cc} - I_c)/I_c = \Delta I_c/I_c \tag{4.2}$$

From Fig. 4.12, it is interesting that K' has the similar variation trend as K. In weak alkaline solutions, K' reaches the maximum (more than 1.0), indicating that there happens strong abrasion-accelerated corrosion during CMP under this condition. In weak acidic solutions, K' is comparatively low. The results stated above agree with the conclusions drawn from the tribocorrosion experiments. That is, conclusions follow the same rule despite of the different experimental perspectives.

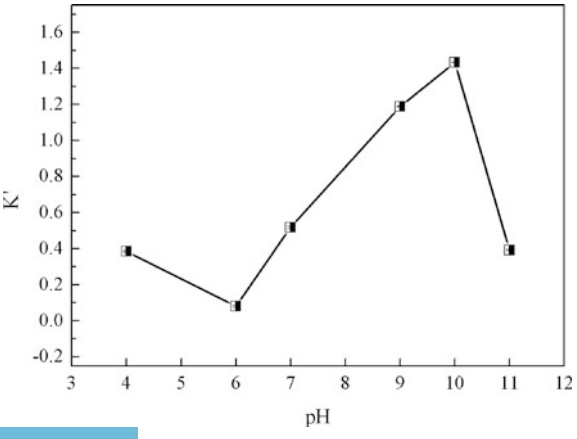

Fig. 4.12 K' of Cu as a function of the KIO_4 solution pH

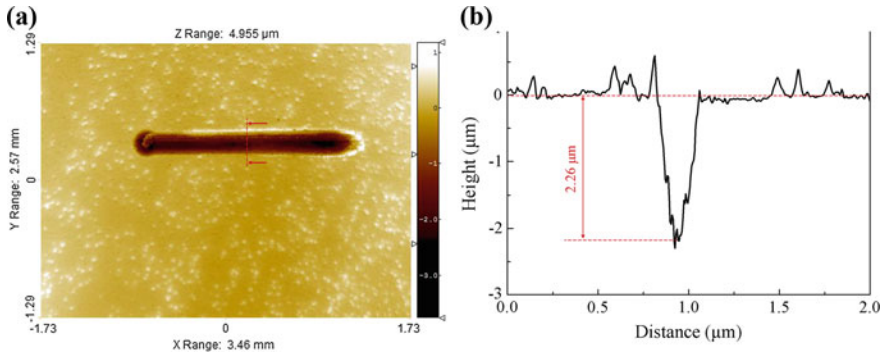

Fig. 4.13 **a** Typical scratch topography on Ru surface at pH 9; **b** the cross-sectional view of the scratch indicated in **a**

4.4 Tribocorrosion Properties of Ru in KIO_4-Based Solution

Figure 4.13 shows the typical wear track topography on Ru after reciprocating sliding in tribocorrosion experiments. The potential holds at the pre-set OCP. The wear track depth under different solution pH is shown in Table 4.3. It is obvious that the scratch depth is affected by the pH value and reaches the maximum of 2.90 μm at pH 6. The scratch depth variation trend coincides with the surface film thickness variation (Sect. 3.3), both of which get the highest value at pH 6 and reach the minimum at pH 11. Therefore, the scratch depth after tribocorrosion experiments could reveal the surface film thickness to some extent.

The results obtained from the tribocorrosion experiments are shown in Figs. 4.14 and 4.15. The sliding process may change the OCP value because of the galvanic coupling established between the depassivated worn area and the surrounding passivated surface. The ratio of the worn area to the whole Ru surface is very small, so that the sliding and repassivation process could be regarded as an accelerated corrosion process under the pre-defined OCP values. Because the cathodic current is positive, the increase or decrease of the current mentioned below refers to the absolute value of the current density. Figure 4.14 shows three complete runs of the scratching process in the KIO_4 solution at pH 11. The variation of the current density with time differs greatly between static condition and the abrasion process. At pH 11, the current density increases almost linearly during abrasion,

Table 4.3 The scratch depth of the wear track on Ru surface in tribocorrosion experiments

pH	4	6	9	11
Scratch depth (μm)	2.15	2.90	2.26	1.88
Standard error (μm)	0.14	0.10	0.21	0.11

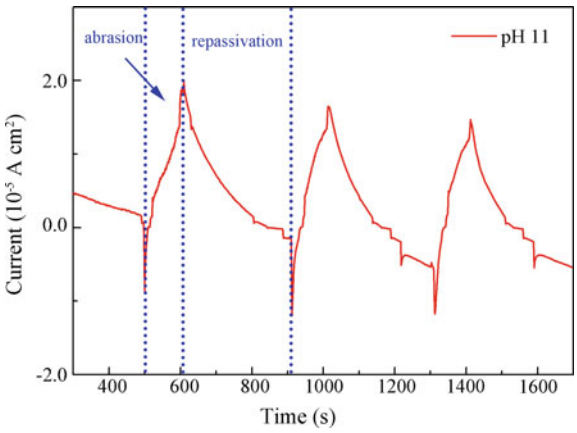

Fig. 4.14 Total three runs of the tribocorrosion experiment at pH 11

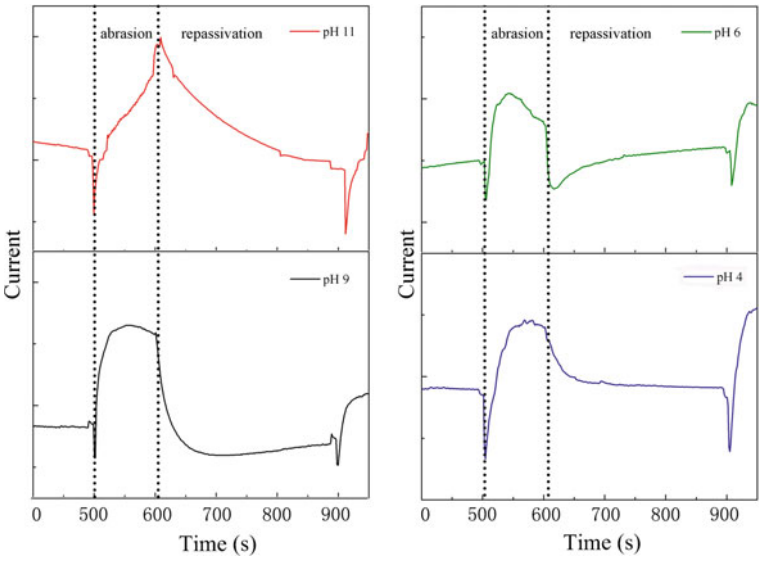

Fig. 4.15 Current changes (the 1st run) with time in tribocorrosion experiments. All the four subgraphs have the same Y axis range (4×10^{-5} A/cm^2)

and then drops steadily right after the stop of the mechanical abrasion because of the formation of a thin oxide film. For a better comparison between different pH conditions, the results from the first run of the whole process are extracted and illustrated in Fig. 4.15. In this figure, the range of the Y (vertical) axis is 5.0×10^{-5} A/cm^2 for all the conditions with different pH values.

At the beginning of the scratching, there is an oscillation of the current, which results from the preloading process of the upper sample. During scratching, there is a sharp increase in the current for all the pH conditions, indicating the abrasion-enhanced corrosion from the depassivated area. The fact that the current increases in positive direction suggests that the enhanced corrosion is caused by the enhancement of the cathodic reactions on the Ru surface. At the predefined-OCP values, the current responding to scratching may come from two origins: the enlargement of the sample surface caused by the wear track and the galvanic coupling between the wear and the surrounding surface (Diomidis et al. 2010). Although it is impossible to distinguish these two effects in the experiment, it is possible to contrast between different pH conditions.

For pH 11, the current increases linearly during scratching, but for pH 4 and 9, it shoots up and remains quite stable during scratching. It is noticeable that at pH 6, the current even begins to drop during the scratching process. The result implies that at pH 6, the surface undergoes a strong repassivation during sliding. For the next 300 s after scratching, the repassivation rate differs significantly between different pH conditions. The current decreases slowly at pH 11 and the fastest current drop occurs at pH 6. These results indicate that the scratched Ru surface repassivates more easily under near neutral condition (pH 6) than other pH conditions, which is in agreement with the results from the AES, EIS and potentiodynamic polarization measurements in Chap. 3.

4.5 Abrasion-Accelerated Corrosion of Ru During CMP

Figure 4.16 shows the *K'* value of Ru, and *K'* has the same meaning as defined in Sect. 4.3. It could be seen that the *K'* basically increases as the solution pH goes up, and reaches a small peak at pH 8 (ca. 0.8). The *K'* reaches the maximum at pH 11,

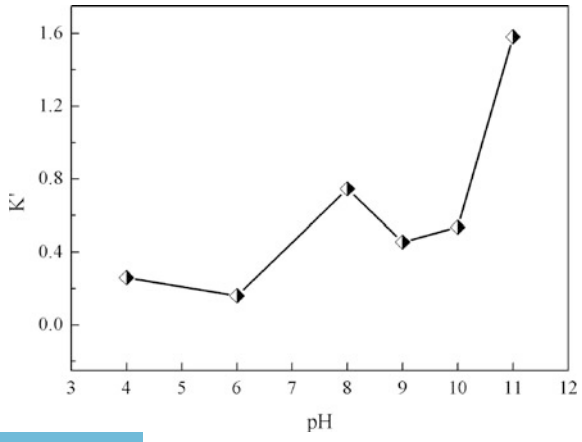

Fig. 4.16 *K'* of Ru as a function of the KIO_4 solution pH

with the value of 1.6. It is clear that the abrasion-accelerated corrosion of Ru is more prominent in alkaline solutions. Based on the analysis stated in Sect. 3.5, the strong abrasion-accelerated corrosion of Ru in alkaline solutions could be explained as follows. Under this condition, the rate-determining process of corrosion is a diffusional-limited mass transfer process, and the rotational movement from CMP could enhance the convection, therefore accelerating the corrosion of Ru. Apart from this, the mechanical strength of surface passive film on Ru is low in weak alkaline solutions, which is easily removed by mechanical abrasion. Eventually, the corrosion of Ru is not only enhanced by the accelerated electrochemical process, but also the abrasion-accelerated corrosion in weak alkaline solutions. Therefore, a small peak appears at pH 8.

However for Cu, which is in direct contact with Ru in the integrated circuits, the tribocorrosion behavior in KIO_4 solution is just the opposite, as has been investigated in Sect. 4.2. The abrasion process mainly accelerates the anodic reactions on the Cu surface. As a result, the mechanical abrasion exerted on the Ru/Cu bimetallic interface during CMP, though has not been directly proved, might aggravate the galvanic corrosion of Cu. This phenomenon has gained much attention (Jiang et al. 2014; Cheng et al. 2014). As a result, there is urgent need to investigate and minimize the galvanic corrosion between Cu and Ru during the barrier layer CMP process.

4.6 Conclusions

In this chapter, CMP-electrochemical experiments combined with the traditional tribocorrosion experiments were carried out to investigate the tribocorrosion properties of Cu and Ru during CMP. Results show that the nature of tribocorrosion phenomenon is the local galvanic corrosion between the abrasion induced depassivation area and the passivation area on metal surface. The external mechanical energy is imported into the system, accelerating the anodic reactions of Cu corrosion and cathodic reactions of Ru corrosion, respectively. The tribocorrosion property is closely related to passivation on metal surfaces. When alkaline slurry is used during CMP, tribocorrosion effect of Cu and Ru is evident, which is caused by both the convection-enhanced corrosion and the mechanical abrasion-enhanced corrosion.

References

Anderson A, Sun TS (1970) Raman spectra of molecular crystals I. Chlorine, bromine, and iodine. Chem Phys Lett 6(6):611–616

Biton M, Salitra G, Aurbach D, Mishkov P, Ilzycer D (2006) On the electrochemical behavior and passivation of copper and brass (Cu70/Zn30) electrodes in concentrated aqueous KOH solutions. J Electrochem Soc 153(12):B555–B565

Botova M, Nagel R, Haeuseler H (2004) Präparation, kristallstruktur, schwingungsspektren und thermische analyse von kupfer-tetrahydrogen-decaoxo-diperiodat-hexahydrat $CuH_4I_2O_{10} \cdot 6H_2O$. Zeitschrift für anorganische und allgemeine Chemie 630(1):179–184

Cheng J, Wang T, Mei H, Zhou W, Lu X (2014) Synergetic effect of potassium molybdate and benzotriazole on the CMP of ruthenium and copper in KIO_4-based slurry. Appl Surf Sci 320 (30):531–537

Deplano P, Devillanova FA, Ferraro JR, Isaia F, Lippolis V, Mercuri ML (1992) On the use of Raman spectroscopy in the characterization of iodine in charge-transfer complexes. Appl Spectrosc 46(11):1625–1629

Diomidis N, Celis J, Ponthiaux P, Wenger F (2010) Tribocorrosion of stainless steel in sulfuric acid: Identification of corrosion-wear components and effect of contact area. Wear 269(1): 93–103

Hamilton JC, Farmer JC, Anderson RJ (1986) In situ Raman spectroscopy of anodic films formed on copper and silver in sodium hydroxide solution. J Electrochem Soc 133(4):739–745

Irish DE, Stolberg L, Shoesmith DW (1985) Surface enhanced Raman spectroscopy and electrochemistry at the copper/iodide, water interface. Surf Sci 158(1):238–253

Jiang L, He Y, Lu X, Luo J (2014) Investigation on the galvanic corrosion of copper during chemical mechanical polishing of ruthenium barrier layer. Paper presented at the International Conference on Planarization/CMP Technology, Kobe

Kliche G, Popovic ZV (1990) Far-infrared spectroscopic investigations on CuO. Phys Rev B 42(16):10060

Landolt D (2007) Corrosion and surface chemistry of metals. CRC Press, Lausanne

Melendres CA, Bowmaker GA, Leger JM, Beden B (1998) In-situ synchrotron far infrared spectroscopy of surface films on a copper electrode in aqueous solutions. J Electroanal Chem 449(1):215–218

Nassau K, Shiever JW, Prescott BE (1973) Transition metal iodates. I. Preparation and characterization of the 3*d* iodates. J Solid State Chem 7(2):186–204

Niaura G (2000) Surface-enhanced Raman spectroscopic observation of two kinds of adsorbed OH^- ions at copper electrode. Electrochim Acta 45(21):3507–3519

Persson D, Leygraf C (1993) In situ infrared reflection absorption spectroscopy for studies of atmospheric corrosion. J Electrochem Soc 140(5):1256–1260

Texier F, Servant L, Bruneel JL, Argoul F (1998) In situ probing of interfacial processes in the electrodeposition of copper by confocal Raman microspectroscopy. J Electroanal Chem 446(1):189–203

Vieira AC, Rocha LA, Papageorgiou N, Mischler S (2012) Mechanical and electrochemical deterioration mechanisms in the tribocorrosion of Al alloys in NaCl and in $NaNO_3$ solutions. Corros Sci 54:26–35

Chapter 5
Micro-galvanic Corrosion of Cu/Ru Couple in KIO_4 Solution

5.1 Experimental

5.1.1 Sample Preparation

The Cu/Ru samples were prepared by mechanically embedding a small Cu electrode into a Ru disk (99.99% purity), so the galvanic couple was created with a tight interface between Cu and Ru. The polished Cu/Ru couple was used for the Volta potential mapping. For the electrochemical and in situ AFM measurements, the Cu/Ru couple was embedded in epoxy in a sample holder, as schematically illustrated in Fig. 5.1. A screw hole at the back side of the sample enabled electrical connection to the instrument. The critical dimensions of the sample are labeled, and the exposed area ratio of Cu: Ru is 1:16. Before each experiment, the sample surface was grinded in water with abrasive papers progressively to 4000 grits, and then polished on flannel pad with ethanol and diamond paste of 1, 0.5, 0.25 μm, which resulted in a smooth surface including the Cu/Ru interface. After polishing, the sample was ultrasonically cleaned in ethanol for 10 min, and dried in compressed N_2 stream. The used sample surface was repolished for repeated measurements. The solution used for the in situ AFM and electrochemical experiments contained 0.015 M KIO_4 (purchased from Sigma-Aldrich Co. LLC.) as oxidant, and the pH was adjusted to 9 by using diluted KOH/H_2SO_4 solutions. This test solution was simplified with respect to the CMP slurries, it was chosen in this study in order to focus on the micro-galvanic corrosion of the Cu/Ru couple in KIO_4-containing electrolyte.

J. Cheng, *Research on Chemical Mechanical Polishing Mechanism of Novel Diffusion Barrier Ru for Cu Interconnect*, Springer Theses,
DOI 10.1007/978-981-10-6165-3_5

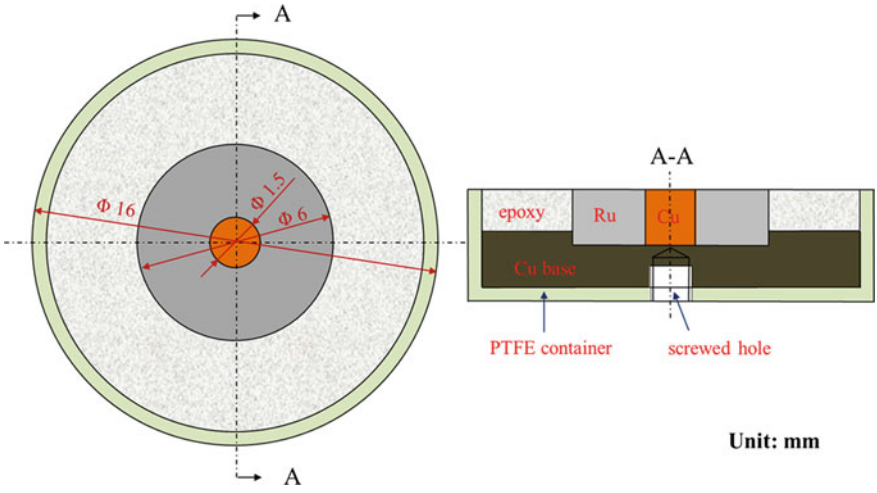

Fig. 5.1 A schematic illustration of the Cu/Ru sample. Only critical dimensions are labeled

5.1.2 Confocal Raman Microscopy Analysis

Chemical composition of the corrosion products formed on the Cu/Ru sample surface was analyzed after the exposure by using a confocal Raman spectrometer (CRM, LabRAM HR800, Horiba Jobin–Yvon). After the in situ AFM experiments, the Cu/Ru sample was taken out from the solution without any drying, the precipitated corrosion products formed around the Cu/Ru interface was immediately analyzed by the CRM. The samples were excited with a HeNe 532 nm green laser, and the lateral resolution of the analysis was less than 1 μm. The data were processed with Labspec 5 software.

5.1.3 KFM Mapping and In-situ AFM Measurements

First to introduce the Kelvin Probe Force Microscopy (KFM) technology. A commercial AFM with Mac III unit (Agilent 5500) was utilized to map Volta potential variation across the Cu/Ru interface in air, and to record topography images in situ in the solution to monitor the topography changes during the exposure. The AFM instrument was placed inside an isolation chamber, where the relative humidity was around 30% and the temperature was in the range of 23–25 °C. The instrument has three lock-in amplifiers, which makes it possible, with one-pass mode, to measure surface topography and Volta potential signals simultaneously. For this purpose, conductive SCM-PIT probes (purchased from Bruker Corp.) were used, and the Volta potential was recorded at an operating frequency of 10 kHz,

which was far away from the resonance frequency (60–100 kHz) for the topography signal. In this way signal cross-talk can be avoided.

For the in situ AFM experiments in the solution, a liquid cell from Agilent designed for electrochemical measurements was used, and the sample was immersed in the solution during the measurements. Contact Al-G probes (purchased from Budget Sensors) were used, and the instrument was operating in contact mode to record the topography images repeatedly in the solution. The data obtained were processed with the Gwyddion software. The total immersion time was around 4 h. The experiments were terminated when considerable corrosion products were formed on the sample surface. Further, smooth and tight Cu/Ru interface areas were chosen for the in situ AFM and KFM mapping, in order to avoid other disturbing factors caused by the interface preparation.

5.1.4 Electrochemical Experiments

All the electrochemical measurements were carried out using a three-electrode electrochemical cell, at room temperature (22 °C). An Ag/AgCl electrode and a bright platinum gauze acted as the reference electrode and counter electrode, respectively. The working electrode was the sample, i.e., Cu/Ru sample (shown in Fig. 5.1), pure Cu and pure Ru disks (5 mm in diameter), respectively. Prior to the measurement, the sample was polished to get a smooth surface/interface, then rinsed with MilliQ water and dried by N_2 gas stream. The electrolyte was the same as that mentioned in Sect. 5.1.1. First, the sample was exposed to the electrolyte and the OCP was recorded continuously for a period of time. It was ca. 40 min for pure Cu and Ru samples to reach a stable OCP, and more than 2 h for the Cu/Ru couple samples to follow the evolution of the mixed potential of the Cu/Ru couple. Then the EIS measurements were performed at the OCP of the sample, using a Solartron instruments (1287 Interface and 1250 frequency response analyzer). The EIS spectra were recorded in a frequency range from 10 kHz to10 MHz, with 10 mV amplitude of the applied AC potential. The data were processed using the PowerSuite and PowerSINE software.

5.2 Corrosion Tendency of the Metal Components

It is generally agreed that the Volta potential difference, rather than the absolute value of the potential, can be used as an indication of the relative nobility of the metals presented at the interface, which determines their role in galvanic corrosion (Femenia et al. 2003; Forslund et al. 2013). Therefore, in this section the discussion is focused on the measured Volta potential difference across the Cu/Ru interface. In the surface topography images shown in Fig. 5.2a and d, Ru side is higher than Cu side. This is due to a much higher hardness of Ru (6.5 on the Mohs scale) than that

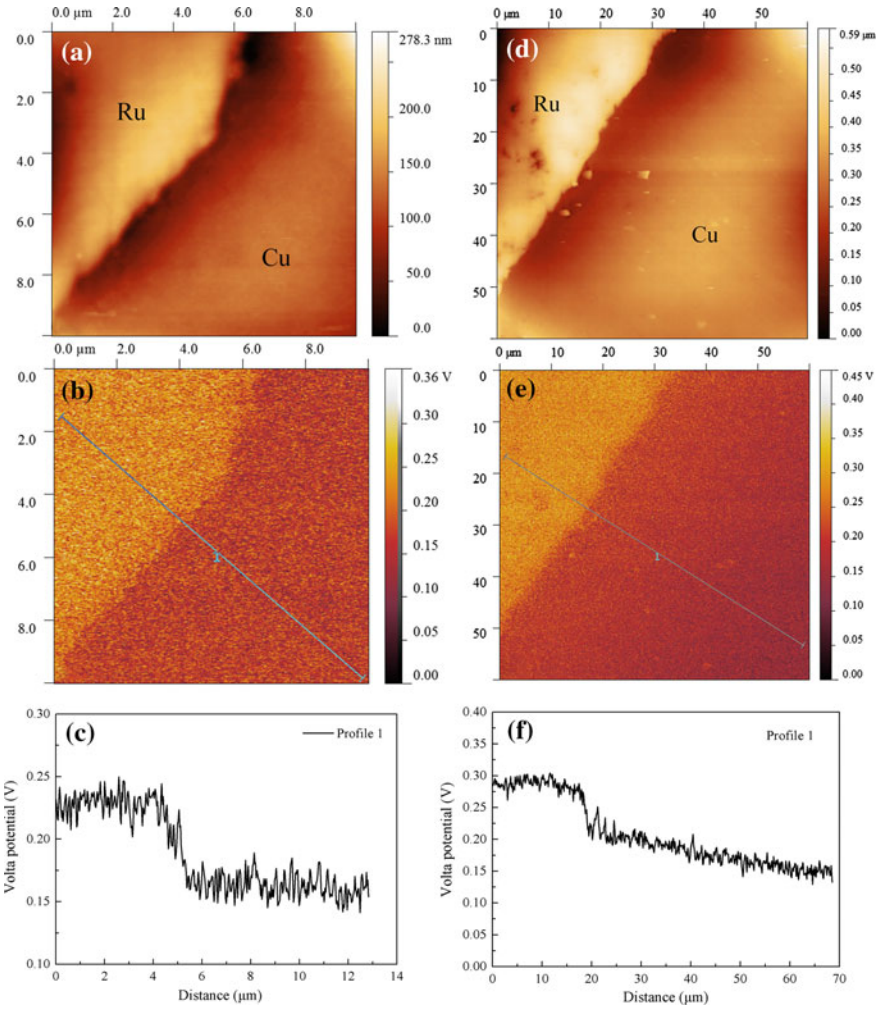

Fig. 5.2 KFM experimental results on the Cu/Ru interface: **a** and **d** surface topography; **b** and **e** relevant surface potential mapping; **c** and **f** surface potential profile across the interface. The scan area for **a**–**c** is 10 μm, and that for **d**–**f** is 60 μm

of Cu (Dey et al. 2004), resulting in an unavoidable uneven interface after the grinding/polishing process. Figure 5.2a–c show the KFM results from a scanned area of 10 μm in size: surface topography (a), Volta potential (b) and potential profile (c) across the Cu/Ru interface. There are some surface defects visible in the surface topography image. The Volta potential image shows a clear boundary at the Cu/Ru interface, but not topographic features. It appears that the Volta potential only depends on intrinsic properties of the two metals. The Ru exhibits a higher Volta potential (brighter in Fig. 5.2b) as compared to Cu, which suggests a cathodic

character of Ru in the micro-galvanic corrosion process. Thus, it is expected that in corrosive solutions Cu has a higher corrosion tendency than Ru, and accelerated corrosion occurs on the Cu surface of the Cu/Ru couple (Guillaumin et al. 2001).

With a larger scan area (60 μm in size), the KFM images show an interesting phenomenon, see Fig. 5.2d–f. The line profile depicted in Fig. 5.2f indicates an apparent downtrend of the Volta potential from the Cu/Ru interface to the interior Cu part. It is well-known that the KFM data are affected by the surface condition of the sample, especially the surface adsorption and passive film (Davoodi et al. 2008). Prior to and during the Volta potential measurement, the sample was exposed in air, so unavoidably the Cu surface was oxidized to form Cu_2O because of oxygen and humidity in the air (Jiang et al. 2002). For galvanic couples, the current distribution is not uniform. It depends on polarization of the anode and cathode, the conductivity of the electrolyte, and the geometry of the couple (Copson 1943). The low polarization of Cu, low conductivity of air and adsorbed water layer probably lead to more galvanic attack near the junction of Cu/Ru. Therefore, the oxidation of Cu could be more accelerated near the junction, as compared with the area far from the Cu/Ru interface. Therefore, the Volta potential value increases from the Cu interior to the Cu/Ru junction, see Fig. 5.2f, due to more oxidized surface. Similar phenomenon was also observed in the in situ AFM experiments, as will be discussed in Sect. 5.5.1.

5.3 Corrosion Products Analysis

After ca. 4 h' in situ AFM experiments in 0.015 M KIO_4 solution, a green gel-like precipitate formed on the Cu/Ru sample, mainly covering the Cu part of the Cu/Ru junction, as shown in Fig. 5.3. Complicated chemical reactions may take place on

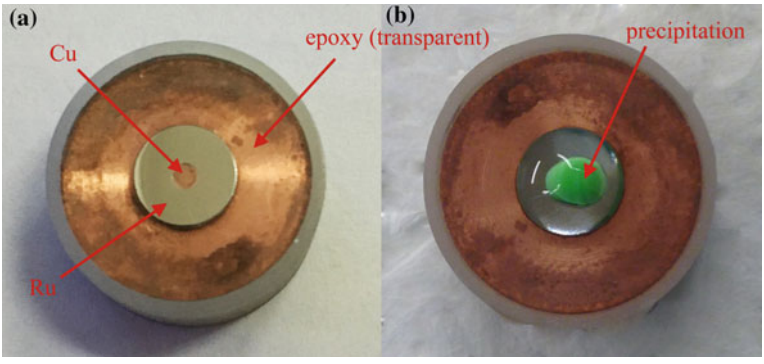

Fig. 5.3 The Cu/Ru sample **a** before the in situ AFM experiments after polishing and **b** after the in situ AFM experiments

the Cu/Ru sample in the KIO_4 solution (Amanapu et al. 2013; Peethala and Babu 2011). The main anodic reactions are given as follows:

$$2Cu + 2OH^- = Cu_2O + H_2O + 2e^- \tag{5.1}$$

$$Cu_2O + 2OH^- = 2CuO + H_2O + 2e^- \tag{5.2}$$

$$Ru + 4H_2O = RuO_2 \cdot 2H_2O + 4H^+ + 4e^- \tag{5.3}$$

The main cathodic reactions are the reduction of IO_4^- and oxygen, as expressed below:

$$IO_4^- + H_2O + 2e^- = IO_3^- + 2OH^- \tag{5.4}$$

$$O_2 + 2H_2O + 4e^- = 4OH^- \tag{5.5}$$

In previous investigations, it was found that the passive film formed on Cu in the KIO_4-based slurry for the CMP process is quite complex. Under weak alkaline conditions, not only Cu_2O/CuO, but also a small amount of $Cu(IO_3)_2$ or $Cu(IO_3)_2 \cdot nH_2O$, was formed on the Cu surface. The solubility (Ksp) of $Cu(IO_3)_2$ at 25 °C is 1.4×10^{-7} (Leckie and Davis 1979), thus $Cu(IO_3)_2$ could be regarded as an insoluble substance, which can form on Cu surface as a stable reaction product. Moreover, the quantity of $Cu(IO_3)_2 \cdot nH_2O$ formed on an uncoupled Cu surface is small in static immersion experiments, and it is not easy to be detected by Raman analysis. In this study, the formation of the green gel-like precipitated corrosion product is a result of local accelerated corrosion of Cu near the Cu/Ru interface. CRM spectra provide chemical information about the precipitated product. Figure 5.4 shows a representative CRM spectrum of the corrosion products covering the Cu/Ru interface. The peak at 844 cm^{-1} can be assigned to IO_4^-, as the presence of tetrahedral IO_4^- ion is indicated by a strong peak at ca. 850 cm^{-1} (v_3 triply degenerate

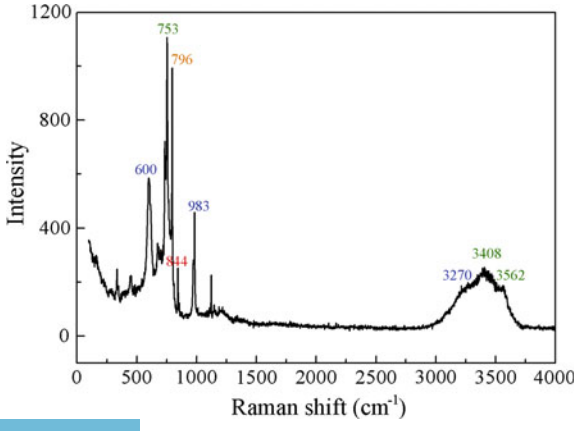

Fig. 5.4 The CRM spectrum of the precipitation formed on the Cu/Ru interface. The Raman shifts of peaks at 753, 3408 and 3562 cm^{-1} refer to $Cu(IO_3)_2 \cdot nH_2O$; The shifts at 600, 983 and 3270 cm^{-1} are assigned to $CuSO_4 \cdot nH_2O$; The shift at 796 cm^{-1} implies the presence of IO_3^-; The shift at 844 cm^{-1} indicates v_3 vibration of IO_4^-

vibration) (Levason 1997). The peak at 796 cm^{-1} is attributed to the presence of IO_3^- (Li et al. 2002), resulted from the reduction of KIO_4. There is a broad band from ca. 3000 to 3700 cm^{-1}, which includes symmetric stretching (v_1) and antisymmetric stretching (v_3) modes of water molecules, indicating the formation of hydrates (Degen and Newman 1993). It should be mentioned that there were some SO_4^{2-} ions in the solution, thus indicating a possibility for formation of $CuSO_4 \cdot nH_2O$ (blue in color). The peaks at 600, 983 and 3270 cm^{-1} could be associated with the presence of $CuSO_4 \cdot nH_2O$ (Fu et al. 2012). However, the precipitate formed on the Cu/Ru interface is green, which could be the color of $Cu(IO_3)_2 \cdot nH_2O$. Early investigations show that the peaks at 753, 3408 and 3562 cm^{-1} are associated with the presence of $Cu(IO_3)_2 \cdot nH_2O$ (Pracht et al. 1997). The peak at 753 cm^{-1} is assigned to I–O stretching mode, and the 3408 and 3562 cm^{-1} bands are caused by the vibration of O–H stretching in water molecules. In short, the CRM spectra suggest the formation of $Cu(IO_3)_2 \cdot nH_2O$ on the Cu/Ru interface.

5.4 Electrochemical Behavior of the Cu/Ru Couple

5.4.1 *Corrosion Tendency in KIO_4 Solution*

OCP and EIS measurements provide information about electrochemical characteristics of the system, such as dominating reactions in the corrosion process, resistive and capacitive properties of the sample in the solution. Separate measurements of pure Cu and Ru samples were also made for comparison with the Cu/Ru couple sample. The OCP was recorded continuously for a certain period, and then the EIS experiments were performed when the sample reached a steady state condition. For the Cu/Ru sample, the EIS spectra were obtained after the green precipitation appeared.

The variations of the OCP with time for the Cu, Ru and Cu/Ru samples are displayed in Fig. 5.5. Within a short period (ca. 50 s), the OCPs of Cu and Ru

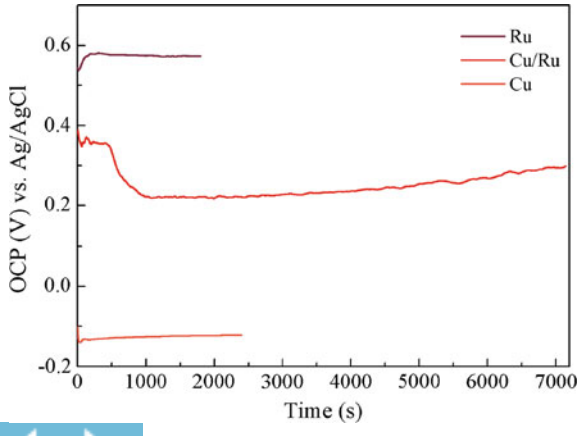

Fig. 5.5 Open circuit potential comparison between the Ru, Cu/Ru and Cu samples. The solution contains 0.015 M KIO_4 and the pH value is 9

samples reach a stable value. The curve for the Cu/Ru sample indicates the change in the mixed potential of the Cu/Ru couple in the solution. Comparatively, more time is needed for the Cu/Ru sample to reach a stable value. As expected, the OCP of the Cu/Ru lies between that of Ru and Cu (Maruyama et al. 2009). During the early period (up to 500 s), the OCP is around 0.36 V versus Ag/AgCl, but quickly drops to 0.22 V afterwards, and remains quite stable for a certain period and later increases slightly during the prolonged exposure. In general, being a mixed potential, the OCP of a metal in an electrolyte is determined by the coupling between the anodic reaction(s) and cathodic reaction(s) as well as the electrolyte resistance. The variation of the OCP with time reflects the changes of the surface condition, e.g., dissolution of native oxide film on the surface in the beginning, corrosion and dissolution of metal ions, and eventual formation of precipitated corrosion product on the surface during prolonged exposure. It has been investigated in Chap. 2 that, during the exposure, a thicker non-compact surface film is formed on the sample in such a system, mainly composed of $CuO/Cu_2O/Cu(IO_3)_2{\cdot}nH_2O$. That could be the reason why the OCP shifts towards that of Ru over the extended period of time. The OCP results are discussed in more detail together with in situ AFM observations (Sect. 5.5.1). The sample preparation, polishing effect, the Cu/Ru junction interface, etc., could affect the experiment results, giving some scattering between parallel measurements, but all the experimental results show the same trend. It should be noted that for pure Cu, both in static immersion experiments and CMP experiments, there is no obvious growth of $Cu(IO_3)_2{\cdot}nH_2O$. Therefore, it can be concluded that the galvanic effect accelerates the Cu corrosion in the Cu/Ru coupling, and results in the formation of $Cu(IO_3)_2{\cdot}nH_2O$ precipitate.

5.4.2 EIS Results

Typical EIS spectra obtained for Cu, Ru and Cu/Ru samples are shown in Figs. 5.6 and 5.7, in Nyquist plots and Bode plots, respectively. The spectra of the Ru and

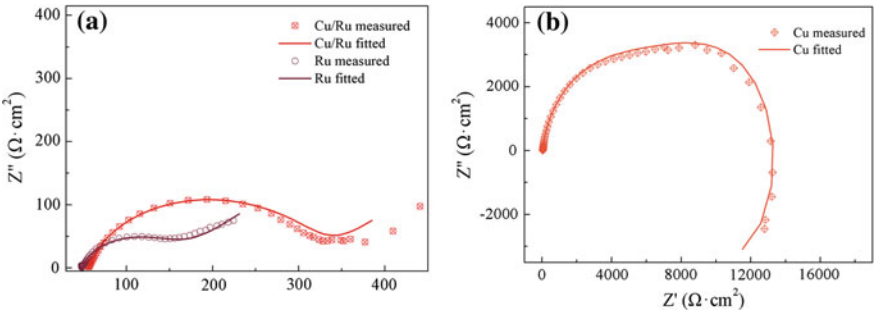

Fig. 5.6 EIS Nyquist plots in KIO_4 solutions at pH 9 for: **a** Cu/Ru and Ru samples; **b** Cu sample

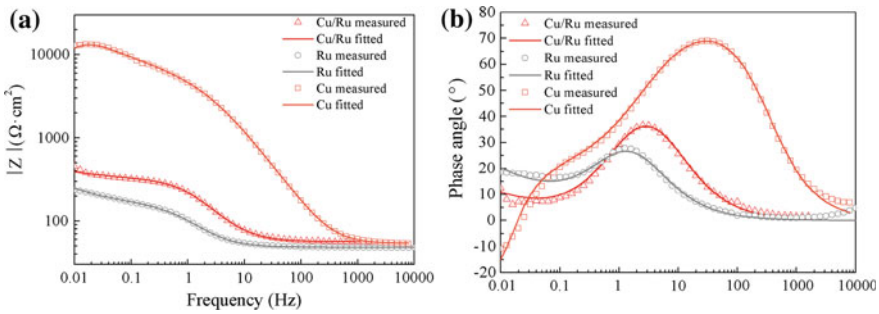

Fig. 5.7 EIS data for Ru, Cu/Ru and Cu samples in 0.015 M KIO_4 solution at pH 9: **a** modulus diagram of Bode plots; **b** phase diagram of Bode plots

Cu/Ru samples are similar, showing one time constant feature typical for a corroding interface and a small diffusion-like tail at low frequencies. In the medium and low frequency regions, the impedance modulus values of the Cu/Ru sample are close to that of the Ru sample, but much lower than that of the Cu sample. In contrast, the Cu sample exhibits more complicated spectra with an inductive response (negative values of the phase angle) at low frequencies. The EIS results indicate that, in the steady state, the Cu/Ru couple exhibits similar electrochemical behavior as the Ru sample. Probably, this is because the electrochemical reactions mainly take place on the Ru part, since the whole Cu surface is covered by the precipitated $Cu(IO_3)_2 \cdot nH_2O$.

The EIS results were analyzed by spectra fitting using simple equivalent circuits commonly used for metal corrosion processes. For the Cu/Ru and Ru samples, the EIS data could be fitted using the simple model for corroding interface with diffusional transport of reactant and/or reaction product, i.e., equivalent circuit (a) in Fig. 5.8. In this circuit, R_s refers to the solution resistance, R_{ct} the charge transfer resistance, Q_1 the double layer capacitance, and the Warburg impedance (W) represents a diffusion-limited mass transfer, indicating a uniform corrosion process on the Ru surface. Here, a constant phase element (CPE) is used instead of

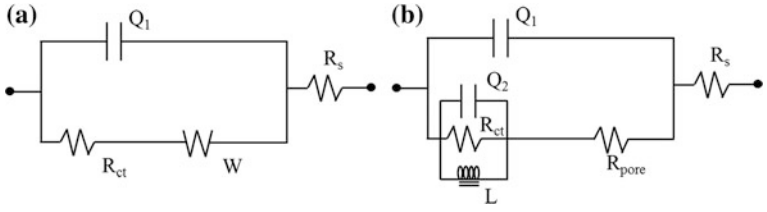

Fig. 5.8 Equivalent circuits of the impedance spectra obtained in 0.015 M KIO_4 solution at pH 9 for **a** Cu/Ru and Ru samples **b** Cu sample

a pure capacitor to take into account the deviation from the ideal dielectric behavior, which could be caused by the surface heterogeneities.

For the Cu sample, the impedance modulus at low frequencies (ca. $10^4\ \Omega\ cm^2$) is much higher than those of the Ru and Cu/Ru samples. The data at low frequencies indicate an inductive response, as is seen in Fig. 5.6b. In general, such inductive response is related to the relaxation of surface adsorption of charged species involved in cathodic and/or anodic reactions (Cordoba-Torres et al. 2008). In this case, it is likely due to active dissolution of Cu in the solution. The surface film formed on Cu under this condition is heterogeneous and non-uniform. Thus, a model considering the porous surface film as well as the inductance, shown in Fig. 5.8b, is utilized for the spectra fitting (Cheng et al. 1998; Tsai et al. 2003). Here, an inductance (L) is in parallel with R_{ct}, and Q_2 is the non-ideal capacitance, all associated to electrochemical processes occurring in the porous surface film. R_{pore} represents the ohmic resistance of the porous surface film. Satisfactory fitting quality is obtained by using this equivalent circuit.

The values of the circuit elements from the spectra fitting are listed in Table 5.1. As expected, the fitting data for the Ru and Cu/Ru samples are quite similar. It has been proved that corrosion of Ru is slow and uniform in such a system. Here, the low R_{ct} value of the Ru sample is indicative for its good catalytic property for the electrochemical reactions rather than a low corrosion resistance. For pure Cu, the relatively high resistance of the surface film dominants the impedance response at low frequencies. This implies that the formation of $Cu(IO_3)_2{\cdot}nH_2O$, the main composition of the surface film, could act as a barrier, protecting Cu from further dissolution.

Table 5.1 EIS fitting parameters using the equivalent circuits shown in Fig. 5.8

	Ru	Cu/Ru	Cu
R_s ($\Omega\ cm^2$)	48.48 (0.48)	56.17 (1.15)	53.58 (0.22)
n_1	8.54×10^{-1} (1.81×10^{-2})	8.52×10^{-1} (4.23×10^{-3})	9.19×10^{-1} (7.07×10^{-3})
Q_1 ($\Omega^{-1}\ cm^{-2}\ s^n$)	2.40×10^{-3} (2.29×10^{-4})	7.51×10^{-4} (1.53×10^{-4})	1.63×10^{-5} (2.82×10^{-6})
R_{pore} (Ω)			6229.52 (406.25)
R_{ct} (Ω)	109.10 (4.41)	265.32 (15.01)	1335.08 (195.88)
Q_2 ($\Omega^{-1}\ cm^{-2}\ s^n$)			1.29×10^{-4} (1.66×10^{-5})
n_2			6.26×10^{-1}(3.58×10^{-3})
W ($\Omega^{-1}\ cm^{-2}\ s^{0.5}$)	3.46×10^{-2} (1.37×10^{-3})	4.11×10^{-2} (6.61×10^{-3})	
L ($H^{-1}\ cm^{-2}$)			2.54×10^5 (1.00×10^4)

5.5 Corrosion Kinetics of Cu/Ru Sample

5.5.1 *Development of Galvanic Corrosion at Cu/Ru Interface*

Figures 5.9 and 5.10 display the AFM topography images obtained on the Cu/Ru sample, showing the topography changes of the Cu/Ru interfacial area during the ca. 4 h' exposure. Figure 5.9 shows the sample surface prior to exposure, and Fig. 5.10 shows sequential in situ images obtained after different time intervals. The scanned position had a slight drift during the in situ AFM experiment. It can be seen from Fig. 5.10a that the Cu part corrodes preferentially, resulting in small voids and probably also some corrosion product particles, and apparently the surface becomes rough and porous. At microscopic scale, corrosion is not uniform, because corrosion usually initiates from surface defects such as grain boundaries or manufacturing defects (Balyanov et al. 2004). In Fig. 5.10b–d, it is noticeable that after ca. 120 min' exposure, many new dots appear and grow on the Cu surface, and quickly cover the whole surface, so the image of the Cu surface becomes blurred. According to the CRM analysis, the precipitated corrosion product composes mainly of $Cu(IO_3)_2{\cdot}nH_2O$. Figure 5.11 shows height profiles along the line labeled in Fig. 5.10d, obtained at the same position after different time intervals. The gray-marked region indicates the Cu side of the Cu/Ru interface. It can be seen that the gray part on Cu became increasingly deeper with the exposure time. This is an evidence of accelerated corrosion of Cu in the Cu/Ru couple due to the galvanic effect. Apart from this, the Cu surface becomes quite smooth, due to the formation of $Cu(IO_3)_2{\cdot}nH_2O$ precipitate covering the whole Cu surface.

In fact, the topography changes on the Cu/Ru sample are in line with the time evolution of the OCP. At the beginning of the exposure, the OCP remains to be

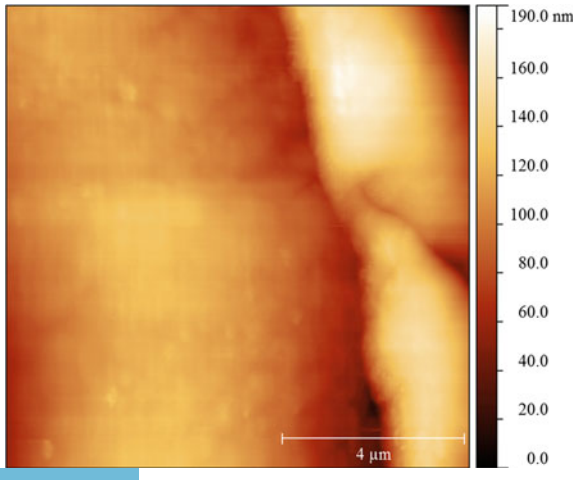

Fig. 5.9 Topography of Cu/Ru sample in air before in situ AFM experiments

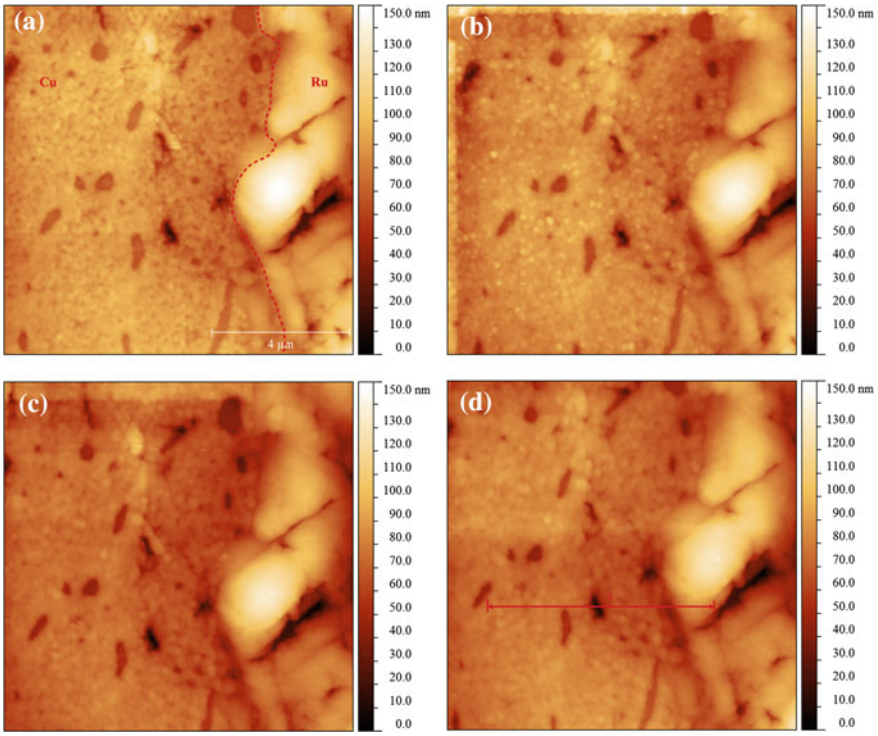

Fig. 5.10 In-situ AFM topography changes in solution after immersion for **a** 23–29 min; **b** 111–118 min; **c** 132–139 min; **d** 236–243 min. The scan area is 10 × 10 μm

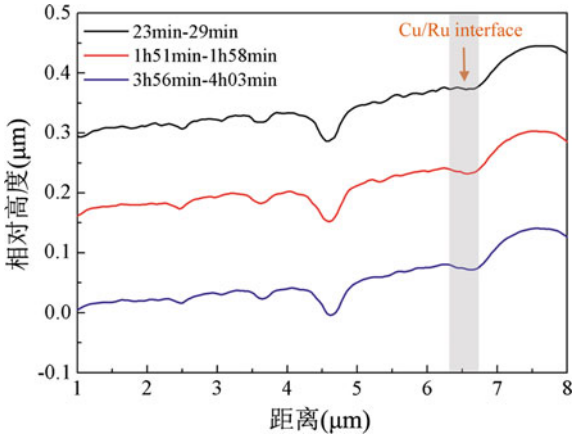

Fig. 5.11 Profile changes of Line 1 indicated in Fig. 5.10d

stable at a relatively higher level, due to the protective thin oxide film formed on the surface in air. The sharp drop of OCP is caused by the breakdown of the native oxide and accelerated oxidation and dissolution of Cu by the galvanic effect. The OCP remains to be quite low for a certain period, but shows a slight increasing trend in the later period of exposure, which is likely related to the large amount of precipitate [$Cu(IO_3)_2 \cdot nH_2O$] gradually covering the whole Cu/Ru interface and Cu surface, inhibiting further Cu corrosion.

5.5.2 *Galvanic Corrosion Mechanism at Cu/Ru Interface*

When Cu/Ru interface is exposed to KIO_4 solutions, the balance of the corrosion process for separated Cu and Ru are changed, and galvanic corrosion effect is generated. The corrosion potential for Ru is high, and therefore Ru acts as the cathode, the surface of which is the main place for cathodic reactions. However for Cu, the corrosion potential is comparatively low, and Cu acts as the anode, the surface of which is the main place for anodic reactions. Due to the galvanic corrosion effect, both the cathodic and anodic reactions are accelerated in the Cu/Ru system. For Cu, the corrosion/dissolution of Cu is accelerated while for Ru, the surface is protected because Ru mainly provides sites for the cathodic reactions.

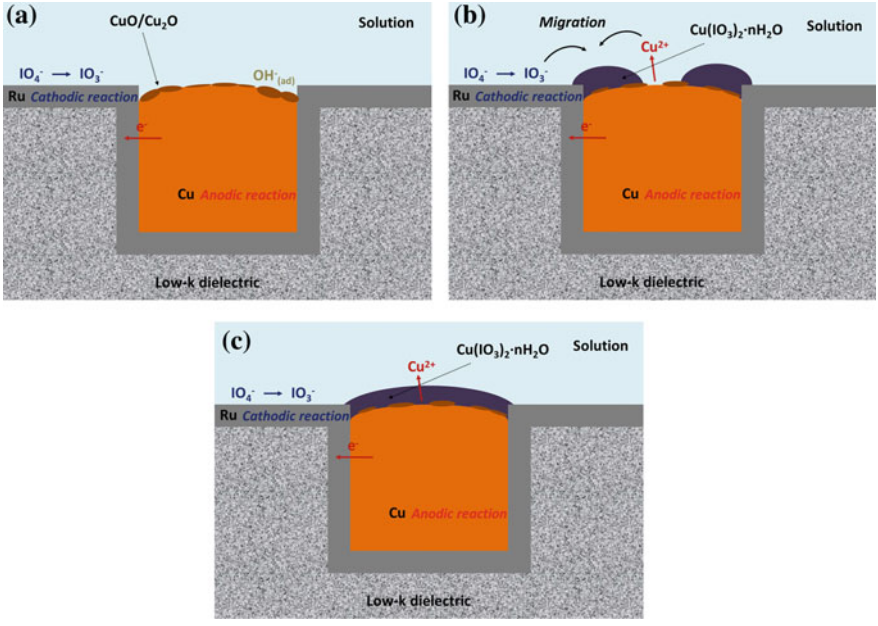

Fig. 5.12 Scheme of the galvanic corrosion mechanism of Cu/Ru interconnects in KIO_4 solution: **a** immune stage; **b** accelerative stage; **c** stabilized stage

Therefore, it could be concluded that the galvanic corrosion occurring on the Cu/Ru interface in KIO_4 solution develops periodically. The whole process could be divided into three typical periods, which is schematically illustrated in Fig. 5.12:

(i) The immune stage: initially, the oxide film (mainly composed of Cu/Cu_2O) on Cu formed in air is protective, and it could prevent Cu from accelerated corrosion caused by the galvanic corrosion effect of Cu/Ru contact.
(ii) The accelerative stage: there happens a transient alternating process of the dissolution and formation of surface oxide film on Cu, causing the breakdown of the native oxide on Cu surface; subsequently the oxidation and dissolution of Cu is boosted by the galvanic effect; simultaneously, Cu^{2+} reacts with IO_3^-, forming a large amount of insoluble $Cu(IO_3)_2{\cdot}nH_2O$ on Cu/Ru interface.
(iii) The stable stage: the formation of insoluble $Cu(IO_3)_2{\cdot}nH_2O$ quickly spreads over the Cu surface, together with Cu oxide, acting as corrosion obstruction; the corrosion of Cu is decelerated and the galvanic corrosion process is stabilized from then on.

5.6 Conclusions

Motivated by the introduction of Ru barrier layer in Cu interconnection in sub-14 nm technology node for manufacturing of ultra-large scale integrated circuit, this chapter focuses on clarifying the mechanism of micro-galvanic corrosion between Cu and Ru in alkaline solution with KIO_4 as oxidant, by using a model sample with Cu/Ru couple. Based on the results from Volta potential mapping, in situ AFM measurements, electrochemical OCP and EIS measurements in 0.015 M KIO_4 solution, and chemical analysis of the corrosion products, following conclusions can be drawn:

Cu exhibits lower practical nobility (less noble) than Ru, and the Volta potential of Cu decreases gradually with increasing distance from the Cu/Ru interface.

Cu acts as the anode in the Cu/Ru couple during the exposure in the KIO_4 solution, and the corrosion of Cu in Cu/Ru couple develops in different stages. Initially, the native surface oxide of Cu is protective, but dissolves quickly in the solution, and the accelerated corrosion of Cu takes place near the Cu/Ru interface due to the galvanic coupling effect. After the initial period, the accelerated Cu dissolution leads to formation of an insoluble compound composed mainly of $Cu(IO_3)_2{\cdot}nH_2O$ that precipitates on the Cu surface. This precipitated corrosion product acts as a barrier, which mitigates further corrosion of Cu.

References

Amanapu HP, Sagi KV, Teugels LG, Babu SV (2013) Role of guanidine carbonate and crystal orientation on chemical mechanical polishing of ruthenium films. ECS J Solid State Sci Tech 2 (11):P445–P451

Balyanov A, Kutnyakova J, Amirkhanova NA, Stolyarov VV, Valiev RZ, Liao XZ, Zhao YH, Jiang YB, Xu HF, Lowe TC, Zhu YT (2004) Corrosion resistance of ultra fine-grained Ti. Scripta Mater 51(3):225–229

Cheng X, Li G, Kneer EA, Vermeire B, Parks HG, Raghavan S, Jeon JS (1998) Electrochemical impedance spectroscopy of copper deposition on silicon from dilute hydrofluoric acid solutions. J Electrochem Soc 145(1):352–357

Copson HR (1943) Distribution of galvanic corrosion. Trans Electrochem Soc 84(1):71–82

Cordoba-Torres P, Keddam M, Nogueira RP (2008) On the intrinsic electrochemical nature of the inductance in EIS: a Monte Carlo simulation of the two-consecutive-step mechanism: the flat surface 2D case. Electrochim Acta 54(2):518–523

Davoodi A, Pan J, Leygraf C, Norgren S (2008) The role of intermetallic particles in localized corrosion of an aluminum alloy studied by SKPFM and integrated AFM/SECM. J Electrochem Soc 155(5):C211–C218

Degen IA, Newman GA (1993) Raman spectra of inorganic ions. Spectrochim Acta, Part A 49 (5):859–887

Dey SK, Goswami J, Gu D, de Waard H, Marcus S, Werkhoven C (2004) Ruthenium films by digital chemical vapor deposition: selectivity, nanostructure, and work function. Appl Phys Lett 84(9):1606–1608

Femenia M, Canalias C, Pan J, Leygraf C (2003) Scanning Kelvin probe force microscopy and magnetic force microscopy for characterization of duplex stainless steels. J Electrochem Soc 150(6):B274–B281

Forslund M, Leygraf C, Claesson PM, Lin C, Pan J (2013) Micro-galvanic corrosion effects on patterned copper-zinc samples during exposure in humidified air containing formic acid. J Electrochem Soc 160(9):C423–C431

Fu X, Yang G, Sun J, Zhou J (2012) Vibrational spectra of copper sulfate hydrates investigated with low-temperature Raman spectroscopy and terahertz time domain spectroscopy. J of Phys Chem A 116(27):7314–7318

Guillaumin V, Schmutz P, Frankel GS (2001) Characterization of corrosion interfaces by the scanning Kelvin probe force microscopy technique. J Electrochem Soc 148(5):B163–B173

Jiang X, Herricks T, Xia Y (2002) CuO nanowires can be synthesized by heating copper substrates in air. Nano Lett 2(12):1333–1338

Leckie JO, Davis JA (1979) Aqueous environmental chemistry of copper. Copper in the Env 1:89

Levason W (1997) The coordination chemistry of periodate and tellurate ligands. Coord chem Rev 161:33–79

Li ZL, Ren B, Xiao XM, Zeng Y, Chu X, Tian ZQ (2002) Further insight into the origin of potential oscillations during the iodate reduction in alkaline solution with mass transfer. J Phys Chem A 106(28):6570–6573

Maruyama K, Shiohara M, Yamada K, Kondo S, Saito S (2009) Galvanic corrosion control in chemical mechanical polishing of Cu interconnects with ruthenium barrier metal film. Jpn J Appl Phys 48(4S):4C–22C

Peethala BC, Babu SV (2011) Ruthenium polishing using potassium periodate as the oxidizer and silica abrasives. J Electrochem Soc 158(3):H271–H276

Pracht G, Lange N, Lutz HD (1997) High-temperature Raman spectroscopic studies on nickel iodates. Thermochim Acta 293(1):13–24

Tsai T, Wu Y, Yen S (2003) A study of copper chemical mechanical polishing in urea-hydrogen peroxide slurry by electrochemical impedance spectroscopy. Appl Surf Sci 214(1):120–135

Chapter 6
Galvanic Corrosion Inhibitors for Cu/Ru Couple During Chemical Mechanical Polishing of Ru

6.1 Experimental

6.1.1 Electrochemical Experiments

It is commonly recognized that a bigger corrosion potential difference (ΔE_{cor}) between two metals will cause a serious tendency of galvanic corrosion, and therefore a minimal ΔE_{cor} is the goal when evaluating the corrosion inhibition effect of various inhibitors in most of the relevant researches. However, practical corrosion process is influenced by many other factors such as the area ratio of anode/cathode, and the properties of the surface passive film (Copson 1943). Therefore, it is ideal if the galvanic corrosion current (i_g) could be directly measured. The general approach to estimate the i_g of Cu is to measure the intersection of Cu anodic branch and Ru cathodic branch by conducting the electrochemical potentiodynamic polarization measurements, as is schematically shown in Fig. 6.1a. The measurement is based upon an assumption that all the cathodic reactions take place on Ru while all the anodic reactions on Cu, which does not agree with most of the actual conditions. In this paper, the i_g of Cu is directly measured by a galvanometer set on a potentiostat, as depicted in Fig. 6.1b. In this way, i_g represents the accelerated corrosion of Cu caused by the Cu and Ru contact, and further could quantitatively evaluate the corrosion inhibition effect of corrosion inhibitors.

All the electrochemical experiments were conducted in a chemical lab where the relative humidity was around 30% and the temperature in the range of 23–25 °C. The galvanic corrosion current measurement was conducted on a potentiostat (M273A EG&G, Princeton Applied Research). Ru and Cu disks (99.99% purity) were sealed in epoxy with an exposure area of 5 mm in diameter. Ru served as the auxiliary and reference electrodes at the same time, while Cu acted as the working electrode, as shown in Fig. 6.1b. In this way, a simple galvanometer was set, and the galvanic corrosion current between Ru and Cu could be directly measured. The

J. Cheng, *Research on Chemical Mechanical Polishing Mechanism of Novel Diffusion Barrier Ru for Cu Interconnect*, Springer Theses,
DOI 10.1007/978-981-10-6165-3_6

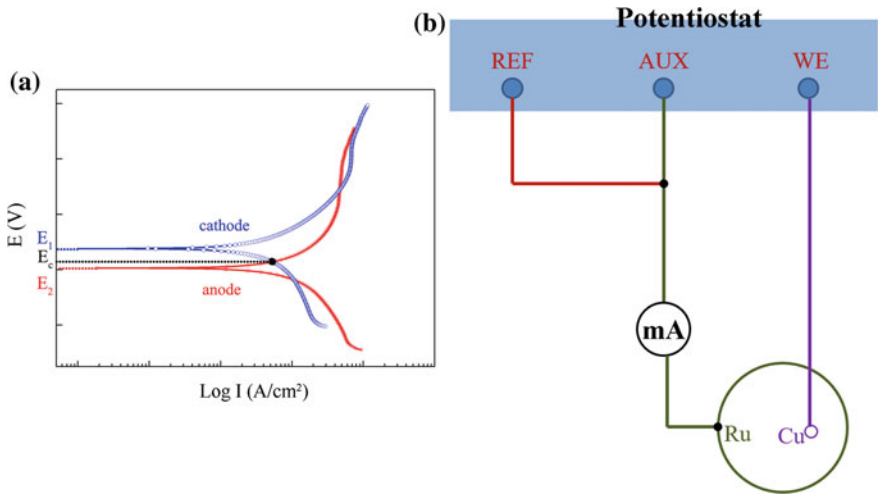

Fig. 6.1 The scheme of **a** the general method to estimate the galvanic corrosion current; **b** the galvanic corrosion meter used in this chapter

solution used contained different oxidants (H_2O_2 and KIO_4) and inhibitors (BTA and 1, 2, 4-triazole). No abrasives were added to the solutions to eliminate other disruptive factors. The pH value was adjusted to 9.5 using KOH/H_2SO_4 adjustors. The measurements were stopped until the current density is comparatively stable (1800 s), at which time the value of corrosion current density was the i_g got under this experimental condition.

For the open circuit potential (OCP) measurements, the whole experiments lasted for 600 s. The Ru or Cu electrode (same as stated hereinabove) was the working electrode. A platinum and Ag/AgCl (3.5 M) worked as the auxiliary and reference electrodes, respectively. Before each measurement, the surface of the working electrode was ground on 2000# SiC abrasive paper, rinsed with DI water, and dried in N_2 gas.

6.1.2 Surface and Interface Characterization

The surface tension of solutions is used to characterize the surface and interface properties of the slurry/wafer during CMP (Tseng et al. 2001). It is well known that a lower surface tension often means a better adsorption property on wafer surface and a better mobility of the slurry. Solutions containing different inhibitors were measured by a surface tension meter (K12, KRuss).

To study the wettability of the slurry on wafer, the contact angles of the solutions on Ru and Cu surfaces were measured separately. The apparatus used was a contact angle meter (DCAT21, DATAPHYSICS). 3 μL solution was dropped onto the

metal surface by a microsyringe, and simultaneously the image of the drop was monitored by an optical microscopy. The samples were Ru coupons made by physical vapor deposition and Cu coupons by electroplating. The contact angle was then calculated by contour fitting.

6.2 Galvanic Corrosion Using Different Oxidants

Both H_2O_2 and KIO_4 are frequently used oxidants in barrier polishing process (Peethala and Babu 2011; Jiang et al. 2014). The current density of galvanic corrosion in Cu/Ru couple is measured when H_2O_2 (Fig. 6.2) and KIO_4 (Fig. 6.3) are used as oxidant. It could be seen from the original data that the values of the current are negative, indicating Cu is the anode in the Cu/Ru couple. The corrosion of Cu is

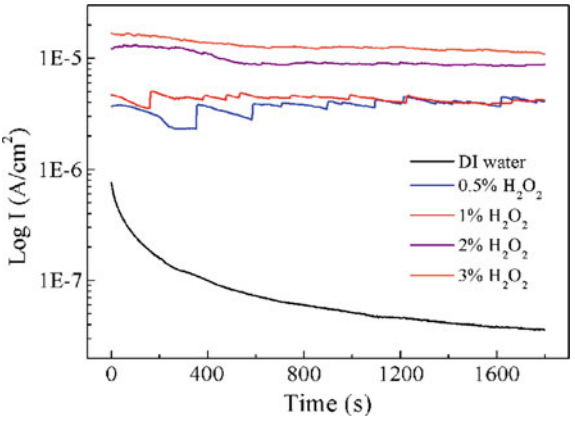

Fig. 6.2 The galvanic corrosion current density of Cu as a function of H_2O_2 content

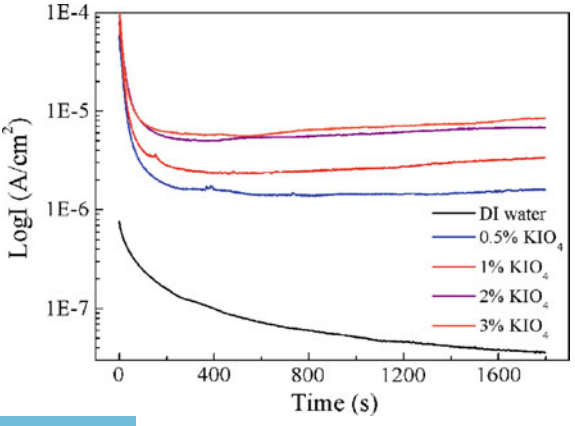

Fig. 6.3 The galvanic corrosion current density of Cu as a function of KIO_4 content

accelerated, which is in line with the expectation. Overall speaking, the galvanic corrosion rate is higher as the oxidant (both H_2O_2 and KIO_4) concentration increases. Comparatively, it takes a longer time to reach a steady state when KIO_4 is used as the oxidant, but the stability of the current is better under this condition. This phenomenon coincides well with the previous findings, that is, the subsequent formation of insoluble precipitates on Cu [mainly $Cu(IO_3)_2 \cdot nH_2O$] could act as corrosion obstruction, which will continuously decelerate the corrosion rate of Cu. When the mass percentage of H_2O_2 is 0.5% (0.147 M), the corrosion rate is 4.16 μA/cm^2; when the content of KIO_4 is 3% (0.130 M), the corrosion rate is 8.48 μA/cm^2. The two concentrations (0.147 M and 0.130 M) are comparative, but the corrosion rates are quite different. With KIO_4 as the oxidant, the galvanic corrosion rate is ca. 2 times higher than that of H_2O_2. That is, when polishing slurry contains KIO_4 as oxidant, the galvanic corrosion of Cu is much severe, which is in line with the previous researches. Therefore, the galvanic corrosion inhibition properties of inhibitors will be discussed below in KIO_4-based solutions.

6.3 Corrosion Inhibition Efficiencies of BTA and 1, 2, 4-Triazole

Benzotriazole (BTA) and triazoles are highly effective corrosion inhibitors for Cu by preventing undesirable surface reactions (Sherif et al. 2007; Brusic et al. 1991; Zhu and Free 2015). In terms of the application of polishing slurry inhibitors, both BTA and 1, 2, 4-triazole have been proved to enhance corrosion resistance for Cu and Ru during CMP in previous studies (Deshpande et al. 2004; Goonetilleke and Roy 2008). Figure 6.4 shows the structural formula of BTA and 1, 2, 4-triazole, the heterocyclic structure of which contains a variety of donor atoms. The corrosion inhibition of them is usually attributed to the interaction with metal (Cu and Ru) surface via physical or chemical adsorption.

Figures 6.5 and 6.6 are the galvanic corrosion rate of Cu when BTA and 1, 2, 4-triazole are added into 0.5% KIO_4 solution, respectively. It is obvious that BTA and 1, 2, 4-triazole could significantly suppress the corrosion rate of Cu, indicating that both of them are effective galvanic corrosion inhibitors. However, the effects of concentrations show different things. Figure 6.7 compares the corrosion inhibition of BTA and 1, 2, 4-triazole at different concentrations. For BTA, the corrosion rate continuously decreases when the concentration of BTA increases from 1 mM and on. It should be noted that when the concentration of BTA is 0.5 mM, the corrosion rate is even higher (2.4 μA/cm^2) than that without inhibitors (1.6 μA/cm^2). The small

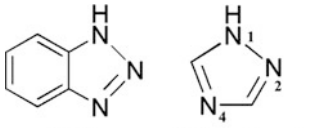

Fig. 6.4 The structural formula of BTA and 1, 2, 4-triazole

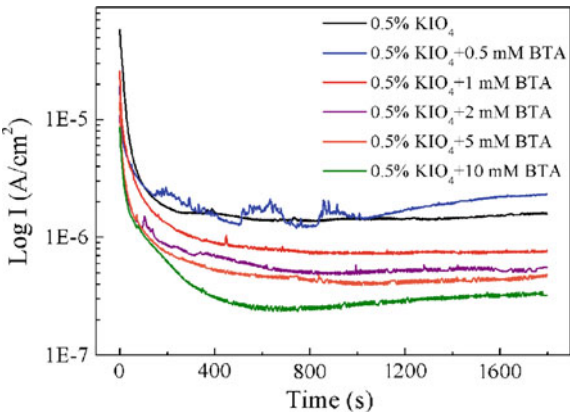

Fig. 6.5 The galvanic corrosion current density of Cu as a function of BTA concentrations

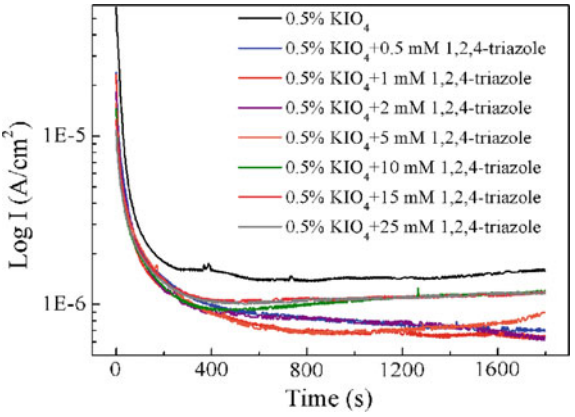

Fig. 6.6 The galvanic corrosion current density of Cu as a function of 1, 2, 4-triazole concentrations

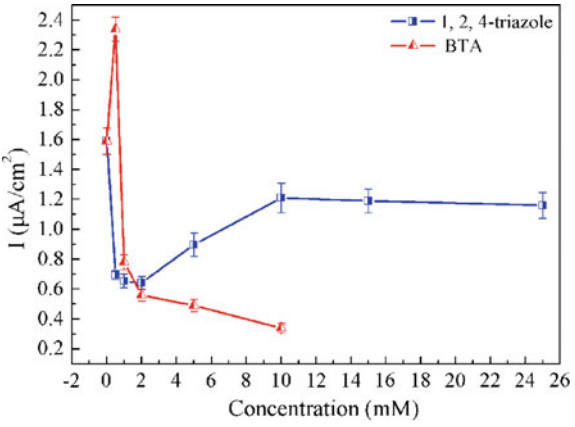

Fig. 6.7 The comparison of the galvanic corrosion rate of Cu when BTA and 1, 2, 4-triazole are used as inhibitors

Table 6.1 The efficiency of Cu galvanic corrosion inhibition (*CIE*) in KIO_4 solution

Solutions	*CIE*	Solutions	*CIE*
0.5% KIO_4 + 0.5 mM BTA	–	0.5% KIO_4 + 0.5 mM 1, 2, 4-triazole	56.4
0.5% KIO_4 + 1 mM BTA	51.3	0.5% KIO_4 + 1 mM 1, 2, 4-triazole	58.9
0.5% KIO_4 + 2 mM BTA	65.0	0.5% KIO_4 + 2 mM 1, 2, 4-triazole	59.7
0.5% KIO_4 + 5 mM BTA	69.4	0.5% KIO_4 + 5 mM 1, 2, 4-triazole	43.6
0.5% KIO_4 + 10 mM BTA	79.6	0.5% KIO_4 + 10 mM 1, 2, 4-triazole	23.9
		0.5% KIO_4 + 15 mM 1, 2, 4-triazole	25.2
		0.5% KIO_4 + 25 mM 1, 2, 4-triazole	27.0

amount of BTA does not have corrosion inhibition effect, and conversely it aggravates the corrosion of Cu. This phenomenon has been reported previously that BTA is an anodic type inhibitor, the insufficient dosage of which could cause severe pitting at the areas without passivation (Costa et al. 1990; Walker 1975).

With regard to 1, 2, 4-triazole, the lowest corrosion rate of Cu arises when the concentration of 1, 2, 4-triazole is 2 mM. When the concentration goes up from 2 to 10 mM, or decreases from 2 to 0 mM, the corrosion rate continuously increases. But it remains almost stable when the concentration is higher than 10 mM. Different from BTA, 1, 2, 4-triazole exhibits good galvanic corrosion inhibition at all concentrations, indicating it a safe corrosion inhibitor.

CIE is defined to quantitatively evaluate the efficiency of galvanic corrosion inhibition, as is shown in Eq. 6.1:

$$CIE(\%) = (1 - i_n/i_o) \cdot 100 \tag{6.1}$$

where i_n is the corrosion current density with inhibitors, and i_o is that without inhibitors. A higher *CIE* means better galvanic corrosion inhibition resulting from the inhibitors. In the KIO_4-based solution, i_o is 1.6 μA/cm^2. Table 6.1 is the calculated *CIE* according to Figs. 6.5 and 6.6. It is clear that BTA shows good Cu corrosion inhibition when the content is over 1 mM. The *CIE* is up to 79.6% when the concentration is 10 mM. However, excessive BTA added in polishing slurry will result in an unsatisfactory low material removal rate, thus 5 mM BTA is chosen for the following experiments and analysis considering the optimal dosage of inhibitor during CMP (Chen and Hsieh 2010). The *CIEs* are 69.4 and 59.7 for BTA and 1, 2, 4-triazole, respectively, which indicate that both of them have good galvanic corrosion inhibition of Cu.

6.4 Solution/Metal Interface Characterization

Wettability indicates the spreading ability of a solution on surfaces. A droplet of the solutions on a smooth metal surface will stay at a certain angle, namely contact angle θ. The solid-gas interface free energy γ_{SG}, solid-liquid interface free energy

γ_{SL}, surface tension of the solution γ_{LG}, and θ follow Young's Equation, as shown in Eq. 6.2. Generally, a smaller θ means a better wetting ability of the solution on metals. In Eq. 6.2, γ_{SL} could be used to evaluate the solution/metal interface properties. With regard to a certain system, γ_{SG} stays the same, surface tension and contact angle could be directly measured by experiments, and therefore the changes of γ_{SL} are in line with $\gamma_{LG}\cos\theta$, which could reflect the solution/metal interface changes.

$$\gamma_{SG} - \gamma_{SL} = \gamma_{LG}\cos\theta \tag{6.2}$$

Table 6.2 shows the surface tension of the solutions. For better comparison, 0.5 mM anionic surfactant sodium dodecyl sulfate (SDS) was added to the KIO_4 solution. It could be found that only SDS could significantly reduce the surface tension of the KIO_4 solution. The addition of BTA and 1, 2, 4-triazole has negligible influences on surface tensions of the solutions, which is not considered in the γ_{LG} changes.

Figures 6.8 and 6.9 are the results of the contact angle experiments on Cu and Ru surfaces. In general, the contact angles on Ru are bigger than that on Cu, implying that the solutions have better wetting ability on Cu. The addition of inhibitors (both BTA and1, 2, 4-triazole) could more or less increase the contact angles of the KIO_4 solution. Especially, BTA-contained solution could increase the

Table 6.2 The surface tension of different solutions

Solutions	KIO_4	KIO_4 + 2 mM 1, 2, 4-triazole	KIO_4 + 5 mM BTA	KIO_4 + 0.5 mM SDS
Surface tension (mN/m)	74.215 (0.052)	74.255 (0.102)	73.765 (0.110)	38.78 (1.021)

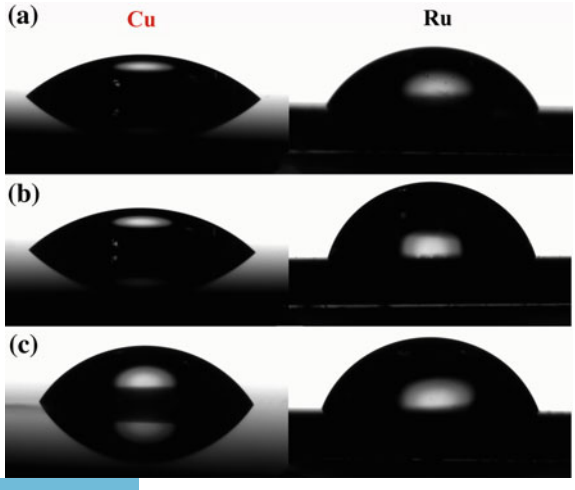

Fig. 6.8 The optical images of the micro-droplets on Cu and Ru surfaces: **a** 0.5% KIO_4; **b** 0.5% KIO_4 + 2 mM 1, 2, 4-triazole; **c** 0.5% KIO_4 + 5 mM BTA

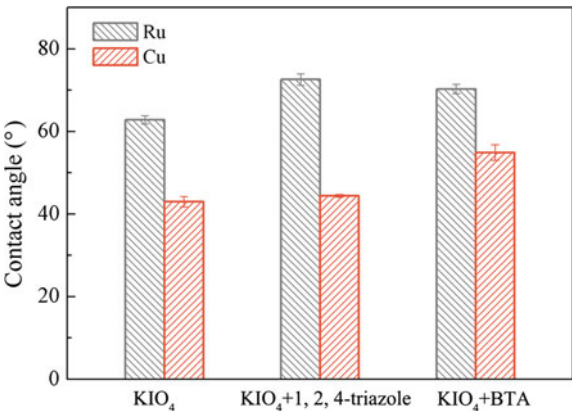

Fig. 6.9 The contact angles of the solutions on metal surfaces

contact angle of KIO_4 on Cu from 43.0° to 54.9°, while 1, 2, 4-triazole barely works on this. The condition is different for Ru. On Ru surface, both BTA and 1, 2, 4-triazole could obviously increase the contact angles, especially for 1, 2, 4-triazole, the addition of which could increase the contact angle from 62.8° to 72.6°. According to Eq. 6.2, when γ_{LG} remains almost unchanged, the changes of contact angles on a given metal surface signifies the solution/metal interface changes. In corrosive solutions with inhibitors, the interface changes often result from the metal surface passivation, metal dissolution and oxides growth. So it follows, different inhibitors play diverse roles for the corrosion inhibition of Cu and Ru. For Cu, only the addition of BTA could significantly change the surface film properties, i.e., forming Cu-BTA complex or so, while for Ru both BTA and 1, 2, 4-triazole have non-ignorable effects on the solution/Ru interface changes.

The results stated above are further supported by the electrochemical *OCP* experiments. In Fig. 6.10, the OCPs of Ru are dramatically higher than those of Cu, which means a higher chemical inertness of Ru as the cathode of the Cu/Ru

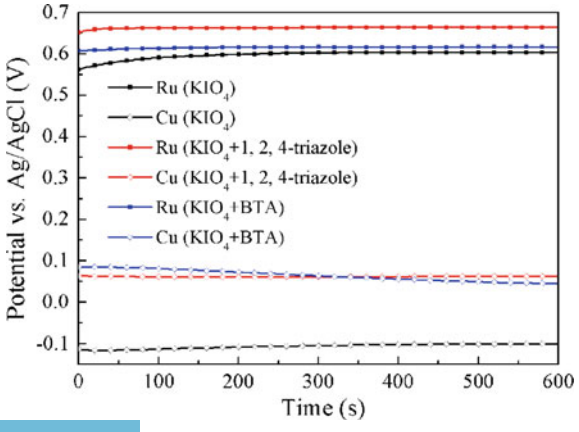

Fig. 6.10 The open circuit potentials of Cu and Ru in different KIO_4 solutions

galvanic couple in KIO_4-based solutions. When inhibitors are added into the KIO_4 solution, the *OCPs* of Cu and Ru are more or less elevated, indicating effective corrosion inhibition. The *OCP* of Ru obviously increases in 1, 2, 4-triazole-contained solution, which coincides well with the contact angle experiments. It is reported that the OCP differences (ΔE_{ocp}) between Cu and Ru could be used to predict the tendency of galvanic corrosion. ΔE_{ocp} is 0.704 V in KIO_4 solution, and it further decreases to 0.601 or 0.572 V after 1, 2, 4-triazole or BTA are added into the solution, respectively. A minimal ΔE_{ocp} is obtained when the solution contains BTA as inhibitor, and the *CIE* is the maximal (69.4) in this case, as has been stated in Sect. 6.3.

6.5 The Corrosion Inhibition Mechanism

Figure 6.11 shows the solutions after galvanic corrosion current measurements. It is obvious that when solutions contains BTA and 1, 2, 4-triazole, the color of the solutions is almost transparent, while that for the KIO_4 solution is light yellow, which results from a small quantity of dissolved I_2. This phenomenon could further elucidate that BTA and 1, 2, 4-triazole are effective galvanic corrosion inhibitors for Cu/Ru couple, which could effectively hinder the corrosion process of Cu and thereby suppress the formation of I_2.

Because of the positions of the donors in the ring, the inhibitors (both BTA and 1, 2, 4-triazole) seem to process the possibility of linking transition metal ions together. Therefore, there will form a protective barrier layer on Cu surface, which prevents Cu from further corrosion (Matjaž and Ingrid 2010). However, the

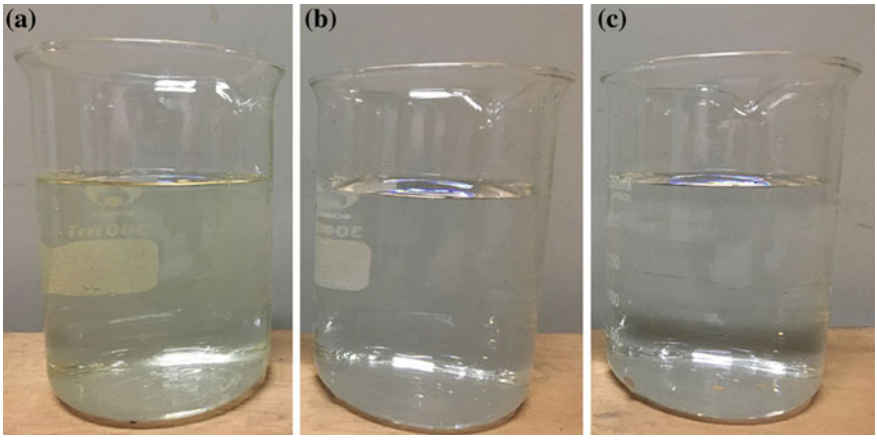

Fig. 6.11 The solutions after Cu/Ru galvanic corrosion current measurements: **a** 0.5% KIO_4; **b** 0.5% KIO_4 + 5 mM BTA; **c** 0.5% KIO_4 + 2 mM 1, 2, 4-triazole

chemisorption and Cu-inhibitor complex structure are diverse when different inhibitors are used, thus various corrosion inhibition performances are generated.

It has been reported that in BTA contained solutions, there forms multilayer films on Cu (Roberts 1974; Törnkvist et al. 1988; Friedrich et al. 2005). The first layer is the Cu oxide layer. The nature of the Cu oxide under-layer will definitely influence the adsorption of BTA. The adsorption is fast on Cu_2O but slow on Cu or CuO, and therefore the oxidation of Cu (forming Cu_2O on Cu surface) will help with the adsorption of BTA. The second layer is the chemisorbed BTA layer. For this layer, BTA is neither lying on nor perpendicular to the Cu, but it is somehow tilted in between these two orientations, linking Cu_2O through the nitrogen lone pairs (Poling 1970; Rubim et al. 1983). The third layer is Cu(I)BTA complex. Parallel stacking of BTA molecules could form chain-like structures, with the molecular plane perpendicular or slightly tilted with respect to the Cu surface (Matjaž and Ingrid 2010). The adsorption mechanism of BTA on Cu is schematically shown in Fig. 6.12a, which forms chain structure passivation film on Cu surface (Ling et al. 1995). It should be noted that due to the ion movement, there are no clear boundaries for the multilayers. When the concentration of BTA is high, the film stack is Cu/Cu_2O/Cu(I)BTA complex, which is complete and tight and has higher inhibition efficiency (Chen et al. 1998). Conversely when the concentration of BTA is low, the surface consists of Cu/Cu_2O/Cu(I)BTA-CuO. The presence of CuO will interfere with the formation of the tight network, and therefore may result in pitting problems when the concentration of BTA is lower. The sketch of the multilayer structures on Cu at different BTA concentrations is shown in Fig. 6.13, which could explain the higher galvanic corrosion current density when 0.5 mM BTA is added into KIO_4 solution.

With regard to 1, 2, 4-triazole, it is recognized that the N_2, N_4 bridging mode will lead to the two-dimensional, layered compounds formed on transition metals

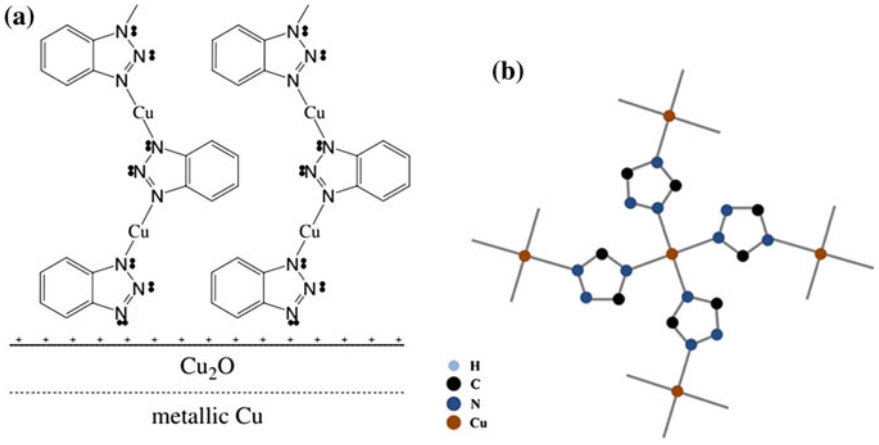

Fig. 6.12 **a** The chain structure of Cu(I)BTA complex on Cu; **b** the net structure of Cu-1, 2, 4-triazole complex

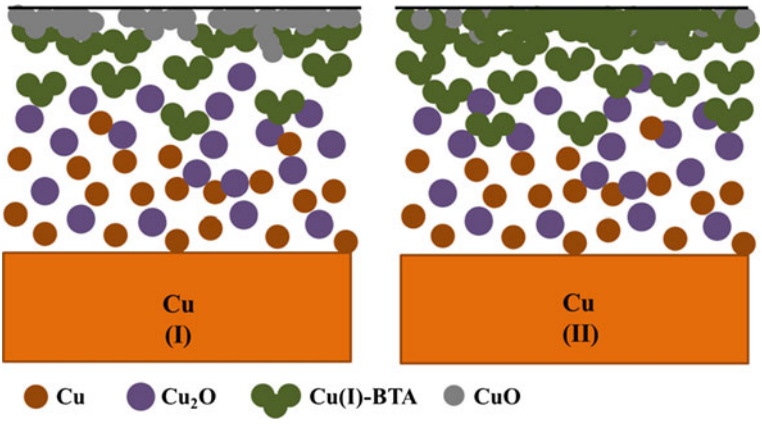

Fig. 6.13 A scheme of the surface film structures of Cu immersed in KIO_4 solutions with BTA as corrosion inhibitor: **I** low BTA concentrations; **II** high BTA concentrations

(Haasnoot 2000). Quite different from BTA, these compounds are net structure with Cu ions, each connected to four neighbors by bridging triazoles, as is shown in Fig. 6.12b. The mechanism of the complex formation could explain the decreased *CIE* when the concentration of 1, 2, 4-triazole increases from 2 mM. When the concentration of 1, 2, 4-triazole is higher than 2 mM, the coverage of 1, 2, 4-triazole on Cu surface is saturated. Excessive 1, 2, 4-triazole cannot find adsorption sites, causing tiny disturbance of the surface layer. The protective layer is not stable enough so that desorption and dissolution of the surface layer will happen, which will result in a decrease of the corrosion inhibition efficiency.

Table 6.3 compares BTA and 1, 2, 4-triazole as galvanic corrosion inhibitors for the Cu/Ru couple. As aforementioned, the complex formed between BTA and Cu is chain structure, while that for 1, 2, 4-triazole is a net structure. BTA is a dangerous inhibitor, the low concentration of which will cause pitting corrosion instead. However for 1, 2, 4-triazole, it shows good corrosion inhibition properties at all concentrations, indicating that 1, 2, 4-triazole is a safe corrosion inhibitor.

Table 6.3 The comparisons between BTA and 1, 2, 4-triazole as galvanic corrosion inhibitors for Cu/Ru couple

	BTA	1, 2, 4-triazole
Polymer structure formed with Cu	Chain structure	Net structure
Safety as corrosion inhibitor	Pitting at low concentrations (dangerous)	Safe
Efficiency of galvanic corrosion inhibition	Increase with concentration (≥ 5 mM)	Reach the maximum at 2 mM

6.6 Conclusions

Considering the unsolved Cu/Ru galvanic corrosion issue during the CMP process using Ru as a new barrier layer material, this chapter investigated the galvanic corrosion inhibition efficiency and mechanism of BTA and 1, 2, 4-triazole as corrosion inhibitors. In KIO_4-based solutions, the galvanic corrosion current densities of Cu/Ru couple were directly measured, based on which the corrosion inhibition efficiencies were calculated. On this basis, corrosion inhibition mechanisms for BTA and 1, 2, 4-triazole were proposed, respectively. Results show that when KIO_4 is used as the oxidant, galvanic corrosion is quite severe. Both BTA and 1, 2, 4-triazole are effective galvanic corrosion inhibitors for Cu, with corrosion inhibition efficiency up to 69.4 and 59.7, respectively. The corrosion inhibition of inhibitors results from the formation of protective surface layers on Cu. For BTA, a tight and complete $Cu/Cu_2O/Cu(I)BTA$ multilayer structure is formed when the concentration of BTA is high. However, low dosage (<0.5 mM) of BTA should be avoided because accelerated galvanic corrosion of Cu could happen in this case. With regard to 1, 2, 4-triazole, the surface protective layer has a net structure, and the optimal dosage is 2 mM. Excessive 1, 2, 4-triazole will inversely reduce the stability of the surface film, as well as the corrosion inhibition efficiency of Cu.

References

Brusic V, Frisch MA, Eldridge BN, Novak FP, Kaufman FB, Rush BM, Frankel GS (1991) Copper corrosion with and without inhibitors. J Electrochem Soc 138(8):2253–2259

Chen CCA, Hsieh CH (2010) Effect of inhibiter concentration on Cu CMP slurry analyzed by a Cu-ECMP system. ECS Trans 33(10):107–113

Chen JH, Lin ZC, Chen S, Nie LH, Yao SZ (1998) An XPS and BAW sensor study of the structure and real-time growth behaviour of a complex surface film on copper in sodium chloride solutions (pH = 9), containing a low concentration of benzotriazole. Electrochim Acta 43(3–4): 265–274

Copson HR (1943) Distribution of galvanic corrosion. Trans Electrochem Soci 84(1):71–82

Costa SFLA, Agostinho SML, Rubim JC (1990) Spectroelectrochemical study of passive films formed on brass electrodes in 0.5 m H_2SO_4 aqueous solutions containing benzotriazole (BTAH). J Electroanal Chem 295(1–2):203–214

Deshpande S, Kuiry SC, Klimov M, Obeng Y, Seal S (2004) Chemical mechanical planarization of copper: role of oxidants and inhibitors. J Electrochem Soc 151(11):G788–G794

Friedrich M, Gálvez-Ruiz JC, Klapötke TM, Mayer P, Weber B, Weigand JJ (2005) BTA copper complexes. Inorg Chem 44(22):8044–8052

Goonetilleke PC, Roy D (2008) Relative roles of acetic acid, dodecyl sulfate and benzotriazole in chemical mechanical and electrochemical mechanical planarization of copper. Appl Surf Sci 254(9):2696–2707

Haasnoot JG (2000) Mononuclear, oligonuclear and polynuclear metal coordination compounds with 1, 2, 4-triazole derivatives as ligands. Coordin Chem Rev 200–202:131–185

Jiang L, He Y, Li Y, Luo J (2014) Effect of ionic strength on ruthenium CMP in H_2O_2-based slurries. Appl Surf Sci 317(30):332–337

Ling Y, Guan Y, Han KN (1995) Corrosion inhibition of copper with benzotriazole and other organic surfactants. Corrosion 51(5):367–375

Matjaž F, Ingrid M (2010) Inhibition of copper corrosion by 1, 2, 3-benzotriazole: A review. Corros Sci 52(9):2737–2749

Peethala BC, Babu SV (2011) Ruthenium polishing using potassium periodate as the oxidizer and silica abrasives. J Electrochem Soc 158(3):H271–H276

Poling GW (1970) Reflection infra-red studies of films formed by benzotriazole on Cu. Corros Sci 10(5):359–370

Roberts RF (1974) X-ray photoelectron spectroscopic characterization of copper oxide surfaces treated with benzotriazole. J Electron Spectrosc Relat Phenom 4(4):273–291

Rubim J, Gutz IGR, Sala O, Orville-Thomas WJ (1983) Surface enhanced Raman spectra of benzotriazole adsorbed on a copper electrode. J Mol Struct 100:571–583

Sherif ESM, Erasmus RM, Comins JD (2007) Effects of 3-amino-1, 2, 4-triazole on the inhibition of copper corrosion in acidic chloride solutions. J Colloid Interface Sci 311(1):144–151

Törnkvist C, Thierry D, Bergman J, Liedberg B, Leygraf C (1988) Methyl substitution in benzotriazole and its influence on surface structure and corrosion inhibition. J Electrochem Soc 136(1):58–64

Tseng W, Kuo P, Liao C, Lu R, Lin J (2001) Novel polymeric surfactants for improving chemical mechanical polishing performance of silicon oxide. Electrochem Solid-State Lett 4(5): G42–G45

Walker R (1975) Triazole, benzotriazole And naphthotriazole as corrosion inhibitors for copper. Corrosion 31(3):97–100

Zhu Y, Free ML (2015) Experimental investigation and modeling of the performance of pure and mixed surfactant inhibitors: partitioning and distribution in water-oil environments. J Electrochem Soc 162(14):70–71

Chapter 7
Synergetic Effect of Potassium Molybdate and Benzotriazole on the CMP of Ru and Cu in KIO_4-Based Slurry

7.1 Experimental

Ru and Cu disks (99.99% purity, thickness and diameter equal to 1 mm and 2 inch, respectively) were used for polishing and static etch experiments. The CMP experiments were carried out at a down pressure of 4 psi with an IC1010/Suba-IV composite pad with a K-type groove (purchased from Dow Electronic Materials, USA). A CETR CP-4 bench-top polisher was used with platen/carrier speed of 100/100 rpm and a slurry flow rate of 100 mL/min. The slurry contained Nexil 85 k-40 colloidal silica abrasives (purchased from Nyacol) and KOH/H_2SO_4 as a pH adjustor. In order to monitor the stability of the slurry, a laser zeta potential analyzer (Malvern Nano ZS90) was used to measure the zeta potential of colloidal silica in KIO_4-based solutions. The MRRs were measured using the weight-loss method after polishing for 1 min. Before the experiments, conditioning was carried out for 10 min. After each polishing, a pad ex situ conditioning was carried out for 45 s. The static etch experiments were performed in glass beakers containing 250 mL solution without abrasive particles. The surface of the disk was abraded on 2000# SiC abrasive paper, cleaned in DI water using ultrasonic agitation, and dried in N_2 successively. The immersing time was 30 min with the solution slightly stirred. The static etch rate (SER) was calculated by weight loss. SER, MRR and zeta potentials were calculated as an average obtained from three different experimental runs.

Potentiodynamic polarization tests were carried out to investigate the electrochemical properties of Ru and Cu. A M273A EG&G potentiostat (Princeton Applied Research) with three electrodes was used, i.e., a platinum electrode, an Ag/AgCl (3.5 M) electrode, and a Cu or Ru disk (diameter of 5 mm), which were employed as the counter electrode, reference electrode, and working electrode, respectively. Before each experiment, the electrode was abraded on 2000# SiC

J. Cheng, *Research on Chemical Mechanical Polishing Mechanism of Novel Diffusion Barrier Ru for Cu Interconnect*, Springer Theses,
DOI 10.1007/978-981-10-6165-3_7

abrasive paper, rinsed with DI water, and dried in N_2 gas successively. The specimens were immersed into solutions without silica abrasives to avoid unnecessary adsorption on the surface. The scan rate was 1 mV/s. Before each scanning, the working electrode was dipped into the solution for 600 s to measure the OCP.

X-ray photoelectron spectroscopy (XPS-250XI) analysis was carried out to characterize the chemical properties of Ru and Cu surfaces. For sample preparation, the Cu and Ru disks (diameter and thickness equal to 5 and 2 mm, respectively) were abraded on 2000# SiC abrasive paper, rinsed with DI water, and dried in N_2 gas. The disks were then immersed in 20 mL solution (without abrasives) for 10 min at room temperature. XPS peaks of Cu 2p3/2, Ru 3d5/2, Ru 3d3/2 and O1 s were analyzed, and the surface products of Cu and Ru were obtained by peak fitting.

7.2 Calculation of Galvanic Corrosion

In order to solve the issues related to corrosion and achieve good material removal selectivity between Ru and Cu, inhibitors, such as BTA, are often added in the slurry. However, in KIO_4-based slurry, BTA passivation film is not sufficiently compact, and consequently, the *MRR* of Cu sharply increases because of complexation occurring in the presence of BTA (Jiang et al. 2014). Thus, to improve the passivation effect, this issue should be addressed. Nontoxic molybdate salts, such as K_2MoO_4, which are stable in both strongly acidic and alkaline solutions, have been extensively used in combination with BTA to prevent Cu corrosion (Robertson 1951; Zhang et al. 2009). In this section, the galvanic corrosion of Cu is calculated based on electrochemical experimental results.

The electrochemical equilibrium potential of Ru/Ru^{2+} is higher than that of Cu/Cu^{2+}, i.e., Cu corrosion is promoted in the Cu-Ru coupling. The accelerated corrosion effect (γ) of Cu can be expressed as:

$$\gamma = \frac{I_{\mathrm{a1}}}{I_{\mathrm{corr1}}} \tag{7.1}$$

where I_{a1} is the anodic dissolution current density of Cu after contact, and I_{corr1} is the corrosion current density of Cu before coupling. The anodic reactions mostly take place on the Cu surface, while the cathodic reactions preferentially occur on the Ru surface. Taken this into account, γ can be described as:

$$\gamma = \frac{E_{\mathrm{corr2}} - E_{\mathrm{corr1}}}{\beta_{\mathrm{a1}} + \beta_{c2}} + \frac{\beta_{\mathrm{c2}}}{\beta_{a1} + \beta_{c2}} \ln\left(\frac{I_{\mathrm{corr2}}}{I_{\mathrm{corr1}}}\right) + \frac{\beta_{\mathrm{c2}}}{\beta_{\mathrm{a1}} + \beta_{\mathrm{c2}}} \ln\left(\frac{A_2}{A_1}\right) \tag{7.2}$$

where E_{corr2} and E_{corr1} are the corrosion potentials of Cu and Ru before coupling, respectively; β_{a1} and β_{c2} are the slopes of the anodic and cathodic branch natural logarithm in the Tafel plots of Cu and Ru, respectively; I_{corr2} is the corrosion current density of Ru before coupling, and A_1 and A_2 are the contact areas exposed in solution of Cu and Ru, respectively. These can be estimated from the actual conditions. E_{corr} and I_{corr}, combined with β, can be calculated from the potentiodynamic polarization plots.

For Cu interconnects, given that the feature size is scaling down, the thickness of the barrier layer has to shrink. A_2/A_1 can be then simplified as:

$$\frac{A_2}{A_1} = \frac{2W_{\mathrm{Ru}} \cdot L}{W_{\mathrm{Cu}} \cdot L} = \frac{2W_{\mathrm{Ru}}}{W_{\mathrm{Cu}}} \tag{7.3}$$

where W_{Ru} is the thickness of the barrier layer, W_{Cu} is the width of the Cu wiring and L is the length of wiring structure. The results of our calculations (based on the 2012 International Technology Roadmap for Semiconductors, ITRS-2012) show that the ratio of A_2/A_1 increases when the feature size is reduced (Table 7.1). Furthermore, γ increases with A_2/A_1 when other parameters are kept unchanged (Eq. 7.2), which suggests that the galvanic corrosion of Cu may worsen as a result of the scaling technology node.

Previous studies show that the poor solubility in water of KIO_4 can be increased by adding KOH (Peethala and Babu 2011). Taking into account that the solubility of KIO_4 at pH = 9 is $\sim$0.36 M, 0.015 M KIO_4 is added into the solutions. Figure 7.1 shows the potentiodynamic polarization curves of Cu and Ru in KIO_4 solutions. The results of the calculation of E_{corr}, I_{corr}, and β are listed in Table 7.2. These are used, together with A_2/A_1 equal to 0.179, in the following calculations. γ and I_{a1} are calculated based on the parameters presented in Table 7.2. The results (Table 7.3) show that after the addition of BTA in the KIO_4-based solution, γ decreases from 53.5 to 34.8. In the presence of 5 mM BTA and 20 mM K_2MoO_4, γ further decreases to 16.4, and the Cu dissolution current density I_{a1} is also obviously reduced (to 7.2 μA cm^2), confirming that the galvanic corrosion of Cu is mitigated by the addition of BTA and K_2MoO_4.

When the solution contains only KIO_4, the corrosion potential difference (ΔE_{corr}) is 0.662 V, in line with the studies of B. C. Peethala's investigation. Moreover, after a two-step addition of BTA and K_2MoO_4, the corrosion potential of Cu continuously increases. However, ΔE_{corr} decreases after the addition of K_2MoO_4 in the solution containing BTA. This is the most desirable scenario. ΔE_{corr} in Solution (3) (0.484 V) is smaller than that in Solution (2). Furthermore, γ is reduced because of the decrease of ΔE_{corr}, as a result of which the galvanic corrosion of Cu is weakened. This confirms that ΔE_{corr} is an important indicator of galvanic corrosion.

Table 7.1 Calculation of A_2/A_1 based on ITRS-2012

MPU/ASIC 1/2 Pitch (nm)	31.82	26.76	23.84	21.24	18.92	16.86	15.02	13.38	11.92	10.62
Barrier thickness (nm)	2.6	2.4	2.1	1.9	1.7	1.5	1.3	1.2	1.1	1.0
A_2/A_1	0.163	0.179	0.176	0.179	0.179	0.178	0.173	0.179	0.185	0.188

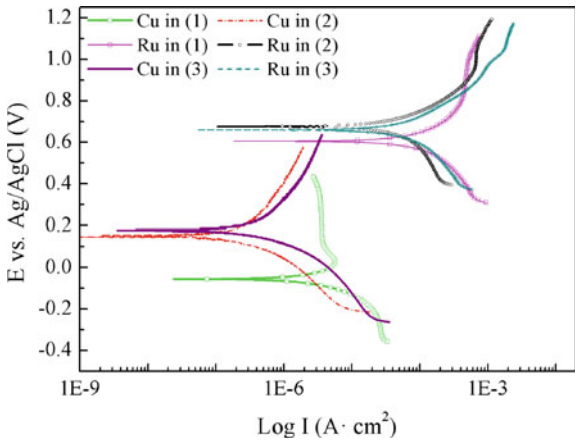

Fig. 7.1 Potentiodynamic polarization plots of Cu and Ru at pH = 9 in solutions of (1) 0.015 M KIO_4; (2) 0.015 M KIO_4 and 5 mM BTA; (3) 0.015 M KIO_4, 5 mM BTA, and 20 mM K_2MoO_4

Table 7.2 The calculation of E_{corr}, I_{corr}, and β from Fig. 7.1

	E_{corr} versus Ag/Cl (V)		I_{corr} (μA cm^2)			
Solution	Cu	Ru	Cu	Ru	β_{a1} (V)	β_{c2} (V)
0.015 M KIO_4	−0.056	0.606	3.660	88.1	0.173	0.113
0.015 M KIO_4 + 5 mM BTA	0.154	0.676	0.182	38.1	0.118	0.129
0.015 M KIO_4 + 5 mM BTA + 20 mM K_2MoO_4	0.1765	0.660	0.314	45.2	0.125	0.115

Table 7.3 The calculation of γ and I_{a1}

Solution	I_{a1} (μA cm^2)	γ
0.015 M KIO_4	250.9	53.5
0.015 M KIO_4 + 5 mM BTA	7.7	34.8
0.015 M KIO_4 + 5 mM BTA + 20 mM K_2MoO_4	7.2	16.4

7.3 Synergistic Effect of BTA and K_2MoO_4 on Corrosion Inhibition

Several anodic (such as Ethylene Diamine Tetraacetic Acid and Polyacrylamide, M.W. 10 k) and cathodic inhibitors (such as AA) were suggested to mitigate corrosion (Cui et al. 2013; Otmačić and Stupnišek-Lisac 2003). In this work, however, cathodic inhibitors like AA are avoided, because they may react with the oxidizer KIO_4. Because the corrosion potentials of both Cu and Ru increase in the presence of BTA and K_2MoO_4, the combination of these compounds acts as an anodic

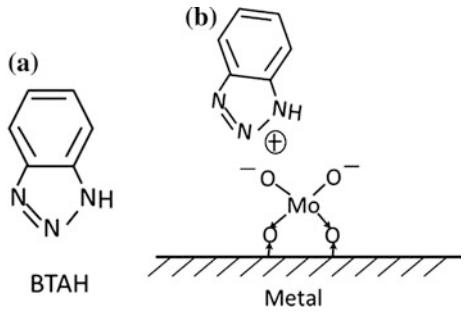

Fig. 7.2 **a** Molecular structure of BTAH and **b** schematic plot of the adsorption of BTAH on a metal surface

inhibitor in KIO_4-based solution. Based on previous studies that suggested molybdate as a corrosion inhibitor, some conjectures about the inhibition mechanism on Cu and Ru can be made. Firstly, MoO_4^{2-} is an active oxygen acid ion, and it may easily be adsorbed on the surface of metals and this may modify the surface structure in the region between the metal and the electrolyte, causing an increase in the activation energy of the electrode reaction. With the absorption of MoO_4^{2-}, the ion-dipole would increase the adsorption stability of BTAH (Fig. 7.2), which is the most likely form of BTA in alkaline solutions (Tromans and Sun 1991), thus forming a three-dimensional network complex film on the protected metal surface (Robertson 1951). Secondly, insoluble molybdate salts could form on the metal surface and deposit into the porous BTA inhibition film. As a result, this could reinforce the compactness of the passivation film (Ramirez Arteaga et al. 2011). Finally, it has been reported that the cuprous oxide is essential for the stable adsorption of BTA on the Cu surface (Vogt et al. 1998). As a result, K_2MoO_4 does not directly participate in passivation of the metal, but supports the formation of Cu_2O, which could enhance the adsorption of the BTA film (Zhang et al. 2009).

Figure 7.3 shows the XPS results of the Cu surface immersed in different solutions. Figure 7.3a, c, e demonstrate the Cu 2p spectra. From these data, it is clear that before the addition of BTA and K_2MoO_4, the surface of Cu is highly oxidized to a cupric state, indicating severe corrosion of the Cu surface (Ramirez Arteaga et al. 2011). After the addition of BTA, the surface is covered with cuprous oxide and a small amount of Cu-BTA (Chadwick and Hashemi 1978). This is because BTA adsorbs on the Cu surface in the form of a chemisorbed layer Cu: BTA (ads) in alkaline solutions (Xue et al. 1991). In contrast, the complex Cu-BTA is likely to form in acid solutions (Yu et al. 2003; Sayed et al. 2003). In the presence of BTA and K_2MoO_4, the cupric oxide disappears, indicating that further corrosion inhibition may occur in solution. It should also be remarked that Cu-BTA disappears (Fig. 7.3e) and this may be due to the adsorption of MoO_4^{2-} on the Cu surface. In contrast, the adsorbed MoO_4^{2-} could increase the activation energy of Cu oxidation reaction, as shown in Fig. 7.4, where the OCP values of Cu and Ru in different solutions are displayed. In Solution (3), the initial OCP value of Cu is higher than that in Solution (2). This confirms the increase of the activation energy of the Cu/Cu^{2+} reaction. On the other hand, the adsorbed MoO_4^{2-} could support the

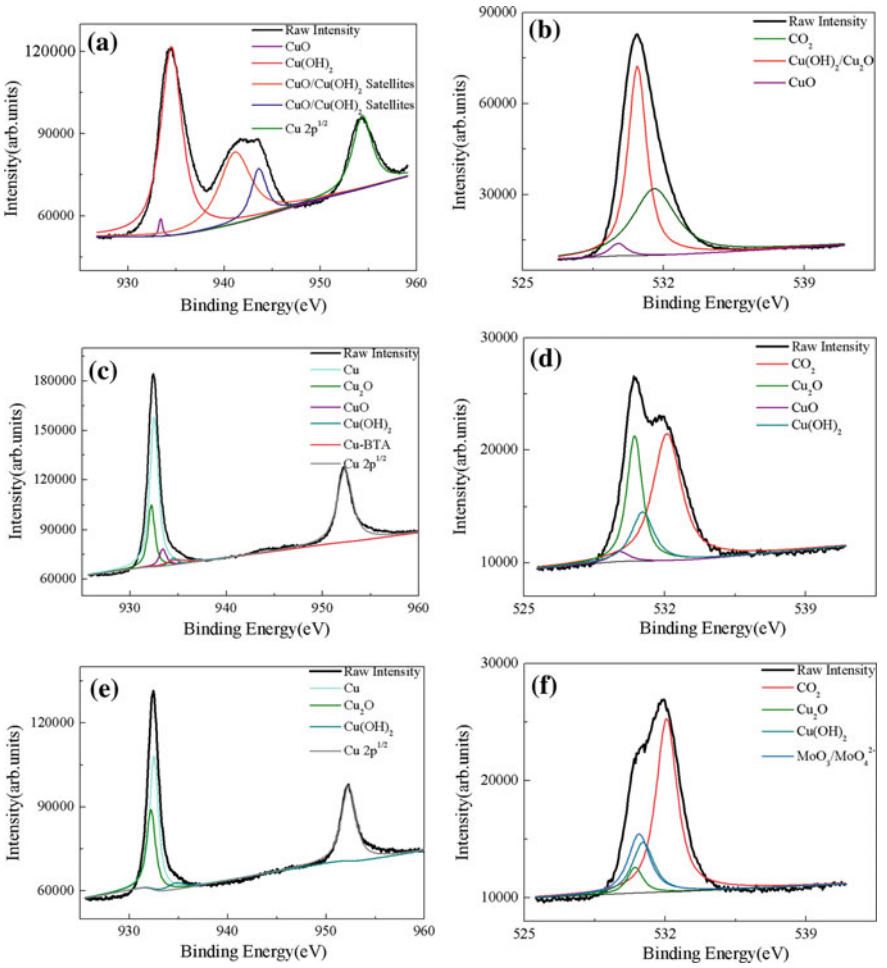

Fig. 7.3 XPS of treated Cu surfaces in different solutions at pH = 9 **a** Cu 2d spectra in 0.015 M KIO_4; **b** O1 s spectra in 0.015 M KIO_4; **c** Cu 2d spectra in a solution containing 0.015 M KIO_4 and 5 mM BTA; **d** O1 s spectra in a solution containing 0.015 M KIO_4 and 5 mM BTA; **e** Cu 2d spectra in a solution containing 0.015 M KIO_4, 5 mM BTA and 20 mM K_2MoO_4; **f** O1 s spectra in a solution containing 0.015 M KIO_4, 5 mM BTA and 20 mM K_2MoO_4

stable adsorption of BTA, forming passivation film with a three-dimensional network. Data displayed in Fig. 7.3f suggest that MoO_4^{2-} is likely to be in the insoluble $CuMoO_4$ form, because MoO_3 can only exist when the pH is at the isoelectric point (pH = 0.9) (Walker and Wilcox 2008). There have been several investigations about synergistic inhibition effect between BTA and other additives (such as non-ionic surfactant) during Cu CMP process (Hong et al. 2007; Pandija et al. 2009). The research results show that the compound BTA inhibitors have better passivation properties because of the more compact passivation film formed

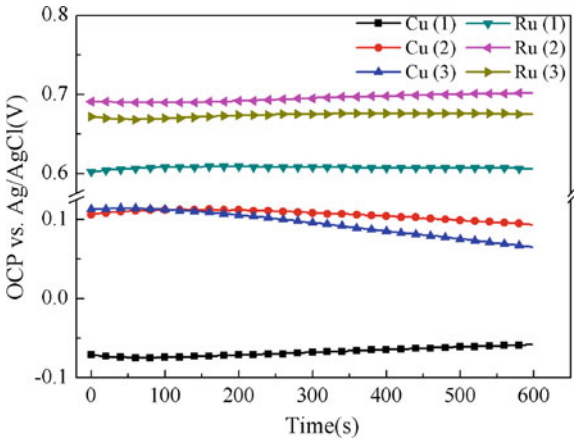

Fig. 7.4 OCP measurements of Cu and Ru at pH = 9 in a solution of (1) 0.015 M KIO_4; (2) 0.015 M KIO_4 and 5 mM BTA; (3) 0.015 M KIO_4, 5 mM BTA, and 20 mM K_2MoO_4

on Cu surface. In the experiments, the insoluble $CuMoO_4$ could thus deposit into the gaps of the BTA film, enhancing the compactness of the passivation film. In addition, XPS as a semi-quantitative analysis method could be used to analyze the amount of chemical compounds on the surface to some extent. However, as shown in Fig. 7.3b, d, f, no evident increase in Cu_2O content is detected, providing no proof of the third conjecture mentioned above (McIntyre and Cook 1975; Hernandez et al. 2001).

Investigations about the BTA passivation mechanism on Ru are rare. Figure 7.5a–c show XPS results of Ru 3d spectra on the Ru surface immersed in different KIO_4 solutions. According to the data displayed in Fig. 7.5b, a shift of binding energy at about 279 eV occurs (to compare with those in Fig. 7.5a, c). Ru metallic binding energy for 3d5/2 occurs at 280.2 eV. The binding energies for RuO_2 and RuO_3 are 281.0 and 282.5 eV, respectively (Cui et al. 2012; Kötz et al. 1983). Therefore, such a clear binding energy shift may be due to the interaction between Ru and BTA.

Previous studies show that RuO_3 may be incorporated into the RuO_2 layer to form an inhomogeneous layer on the metal surface, thus increasing the chemical corrosion and the MRR during Ru polishing. As a consequence, the relative content of RuO_3 on the surface has been suggested as an important indicator of the passivation of the inhibitor. Figure 7.5d–f show the O1 s spectra of the Ru surface in different solutions. The binding energies for RuO_2 and RuO_3 are 529.2 and 530.7 eV, respectively (Kim et al. 2009). In addition, a considerable amount of CO_2 on the surface with the binding energy of 531 eV is detected (Kötz et al. 1983) and the peak located at 533 eV originates from adsorbed water (Cano et al. 2001). In addition, the peak at around 530 eV in Fig. 7.5e may be due to the formation of Ru $(OH)_3$ (Blouin and Guay 1997). After the addition of BTA in Fig. 7.5e, a clear peak assigned to RuO_3 appears, indicating that BTA alone cannot protect the surface, i.e., corrosion-induced pits may sparsely disperse over the surface. As shown in Fig. 7.5f, after further adding K_2MoO_4 in the solution, the RuO_3 peak can be barely

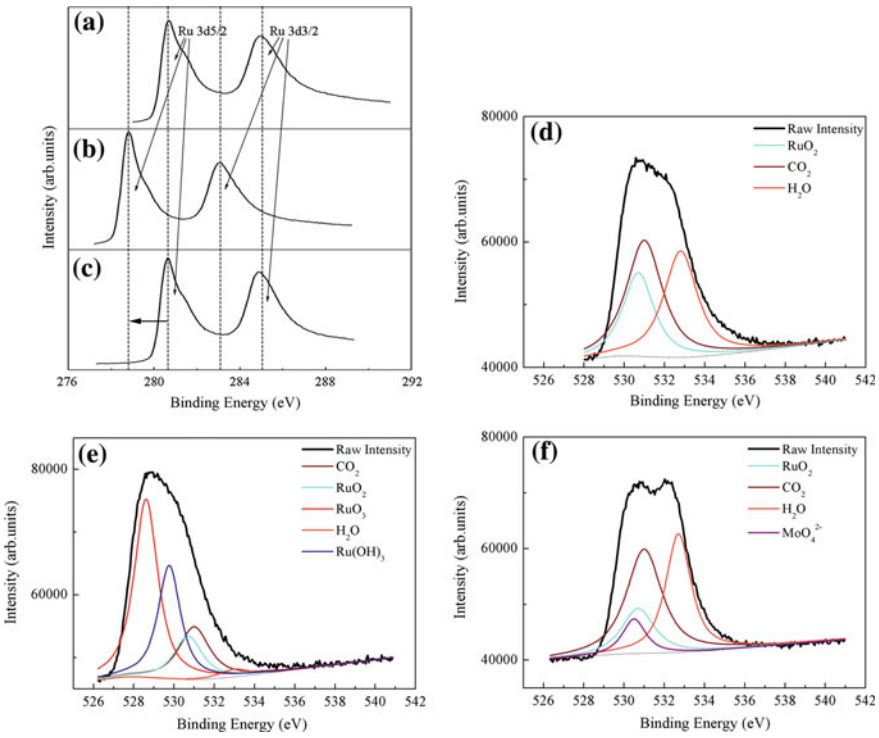

Fig. 7.5 XPS of treated Ru surfaces at pH = 9 in a solution of **a** Ru 3d spectra in 0.015 M KIO_4; **b** Ru 3d spectra in a solution containing 0.015 M KIO_4 and 5 mM BTA; **c** Ru 3d spectra in a solution containing 0.015 M KIO_4, 5 mM BTA and 20 mM K_2MoO_4; **d** O1 s spectra in 0.015 M KIO_4; **e** O1 s spectra in a solution containing 0.015 M KIO_4 and 5 mM BTA; **f** O1 s spectra in a solution containing 0.015 M KIO_4, 5 mM BTA and 20 mM K_2MoO_4

observed. In this respect, not only does the presence of BTA and K_2MoO_4 reduce the corrosion current, but it also contributes to ease pitting problems, improving the quality of the surface. Figure 7.5f also shows a peak related to MoO_4^{2-}, with a binding energy of 530.5 eV (Fleisch and Mains 1982), which may be due to the formation of insoluble ruthenium molybdate. Once formed, ruthenium molybdate could deposit into the gaps of the porous BTA film, thus improving the compactness of the passivation film.

As shown in Fig. 7.4, the OCP of Cu in Solution (3) decreases as a function of time. This may be due to the adsorption of MoO_4^{2-}, which in turn indicates that the adsorbed layer is not integrated and stable enough. In the case of Ru, the OCP is perfectly stable, because of a combination of effects arising from the deposition of the molybdate and the adsorption enhancement of BTA in the presence of K_2MoO_4.

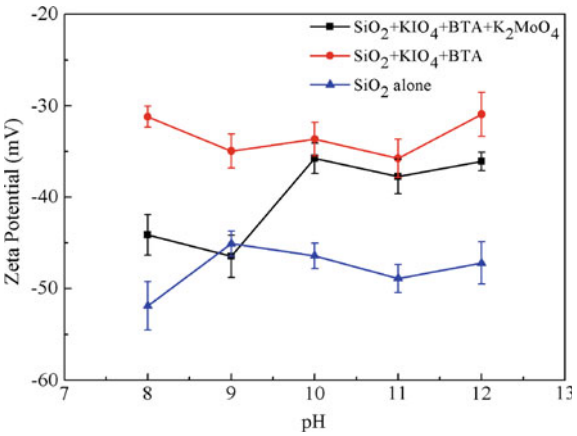

Fig. 7.6 Zeta potential of slurry with 5 wt% colloidal silica as a function of pH. The amount of KIO_4, BTA, and K_2MoO_4 is 0.015 M, 5 mM, and 20 mM, respectively

7.4 Synergistic Effect of BTA and K_2MoO_4 on MRR Selectivity Between Cu and Ru

Figure 7.6 shows the zeta potential of the slurry as a function of pH. The zeta potential of abrasive particles reflects the stability of the slurry, i.e., a highly negative zeta potential is suitable for the preparation of the slurry (Zeng et al. 2012). In an alkaline solution, after the addition of BTA and K_2MoO_4 in KIO_4-based slurry, zeta potential becomes slightly positive, but remains almost unchanged at pH = 9, compared with that of the slurry containing SiO_2 alone. Highly alkaline slurries could result in a high *MRR* of the underneath low-*k* dielectric (Hartmannsgruber et al. 2000). Therefore, the slurry at pH = 9 is the most suitable for our study, and the CMP tests have been carried out at this pH value.

Comparatively a higher *MRR* selectivity between Ru and Cu (slightly larger than 1) is crucial to reduce the dishing defects of the pattern structures generated in the Cu polishing step (Peethala and Babu 2011). Figure 7.7 shows the *MRR*s of Cu and Ru at pH equal to 5.5 and 9 for different slurries. The *MRR* of Cu at pH = 5.5 is larger than that of Ru, and the MRR difference (*ΔMRR*) increases when BTA and BTA-K_2MoO_4 is added. Thus, *ΔMRR* is 48.2, 83.5, and 124.8 nm/min in Slurry (1, 2 and 3), respectively. Such a large *ΔMRR* is, however, the most undesirable condition during polishing. In addition, in acid slurries, toxic-oxidation production of RuO_4 occurs in the slurry, due to its low melting point (Cui et al. 2012). Therefore, it is desirable to carry out the CMP experiments under alkaline conditions. Figure 7.8 displays the surface quality of Cu and Ru after polishing. Because the samples used in the CMP experiments are prepared by powder metallurgy technology, it is difficult to obtain good surface quality after polishing. Therefore, PVD or CVD deposited Cu and Ru films should be used for further CMP experiments.

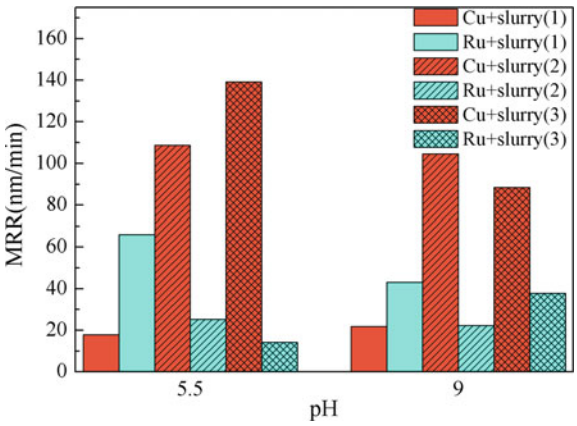

Fig. 7.7 The *MRR* of Cu and Ru in both alkaline and acid slurries with 5wt% SiO_2 abrasives. Slurry contains (1) 0.015 M KIO_4; (2) 0.015 M KIO_4 and 5 mM BTA; (3) 0.015 M KIO_4, 5 mM BTA, and 20 mM K_2MoO_4

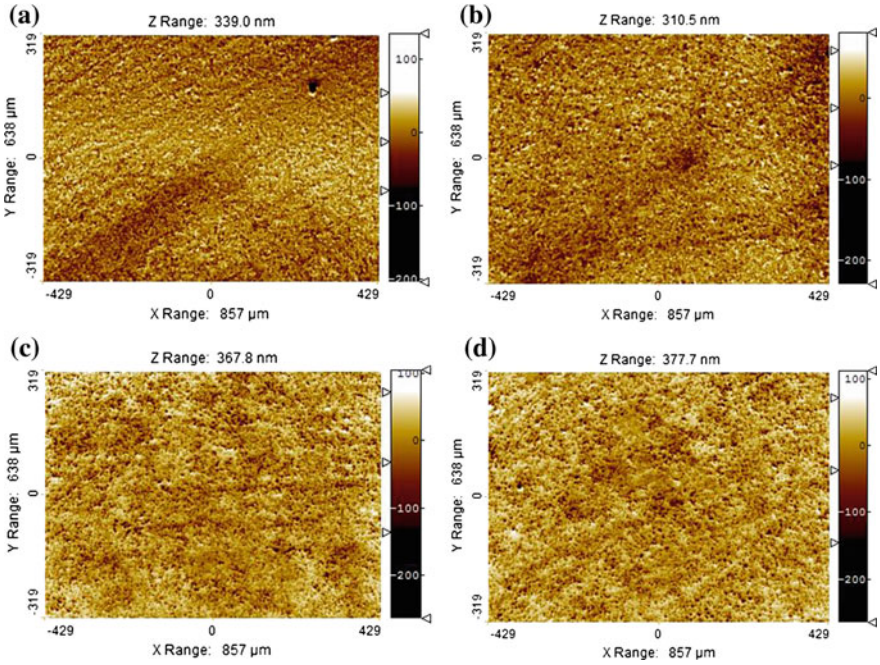

Fig. 7.8 **a–b** Surface quality of Cu after CMP; **c–d** surface quality of Ru after CMP. Slurry contains: **a** and **c** 0.015 M KIO_4 + 5 mM BTA; **b** and **d** 0.015 M KIO_4 + 5 mM BTA + 20 mM K_2MoO_4

Table 7.4 SER of Cu and Ru in solutions containing 0.015 M KIO_4 and 5 mM BTA with different content of K_2MoO_4 (Å/min)

	0 mM K_2MoO_4	1 mM K_2MoO_4	2 mM K_2MoO_4	5 mM K_2MoO_4	10 mM K_2MoO_4	20 mM K_2MoO_4
Cu	1.53	0.75	0.87	0.60	1.01	1.02
Ru	3.99	5.52	12.31	13.30	12.37	12.64

At pH = 9, after the addition of BTA in the KIO_4-based slurry, the *MRR* of Cu increases to 104.5 nm/min, while the *MRR* of Ru drops to only 22.3 nm/min, *ΔMRR* being 82.2 nm/min. Thus, a suitable approach must be found to minimize such a large *MRR* difference. When K_2MoO_4 is added in the slurry containing BTA, the *MRR* of Cu diminishes and that of Ru increases. This significantly reduces the *ΔMRR* between Cu and Ru. Data in Table 7.4 show that the chemical dissolution of Cu is much smaller than that of Ru, in contrast to the *MRR*, which follows an opposite trend.

In summary, the data collected in this work show that the mechanical effect is the main factor that influences the *MRR* of Cu in polishing systems. Based on our findings, we suggest that Cu is much more sensitive to mechanical forces than chemical functions of the slurry. Thus, in order to further minimize the *MRR* selectivity between Cu and Ru, the content of oxidizer should be increased and the down-force pressure of polishing reduced.

7.5 Conclusions

In this chapter, the coexistence of K_2MoO_4 and BTA in KIO_4-based slurry has been investigated. The calculation results of the parameter γ show that the galvanic corrosion of Cu is successfully mitigated in the proposed system. Furthermore, the synergistic effect on the passivation of BTA and K_2MoO_4 has been investigated. The data demonstrate that not only does the adsorption of K_2MoO_4 increase the activation energy of the oxidation reaction, but it also promotes the formation of a complex three-dimensional network with BTA, improving the stability of the passivation film. In case of Ru, the adsorbed K_2MoO_4 mainly contributes to the stable adsorption of the metal, and minimizes the content of RuO_3 on the surface, possibly inhibiting the pitting of Ru. Finally, the results of CMP tests demonstrate that in the presence of both BTA and K_2MoO_4 in KIO_4-based slurry, the *MRR* difference between Cu and Ru can be significantly minimized. It could be inferred that in order to achieve relatively equal *MRR* between Cu and Ru, the content of oxidizer should be increased and the down pressure should be reduced in the future investigations. The findings are of great value to further investigations about corrosion inhibition in the barrier layer CMP process.

References

Blouin M, Guay D (1997) Activation of ruthenium oxide, iridium oxide, and mixed Ru_xIr_{1-x} oxide electrodes during cathodic polarization and hydrogen evolution. J Electrochem Soc 144 (2):573–581

Cano E, López MF, Simancas J, Bastidas JM (2001) X-ray photoelectron spectroscopy study on the chemical composition of copper tarnish products formed at low humidities. J Electrochem Soc 148(1):E26–E30

Chadwick D, Hashemi T (1978) Adsorbed corrosion inhibitors studied by electron spectroscopy: benzotriazole on copper and copper alloys. Corros Sci 18(1):39–51

Cui H, Park J, Park J (2012) Study of ruthenium oxides species on ruthenium chemical mechanical planarization using periodate-based slurry. J Electrochem Soc 159(3):H335–H341

Cui H, Park J, Park J (2013) Corrosion inhibitors in sodium periodate slurry for chemical mechanical planarization of ruthenium film. ECS J Solid State Sci Tech 2(3):P71–P75

Fleisch TH, Mains GJ (1982) An XPS study of the UV reduction and photochromism of MoO_3 and WO_3. J Chem Phys 76(2):780–786

Hartmannsgruber E, Zwicker G, Beekmann K (2000) A selective CMP process for stacked low-*k* CVD oxide films. Microelectron Eng 50(1):53–58

Hernandez J, Wrschka P, Oehrlein GS (2001) Surface chemistry studies of copper chemical mechanical planarization. J Electrochem Soc 148(7):G389–G397

Hong Y, Devarapalli VK, Roy D, Babu SV (2007) Synergistic roles of dodecyl sulfate and benzotriazole in enhancing the efficiency of CMP of copper. J Electrochem Soc 154(6): H444–H453

Jiang L, He Y, Niu X, Li Y, Luo J (2014) Synergetic effect of benzotriazole and non-ionic surfactant on copper chemical mechanical polishing in KIO_4-based slurries. Thin Solid Films 558:272–278

Kim I, Cho B, Park J, Park J, Park H (2009) Effect of pH in Ru slurry with sodium periodate on Ru CMP. J Electrochem Soc 156(3):H188–H192

Kötz R, Lewerenz HJ, Stucki S (1983) XPS studies of oxygen evolution on Ru and RuO_2 anodes. J Electrochem Soc 130(4):825–829

McIntyre NS, Cook MG (1975) X-ray photoelectron studies on some oxides and hydroxides of cobalt, nickel, and copper. Anal Chem 47(13):2208–2213

Otmačić H, Stupnišek-Lisac E (2003) Copper corrosion inhibitors in near neutral media. Electrochim Acta 48(8):985–991

Pandija S, Roy D, Babu SV (2009) Achievement of high planarization efficiency in CMP of copper at a reduced down pressure. Microelectron Eng 86(3):367–373

Peethala BC, Babu SV (2011) Ruthenium polishing using potassium periodate as the oxidizer and silica abrasives. J Electrochem Soc 158(3):H271–H276

Ramirez Arteaga MA, Gonzalez Rodriguez JG, Rosales I, Dominguez Patiño G, Martinez Villafañe A, Neri Florez MA (2011) Corrosion inhibition of 70Cu-30Ni alloy in LiBr + ethylene glycol + H_2O mixtures by inorganic compounds. Mater Corros 62(1): 41–46

Robertson WD (1951) Molybdate and tungstate as corrosion inhibitors and the mechanism of inhibition. J Electrochem Soc 98(3):94–100

Sayed SY, El-Deab MS, El-Anadouli BE, Ateya BG (2003) Synergistic effects of benzotriazole and copper ions on the electrochemical impedance spectroscopy and corrosion behavior of iron in sulfuric acid. J Phys Chem B 107(23):5575–5585

Tromans D, Sun RH (1991) Anodic polarization behavior of copper in aqueous chloride/benzotriazole solutions. J Electrochem Soc 138(11):3235–3244

Vogt MR, Nichols RJ, Magnussen OM, Behm RJ (1998) Benzotriazole adsorption and inhibition of Cu (100) corrosion in HCl: a combined in situ STM and in situ FTIR spectroscopy study. J Phys Chem B 102(30):5859–5865

Walker DE, Wilcox GD (2008) Molybdate based conversion coatings for zinc and zinc alloy surfaces: a review. Trans IMF 86(5):251–259

Xue G, Ding J, Lu P, Dong J (1991) SERS, XPS, and electroanalytical studies of the chemisorption of benzotriazole on a freshly etched surface and an oxidized surface of copper. J Phys Chem 95(19):7380–7384

Yu P, Liao D, Luo Y, Chen Z (2003) Studies of benzotriazole and tolytriazole as inhibitors for copper corrosion in deionized water. Corrosion 59(4):314–318

Zeng X, Wang J, Lu H, Chen F, Zhang X, Qu X (2012) Improved removal selectivity of ruthenium and copper by glycine in potassium periodate (KIO_4)-based slurry. J Electrochem Soc 159(11): C525–C529

Zhang DQ, Goun Joo H, Yong Lee K (2009) Investigation of molybdate-benzotriazole surface treatment against copper tarnishing. Surf Interface Anal 41(3): 164–169

Chapter 8
Conclusions and Recommendations

8.1 Conclusions

The thesis presents a systematic research work of the chemical mechanical polishing (CMP) of Ru as a novel diffusion barrier layer for sub-14 nm technology node of the integrated circuit. The material removal mechanism of Ru and Cu in KIO_4-based slurry was thoroughly investigated based on the chemical-mechanical synergism theory. On the basis, the tribocorrosion properties of Cu and Ru as a function of slurry pH were revealed. The unsettled corrosion problems, such as galvanic corrosion between Cu and Ru, were then studied from a micro and in situ perspective, and on the basis, ways to mitigate corrosion using different slurry additives were subsequently sought for. The main conclusions are shown as follows:

(1) With a combination of the surface chemistry analysis, electrochemical experiments, and CMP test methods, the material removal mechanism of Cu was comprehensively investigated. Results show that the pH value of the slurry is decisive to the material removal mechanism of Cu. When the pH value of slurry is near neutral, Cu surface is covered by inhomogeneous $CuO/Cu(IO_3)_2{\cdot}nH_2O$/Cu-periodate/CuI passive film, which has good passivation property and weak mechanical strength. The chemical-mechanical synergistic effect plays the predominant role in the material removal of Cu polishing. Moreover, both the corrosion-enhanced abrasion and the abrasion enhanced-corrosion during polishing are strong when weak alkaline slurry is used, and thus a good polishing quality and desirable material removal rate could be obtained under this condition. Therefore, the weak alkaline polishing slurry is the most suitable for Cu CMP.
(2) The material removal mechanism of Ru was investigated, especially the corrosion kinetics of Ru in KIO_4-based slurries. Results show that Ru is oxidized to $RuO_2{\cdot}2H_2O/RuO_3$ passivation film in weak alkaline slurries. At this situation, the corrosion rate of Ru is the lowest, and the corrosion process is

J. Cheng, *Research on Chemical Mechanical Polishing Mechanism of Novel Diffusion Barrier Ru for Cu Interconnect*, Springer Theses,
DOI 10.1007/978-981-10-6165-3_8

determined by the resistance of passivation film. Because of the low mechanical strength of the surface film, which is easy to be removed by the mechanical force during polishing, the abrasion-enhanced corrosion is the most obvious under this condition. As a result, a good material removal rate of Ru could be achieved in weak alkaline slurries.

(3) CMP-electrochemical experiments combined with the traditional tribocorrosion experiments were conducted to investigate the tribocorrosion properties of Cu and Ru. Results show that the nature of tribocorrosion phenomenon is the local galvanic corrosion between the abrasion induced depassivation area and the passivation area on metal surface. The external mechanical energy is imported into the system, accelerating the anodic reactions of Cu corrosion and cathodic reactions of Ru corrosion, respectively. The tribocorrosion property is closely related to passivation on metal surfaces. When alkaline slurry is during CMP, tribocorrosion effect of both Cu and Ru is evident, which is caused by both the convection enhanced corrosion and the mechanical abrasion enhanced corrosion.

(4) The generation and development of galvanic corrosion between Cu and Ru was studied from an in situ and micro perspective mainly using the scanning probe microscopy methods. The development of Cu/Ru micro-galvanic corrosion could be divided into three stages: the galvanic corrosion immune stage, Cu surface is passivated by the native oxide layer formed in the air, which could prevent Cu from the accelerated corrosion; Cu corrosion accelerating stage, the breakdown of the native oxide layer results in the sharply accelerated corrosion of Cu, and simultaneously large amount of insoluble reaction product $Cu(IO_3)_2{\cdot}nH_2O$ initiates from the Cu/Ru interface and spreads to the whole Cu surface within a short period; galvanic corrosion stabilization stage, the insoluble $Cu(IO_3)_2{\cdot}nH_2O$ acts as the corrosion obstruction again, decelerating the corrosion of Cu, and the galvanic corrosion is stabilized henceforward.

(5) The Cu/Ru galvanic corrosion inhibition efficiency and mechanism of BTA and 1, 2, 4-triazole as corrosion inhibitors were investigated. Results show that when KIO_4 is used as the oxidant, galvanic corrosion between Cu and Ru is quite severe (compared with H_2O_2 as oxidant). Both BTA and 1, 2, 4-triazole are effective galvanic corrosion inhibitors for Cu, with corrosion inhibition efficiency up to 69.4 and 59.7, respectively. The corrosion inhibition results from the formation of protective surface layers on Cu. For BTA, a tight and complete $Cu/Cu_2O/Cu(I)BTA$ multilayer structure is formed when the concentration of BTA is high (>0.5 mM). A higher concentration of BTA results in a better corrosion inhibition effect. With regard to 1, 2, 4-triazole, the surface protective layer has a net structure, and the optimal dosage is 2 mM. Excessive 1, 2, 4-triazole will inversely reduce the stability of the surface film, as well as the corrosion inhibition efficiency.

(6) BTA-potassium molybdate (K_2MoO_4) are effective compound corrosion inhibitors in KIO_4-based slurry during the barrier layer polishing. MoO_4^{2-} preferentially adsorbs on metal surface, increasing the activation energy of the electrode reactions. Meanwhile, the compound corrosion inhibitors could

enhance the physical adsorption of MoO_4^{2-}-BTA passivation film, with insoluble molybdate salts deposited in the gaps, improving the surface passivation property. Not only could the compound corrosion inhibitors effectively suppress the galvanic corrosion within Cu/Ru coupling, but also achieve a good material removal selectivity between Cu and Ru.

8.2 Recommendations

(1) The apparatus used for the CMP-electrochemical experiments could be further improved. That is, ways should be sought for to measure the electrochemical signals during the real polishing conditions. One possible method is to connect the potentiostat with the CMP polisher (the sample on the rotational polishing head) by electrical brush.
(2) The patterned wafer using Ru as barrier layer should be used for the CMP experiments. In this way, surface and interface defects after polishing, such as Cu dishing, dielectric material erosion and galvanic corrosion, could be comprehensively investigated within different line/space width.